Biaxial Driving Technique for Ultrasound Generation with Ferroelectric Materials

by

Sagid Alberto Delgado Amparano

Supervisors: Dr Samuel Pichardo & Dr. Laura Curiel

A thesis submitted to Lakehead University in partial fulfillment of the requirements for the degree of

Doctor of Philosophy in Electrical and Computer Engineering

Lakehead University

Department of Electrical Engineering

Thunder Bay, Ontario, Canada

December 2020

ACKOWLEDGEMENTS

I would like to express my sincere gratitude to my advisor, Dr. Samuel Pichardo, for his patience, encouragement and guidance over the course of this research. His advices and all the discussions we had over the years helped me to grow as a student, but most importantly, as a person. It has been an honor to me working under his supervision.

I would also like to thank my co-advisor, Dr. Laura Curiel, whose knowledge and experience helped me through my academic career and personal life. My time during the PhD would have been very different without her proper advices.

I have also been blessed by working with such an amazing people in the NeuroFUS Lab, Andrew, Chris, Amanda, Matt, Steve, Chenchen, Bingbing, Maryam, Amine, Shirshak, Jak, I would like to give you a great thank you for all the good times we spent together.

I want to acknowledge CMC Microsystems for providing products and services that facilitated this research work and to the Natural Sciences and Engineering Research Council of Canada (NSERC), the National Council for Science and Technology of Mexico (CONACYT) and the Canada Foundation for Innovation (CFI) for the finantial support of this research work.

Lastly and most importantly, I would like to thank my parents, Felipe and Evelia, and my siblings, Ramses and Iris, whose sacrifices, support and unconditional love have been the main pillars of success along my path of education.

ABSTRACT

Over the years, ferroelectric materials have been used in a wide variety of applications in the health care field in applications such as thermal therapy, medical imaging and lithotripsy, just to mention some of them. One technical barrier in the transducer industry is that the refocusing or redirection properties of an ultrasound beam depends primarily on the “classical” solution of using a large number of independent transducer elements. High-density ultrasound transducer arrays often imply complexity from the electrical driving circuitry, mechanical constraints caused by the ultrasound probe size, and the need to handle heating of the device; all of which translates into high fabrication costs.

Commonly used ultrasound transducers are driven by applying an electric field along the poling axis to maximize their mechanical response. More efficient operation of ultrasound transducers translates into less power consumption to obtain the desired effect and less heating into the system. This work is based on an emerging technique called biaxial driving that offers and enhancement of the mechanical response of an ultrasound transducer by using two phase-offset orthogonal electrical fields on the propagation and lateral directions. In addition to the efficiency enhancement, we hypothesize that the biaxial driving technique produces an added vibration mode due tothe application of the second electric field, which will allow a controlled acoustic pressure redistribution that can be exploited to produce a refocusing or steering of the ultrasound beam with a single element, or an array where fewer elements than conventional transducer arrays are needed.

The objective of this research work is to demonstrate with numerical and experimental work that controlled steering of the ultrasound beam can be achieved by the application of a biaxial driving in single-element ferroelectric transducers. A finite element analysis has been carried out to simulate and calculate the efficiency and the acoustic field response on different ferroelectric materials biaxially driven. Different transducer shapes and parameters have been tested, demonstrating a change in the efficiency and the steering of the acoustic field using a single-element transducer. Experimental validation was performed for the specific case of the lead zirconate titanate material, using prismatic and ring geometries for the transducers. We demonstrated for the first time the steering capabilities for single-element ultrasound transducers through our simulation and experimental work. Steering angles up to 30° were reached from our experimental validations for the single-element prismatic transducers while using the biaxial driving technique. It was also demonstrated that a controlled refocusing from 4.5 mm to 9 mm is possible for single-element ring shaped transducers while applying the two orthogonal electric driving signals.

In addition to the acoustic efficiency, we also proved that there was an improved response on the axial resolution and the signal-to-noise ratio on a simple ultrasound imaging device. The biaxial driving method has the potential to improve the focusing of phased arrays and open new opportunities for the use of single-element devices that can take advantage of the control of the ultrasound beam directivity.

Table of Content

LIST OF FIGURES

LIST OF TABLES

LIST OF SYMBOLS

c	Speed of sound
c_{ijkl}^{E}	Elastic stiffness constant (constant electric field)
C_p	Dielectric capacitance
C_t	Specific heat of tissue
C_{tb}	Specific heat of blood
C_β	Viscous damping
d	Distance
d_{kij}	Piezoelectric constant ($m \cdot V^{-1}$)
D_i	Electric displacement
e_{ijk}	Piezoelectric constant ($C \cdot m^{-2}$)
E_c	Coercive field
E_i	Electric field

E_w	Energy accumulated on the electrodes of a piezoceramic transducer due to piezoelectric effect (electrodes open-circuit)
f_r	Resonance frequency
f	Frequency
F	Force
f'	Frequency of an echo (Doppler effect)
f_1, f_2	right and left -3 dB frequency
F_A	Assembly force vectors
g	Acceleration due to gravity ($9.81\ ms^{-2}$)
H	Enthalpy
$Hl\{\quad\}$	Hilbert transform
I	Intensity (acoustic or electric as specified)
I_R	Intensity reflection coefficient
I_T	Intensity transmission coefficient
k	Relative dielectric constant
k_{ij}	Electromechanical coupling coefficient
k_t	Thermal conductivity
K	Anisotropy degree of the free energy surface
K_A	Assembly element characteristic matrix
l	Length
m	Change in mass
Ng	Number of gray scale levels
p	Pressure
p_l	Power applied at the lateral electrodes of a biaxial transducer
P	Polarization
P_r	Remanent polarization
P_s	Spontaneous polarization
q	Charge
Q	Complex charge
$\dot{Q}$	Source of heating
Q_m	Quality factor
r	location vector with Cartesian components (x,y,z)
r_{ab}	Absorption at the boundary
r_c	Reflection coefficient
s	Surface
$S(t)$	Envelope of a signal
S_{in}	Mean signal measured inside the region of an object
S_{out}	Average signal measured in the region of an object, without the object
S_{ijkl}^E	Compliance coefficient (constant electric field)
t	Time
t_h	Thickness
T	Period; Temperature

T_c	Curie Temperature
$T_{i,j}$	Stress
Tr_c	Transmission coefficient
$\tan\sigma$	Dielectric dissipation factor
u	Particle velocity
U	Displacements
U_b	Energy barrier height for the tetragonal to cubic phase
U_b^*	Energy barrier height for the orthorhombic to cubic phase
U_e	Stored energy in the piezoelectric medium
U_{LD}	Free-energy density (Landau-Devonshire)
$\vec{v}$	Instantaneous velocity
V	Voltage
Vol	Volume
w	Width
W_A	Acoustic power
W_b	Perfusion
W_E	Effective electric power
W_M	Mechanical work
Y_o	Fluid admittance
Δz	Deflection
Z	Impedance (acoustic or electric as specified)
α	Attenuation coefficient
β	Boundary absorption coefficient
β_0	Compressibility of the medium
γ	Steering angle produced by a biaxial transducer
δ	Particle displacement
ε_{ij}^{ξ}	Dielectric constant (constant strain)
η	Acoustic efficiency
θ	Reflection angle
θ_b	Angle between acoustic beam and blood vesseld axis
λ	Wavelength
μ_S	Average of a signal
ξ_{ij}	Strain
ρ	Density
σ_n	Standard deviation of the noise
τ	Time constant
ϕ	Phase difference between the propagation and lateral electrodes of a biaxial transducer
Ψ	Centroid for conventional or biaxial acoustic field
ω	Angular frequency
$[B]$	Strain-displacement matrix
$[C]$	Damping matrix
$[C_F]$	Fluid damping matrix

$[C^{vh}]$	Electric damping matrix
$\{F_F\}$	Fluid pressure load
$\{J\}$	Vector of nodal, body or surface charges
$\{J^{th}\}$	Thermo-piezoelectric load vector
$[K]$	Structure stiffness matrix
$[K^d]$	Dielectric permittivity coefficient matrix
$[K_f]$	Fluid stiffness matrix
$[K^z]$	Piezoelectric coupling matrix
$\{L\}$	Gradient operator $\nabla()$
$\{L\}^T$	Divergence operator $\nabla \cdot (\quad)$
$[M]$	Mass matrix
$[M_f]$	Fluid mass matrix
$\{n\}$	Normal to the surface
$\{N\}$	Element shape function for pressure
$\{\acute{N}\}$	Element shape function for displacement
$\{u\}$	Nodal degree of freedom
$\rho_o[R]^T$	Coupling mass matrix for a fluid-structure interaction
$\{\varphi\}_n$	Mode shape eigenvector at the nth frequency

CHAPTER 1: INTRODUCTION

1.1 Introduction

Ferroelectric materials are used in a wide range of applications, such as energy storage, tunable capacitors, non-volatile memory devices, sensors, and actuators[1]. In the medical field, ferroelectric materials are often employed as ultrasound transducers in applications such as imaging[2], ablation therapy[3], and lithotripsy treatments[4]. The conventionally desired characteristics for medical ultrasound transducers include a high thickness mode coupling coefficient, which is related to the conversion of electrical energy to mechanical energy (and vice versa), low planar mode coupling coefficient, low acoustic impedance, high dielectric constant and small dissipation factor[5].

Ultrasound transducers convert an electric driving signal into ultrasound waves, or the incident ultrasound waves into an electric signal. The rate of conversion from one form of energy to another is called efficiency. Ferroelectric materials do not have a 100% efficiency conversion, so part of the energy delivered to the transducer is converted into other forms of energy, mainly heat. The heat generation that occurs within the ferroelectric material depends on the material dielectric and elastic losses and the acoustic impedance, frequency, amplitude and duty-cycle of the driving voltage[6]–[9]. This self-heating produces a reduction in the transducer's acoustic power response[6], [10] and hence a reduced efficiency. The heat generation issue is more critical when bigger size piezoceramics or high power ultrasound therapy applications such as the high intensity focused ultrasound (HIFU) are considered, due to the fact that the efficiency deteriorates when higher driving powers are applied[11] which in addition produce more heating that translates into a higher efficiency reduction. This heat generation can depolarize the ferroelectric material if it reaches a temperature value close to its Curie temperature[10], which corresponds to the value at which a ferroelectric material changes its ferroelectric phase into a paraelectric phase and hence loses its ferroelectrical properties.

Ultrasound imaging transducers can present problems with heat generation due to the fact that their efficiency ranges from 20% to 70%, which can produce increments of temperature up to 60%[12] The IEC standard 60601-2-37:2007 states that for ultrasound transducers used in humans, its increment in temperature should not be higher than 6 °C for endocavitary applications, 10 °C for external use and 27 °C while used in air[13]–[15]. A second disadvantage related to low-efficiency transducer is that the applied driving peak voltage needs to remain lower than the polarized voltage used to produce the

ferroelectric material[10], or it will lose its respective spontaneous polarization in that direction, which limits the maximum acoustic power that a transducer can deliver. The application of a cooling system inside the ultrasound transducer can reduce the produced heat, and an electrical direct current bias can help the peak voltage problem, but increasing the overall efficiency helps to solve both issues. In therapeutic devices using ultrasound, such as high intensity focused ultrasound, it is expected that a cooling system will be used to protect both, the transducer and the tissue that may be in proximity to the transducer[16]–[18], because the transducer is generating heat due the fact that is being driven in continuous mode during many seconds .

For imaging applications, lower efficiencies and hence heat generation lead to a reduced sensitivity[19] while detecting the reflected echoes in receive mode, producing a low signal-to-noise ratio (SNR). For ultrasound imaging, good contrast and resolution with increasing penetration depth is highly desired. Tissue attenuation causes the backscattered signal power to diminish its amplitude as depth increases[20]; the signal reaches a point where the produced echo signal power is so low that the transducer's sensitivity does not allow an image to be reconstructed anymore. Since the amount of power that a transducer probe can handle is limited for safety concerns, and the received signal is in the range of the milivolts or lower[21], good quality imaging reconstructions of deep regions are remarkably difficult. Decreasing the transmission frequency provides an increase in penetration but at the expense of reducing the lateral and axial resolution, which means that objects that are close to each other might not be recognized anymore.

1.1.1 Improving Efficiency of Transducers Using the Biaxial Driving Method

The piezoelectric, dielectric, and ferroelectric properties of ferroelectric ceramics can be enhanced by optimizing their calcination or sintering processes[22]–[24] or by adding doping materials such as *Ce*, *Al*, *MgZr,* and MnO_2[25]–[28]. The energy conversion within a ferroelectric material can also be improved by using one emerging technique called biaxial driving[29], [30]. This technique relies on the reduction of the coercivity and consequently decreasing energy dissipation during operation. This reduction in coercivity is achieved by applying two orthogonal electrical fields with a phase offset. Two sets of electrodes are placed on the ferroelectric material to produce two orthogonal electrical fields; the first set (propagation or P-electrode) is attached to faces perpendicular to the poling axis while the second set (lateral or L-electrodes) is attached to faces parallel or lateral to the poling axis. Both sets of electric signals should have the same driving frequency[30]; otherwise, the efficiency response would be reduced; it has been shown that efficiency follows a sinusoidal response as a function of the phase between the electrical

fields[30]. When the right phase is applied, higher efficiencies can be achieved with biaxial driving than with conventional monoaxial driving[30].

This increment in efficiency allows one to take advantage of a maximum amount of energy conversion for an ultrasound probe, which results in improving the receiving sensitivity and allows to properly detect the low amplitude ultrasound echo from deeper zones within the tissue, without having to reduce the frequency and therefore have a loss of axial or lateral resolutiont. For therapeutic applications, higher efficiencies can potentially translate into less energy required to produce the desired effect (cavitation, ablation, etc.) without generating a significant amount of heat on the transducer that could damage the transducer, the patient or require treatment times to be longer.

Lead Zirconate Titanate (PZT) transducers are the most widely used worldwide because of their high electromechanical coupling factor, and the fact that the piezoelectric properties can be enhanced easily by chemical modifications[31], [32]. However, the production of lead-based ceramics cause environmental problems due to the toxicity of lead and the volatility of PbO during production[33]. The biaxial driving method increased efficiency results while driving PZT ceramics[30] suggest that other materials like $\mathrm{BaTiO_3}$, $\mathrm{LiNbO_3}$ or KNN-based piezoceramics could be an interesting alternative to achieve similarly high efficiency with a less toxic material.

1.2 Hypotheses on New Applications of the Biaxial Driving Method

In prismatic-shaped ferroelectric materials poled along the thickness axis, an extensional deformation is expected along the length[34] when an electric field is applied along the poling direction at its resonance frequency (f_r). The application of an electric field orthogonal to the poling axis to such materials produces a thickness-shear deformation[35]. I **hypothesize** that along with the coercive field and polarization changes produced by biaxial driving[29], [30], the interaction between the orthogonal electric fields applied on the ferroelectric material would produce a combination of extensional and shear deformations as a function of the applied phase difference, ϕ, between the propagation and lateral electric fields; this, in turn, translates into controlled steering of the acoustic beam. A representation of the vibration mode for the propagation, lateral and biaxial mode is shown in Fig. 1.1.

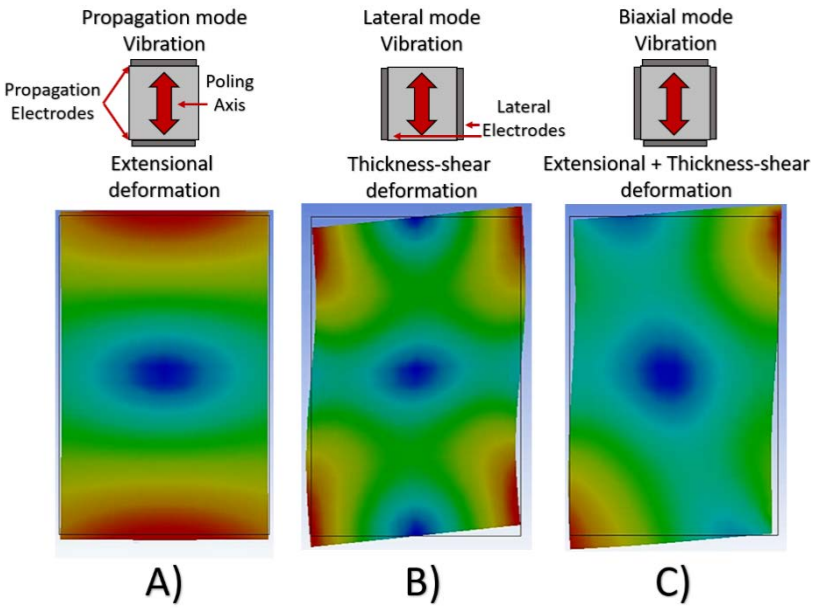

Fig. 1. 1. Simulation of the vibration modes for propagation (A), lateral (B) and biaxial mode (C) of a prismatic shaped PZT transducer poled along the thickness direction. Biaxial mode is testing a phase value of 0°.

Furthermore, I **hypothesize** that the intensity of the lateral electric field affects the acoustic efficiency response[36] suggesting that the power applied to the lateral electrical field should be reduced to achieve maximum efficiency.

In this study, we investigated the feasibility of producing ultrasound beam steering with a single-element transducer using the biaxial driving technique and its potential applications. We conducted simulations using finite element analysis (FEA) and experimental validation to establish and verify the driving conditions for steering single-element biaxial transducers.

Also, we applied the biaxial driving technique to an ultrasound imaging probe to register the acoustic field effects produced by this driving method and prove that the increase in efficiency translated into improved sensitivity and therefore better signal-to-noise ratio.

CHAPTER 2: OBJECTIVES AND MOTIVATION

2.1 Main Objective

The main objective of the present work is to demonstrate with simulations based on the finite element method and experimental validations that, in addition to the acoustic efficiency enhancement[30], the application of the biaxial driving technique on single-element ultrasound transducers produces a directional controlled acoustic beam while using a prismatic shaped ferroelectric material and an enhanced focusing for transducers with a ring shaped ferroelectric material. Different materials, and parameters were tested to establish the best driving conditions to achieve steering for biaxial transducers. Along with the steering and refocusing properties, we aim to demonstrate how the biaxial method can be applied to improve the performance of imaging applications of ultrasound.

2.2 Specific objectives

To achieve the main objective of this work we conducted simulations, experimental validations and application studies, as follows:

2.2.1 Numerical simulation of the biaxial driving on different ferroelectric materials

- FEA modelling of biaxially driven single-element ultrasound transducers made of PZT, $LiNbO_3$ and $BaTiO_3$ with a prismatic shape.
- FEA modelling of biaxially driven ring-shaped single-element ultrasound transducers made of PZT.
- Characterization of the impedance, efficiency response and acoustic pressure distribution produced by a biaxial excitation as a function of the difference in phase and power applied on the lateral electrode.
- Comparison of the conventional and biaxial driving response for the efficiency and acoustic pressure distribution.

2.2.2 Experimental validation of prismatic-shaped single-element biaxial transducer

- Design and construction of a set of single-element PZT biaxial transducers with a prismatic shape and a set of conventional transducers with the same geometry.
- Characterization of the acoustic pressure and efficiency of conventional and biaxial transducers at the propagation resonance frequency by using conventional and biaxial driving while testing different phases and powers on the lateral electrode.
- Comparison with the FEA model results.

2.2.3 Ring-shaped single-element biaxial transducer application

- Design and construction of a set of single-element PZT biaxial transducers with a ring shape.

- Characterization of the acoustic pressure and efficiency of ring biaxial transducers by using conventional and biaxial driving while testing different phases and powers on the lateral electrode.
- Comparison with the FEA model results.

2.2.4 Biaxial ultrasound imaging probe

- Construction of a 4-elements array with biaxial configuration for ultrasound imaging.
- Design of an ultrasound imaging algorithm to drive the biaxial ultrasound imaging probe with the Verasonics Vantage system.
- Characterization of the acoustic pressure of the imaging probe at the propagation mode resonance frequency while applying a phase variation on the lateral electrodes.
- Characterization of the acoustic pressure of the imaging probe at the propagation mode resonance frequency with the while applying a power variation on the lateral electrodes.
- Application of the biaxial driving technique on reception mode.
- Imaging formation using different combinations of excitation at propagation only (P-), lateral only (L-) and combined propagation and lateral (P+L) modes on transmission and reception
- Evaluation of the axial resolution and signal to noise ratio (SNR) on formed images.

2.3 Significance and Motivation

For therapy applications of ultrasound, the outcome of this work can have a significant impact. For applications in pre-clinical research in neurosciences, improvements in focusing and directivity of the controlled acoustic field can be used to treat highly localized targets within the brain of murine models. For the imaging applications, the axial resolution and sensitivity can be improved, which can lead to enhancing diagnostic capabilities for ultrasound imaging.

2.4 Organization of the thesis

The thesis is organized in 7 chapters covering the fundamental theory of ultrasound waves and ultrasound transducer technology, the validation and the application of the emerging technique called biaxial driving through finite element simulations and experimental validations.

- Chapter 1 & 2 give an introduction to the research work and include the objectives and motivation.
- Chapter 3 provides a review of the required background describing the generation and propagation of ultrasound waves and its application in the medical field as therapy or imaging.

- Chapter 4 includes the theoretical basis describing the biaxial driving technique and the modelling tools used to represent the biaxial transducer response.
- In chapter 5 the simulation and experimental validation for different single-element transducer configurations using the biaxial driving technique are presented. The study includes a ring and a prismatic shaped single-element biaxial transducer with an analysis of the acoustic and efficiency and the steering response through the variation of different parameters.
- Chapter 6 presents the experimental application of biaxial driving to a 3-element ultrasound imaging probe. It includes the analysis of resolution and signal-to-noise ratio improvement when using biaxial driving.
- Finally, Chapter 7 provides the conclusions and discussion.

CHAPTER 3: BACKGROUND

3.1 Ultrasound

Sound is a phenomenon that involves the propagation of a mechanical wave through an elastic medium, which can be in the liquid, solid or gaseous state[37], by the motion of particles within the medium. According to the frequency of the sound wave, it is classified as infrasound when the frequency has values lower than 20 Hz; audible sound when the frequency is in the range of 20 Hz and 20 kHz, which correspond to the frequencies that human beings can hear; and ultrasound, which refers to an acoustic wave whose frequency is above the 20 kHz. In acoustics, waves can be classified as follow:

- Longitudinal waves. They consist of alternated compressions and rarefactions along the propagation direction in which the particles transmit the wave when moving back and forth from their equilibrium position parallel to the movement axis of the wave[38]. The speed of propagation is determined primarily by the elastic and stiffness properties of the medium, resulting in a faster wave propagating within a stiff medium than in one that is highly elastic. With the passage of the wave, there are changes in the particle displacement, velocity, density, pressure, and temperature[20].
- Transverse waves. They consist of vibrations that are perpendicular to the direction of propagation. In contrast to the changes in particle volume for longitudinal waves, no density change occurs for transverse waves. The speed at which the transverse wave propagates is approximate 50% of the longitudinal wave for the same material[37]. Transverse waves cannot be propagated in liquids[20].
- Rayleigh waves. They consist of surface acoustic waves resulting from the coupling of longitudinal and transverse waves. This wave propagation is produced at the boundary that separates a solid from a rarefied medium such as the air[37]. Each particle moves in an elliptical orbit as the wave passes through it, and the amplitude of that particle displacement decays rapidly as the distance with the surface increases.

3.2 Characteristics of ultrasound

3.2.1 Frequency

The variables that can describe the propagation of a wave in time and space are frequency f (or its inverse, the period $T = f^{-1}$, and wavelength λ given by

$$\lambda = \frac{c}{f} = cT, \tag{3.1}$$

where c is the speed of sound[39].

3.2.2 Acoustic impedance

The acoustic impedance Z of a medium is a parameter that represents the relation between the resistances of the particles of a medium and the mechanical vibrations. This resistance is increased proportionally to the density and the speed of sound in the medium. The acoustic impedance can be defined as the product of the density of the medium (lossless) and the propagation velocity of the ultrasound in it. This relationship can be described with

$$Z = \rho c, \tag{3.2}$$

where *Z* is the impedance of the medium, ρ is the mass density of the medium, and *c* is the speed of sound in the medium[40]. The acoustic impedance has the rayl as a unit, which is equal to $\mathrm{kg} \cdot \mathrm{m}^{-2}\mathrm{s}^{-1}$.

3.2.3 Acoustic intensity

The amount of power transported through an area perpendicular to the acoustic beam can be characterized by the acoustic intensity I, which is defined as the energy transmitted per unit of time and per unit of area in the direction normal to the considered area[39]. The time-averaged acoustic intensity of a continuous wave is related to the pressure amplitude p in the medium as

$$I = p^2(2\rho c)^{-1} \tag{3.3}$$

In the field of medical ultrasound, I is measured in W·cm^{-2}.

3.2.4 Attenuation

When an acoustic wave travels through a medium, part of its mechanical energy is converted into other types of energy (mostly heat) so that its intensity gets reduced the farther it goes; this effect is called attenuation[41]. In general, overall ultrasound attenuation is characterized by the following exponential decay of the pressure amplitude p and of the amplitude of the acoustic intensity I with the traveling distance d [39]

$$p = p_0 e^{-\alpha d} \tag{3.4}$$

$$I = I_0 e^{-2\alpha d} \tag{3.5}$$

Where p_0 and I_0 are the pressure and intensity at $d = 0$ and α is the pressure frequency-dependent attenuation coefficient. An acoustic wave can be attenuated by different mechanisms, including the

following: absorption, which is the process where the energy of the ultrasonic beam is transferred to the propagation medium and converted into other types of energy (heat, chemical energy, light)[40]; and scattering due to changes of the acoustic impedance. Attenuation increases with frequency in biological tissues, and the attenuation coefficient of most tissues increases approximately linearly with frequency. Table 3.1 shows an example of attenuation values for biological tissue.

Table 3. 1 Attenuation values for some human tissues[41]

TISSUE	ATTENUATION $(\mathbf{dB\ cm^{-1}MHz^{-1}})$
LIVER	0.399
BRAIN	0.435
MUSCLE	0.57
BLOOD	0.15
WATER	0.02
BONE	22

3.2.5 Specular Reflection and refraction

Reflection and refraction occur at the boundary between media with different acoustic impedances or different speeds of sounds[39]. If we consider a sound wave that strikes on a surface (interface between two media), part of the energy is reflected (echo) depending on the characteristics of the surface and the adjoining substance. The rest of the wave that was not reflected passes through the interface separating two media with different c or Z[42] and changes its propagation direction. There are two important interfaces to consider: The fluid-fluid interfaces, which are often associated to the discontinuity between two soft tissues and the fluid-solid interfaces, such as the boundary between soft tissues and bone[39].

3.2.5.1 Fluid-fluid interface

When a plane acoustic wave impinges on a smooth interface, reflected and transmitted longitudinal waves (only longitudinal) can be generated. According to Snell's law, the reflection angle θ_1 is equal to the angle of the incident wave, and the transmitted wave is refracted away from the direction of the incident wave with an angle θ_2 given by[39]

$$\frac{\sin\theta_1}{c_1} = \frac{\sin\theta_2}{c_2}, \tag{3.6}$$

where c is the speed of sound for each medium. The ratio of the reflected acoustic pressure is called reflection coefficient r_c , and for a normal incidence it can be calculated as

$$r_c = \frac{Z_1 - Z_2}{Z_1 + Z_2}, \tag{3.7}$$

where Z_n is the impedance of each *n*-medium[39]. the ratio of the transmitted to the incident acoustic amplitude is called amplitude transmission coefficient Tr_c and is given by:

$$Tr_c = \frac{2Z_2}{Z_1 + Z_2} \tag{3.8}$$

The intensity reflection (I_R) and transmission (I_T) coefficients are defined in a similar way as

$$I_R = \left(\frac{Z_1 - Z_2}{Z_1 + Z_2}\right)^2 \tag{3.9}$$

$$I_T = \frac{4Z_1Z_2}{(Z_1 + Z_2)^2} \tag{3.10}$$

3.2.5.2 Fluid-solid interface

At normal incidence, (3.7) and (3.8) represents the ideal case to determine the reflected and transmitted energies. For oblique incidence, the refracted longitudinal wave is partially converted into a shear wave, and two refracted beams are produced. For oblique incidence, the Snell's law can be generalized to[39]

$$\frac{\sin\theta_1}{c_1} = \frac{\sin\theta_{2L}}{c_{2L}} = \frac{\sin\theta_{2S}}{c_{2S}}, \tag{3.11}$$

where $2L$ and $2S$ refers to the refracted longitudinal and shear waves in the solid medium. Fig. 3.1 shows the fluid-fluid and fluid-solid interfaces interaction with an ultrasound beam.

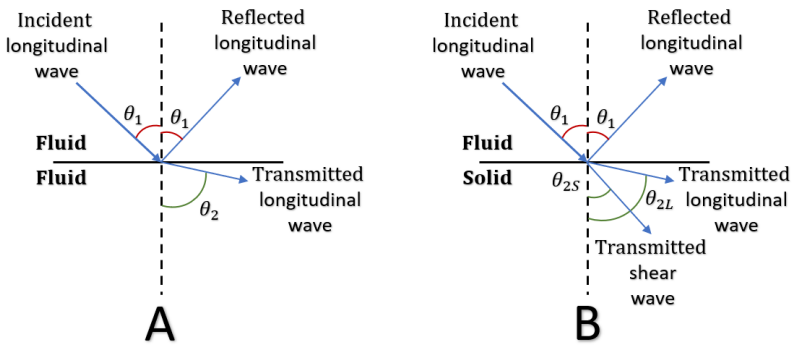

Fig. 3. 1. Reflection and refraction of an ultrasound beam for a medium. (a) fluid-fluid interfaces and (b) a fluid-solid interface[39].

3.2.6 Scattering

When an ultrasound beam impinges into an interface with an inhomogeneous shape, and its dimensions are smaller than the wavelength of the ultrasound beam, the incident beam is reflected in many directions called scattered waves[43]. The scattered intensity from soft tissues is generally smaller than the specular reflected intensity from organ boundaries. In soft tissue, the density and compressibility of scatters are close to those of the surrounding medium. Thus, the contribution of scattering to attenuation is relatively small. In the MHz range of frequencies, attenuation due to scattering is in the range of 10-15% of the total attenuation[43].

3.3 Piezoelectricity

The most widespread method to generate an ultrasound wave is by the application of the piezoelectric effect, which relies on the application of an electric signal into a special crystal or polycrystalline structure to produce a mechanical deformation. A crystal can be defined as “a special arrangement of atoms that repeats itself periodically in three dimensions” [35] and which smallest repeating unit is called the unit cell. This unit cell can be described by referring the atoms as the intersection points of a three-dimensional network of lines called space lattice. The size and shape of the lattice are described by the axial length vectors *a*, *b* and *c* and its respective interaxial angle α, β and γ. A crystal structure with its respective unit cell are represented in Fig. 3.2.

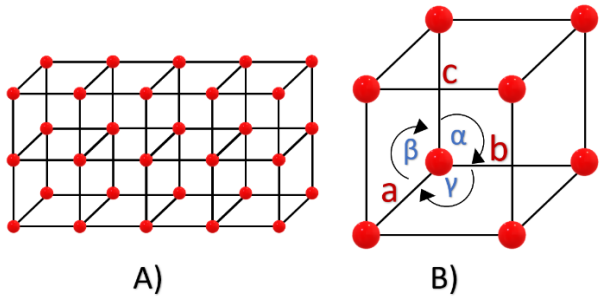

Fig. 3. 2. Representation of a crystalline solid (A) with its respective unit cell (B).

Most piezoelectric materials are crystalline solids that can be single crystals or polycrystalline materials like ferroelectric ceramics[35]. During the natural growth of some crystals, the planes of the highest atomic density have a propensity to form the external faces[35]. The relationship between these faces produces a symmetry that forms the basis of the classification of the crystals into 32 conventional symmetry classes known as point groups. Those 32-point groups can also be regrouped into seven different sets, each having one common symmetry element[44], which are known as the seven crystal systems. Table 3.2 describes the seven crystal systems and their corresponding relation between its lattice angles (α, β, γ) and vectors (a, b, c) for the unit cell.

Table 3. 2 Seven crystal systems[44]

Crystal System	Relation between a, b and c	Relation between α, β and γ
Triclinic	a ≠ b ≠ c	$\alpha \neq \beta \neq \gamma$
Monoclinic	a ≠ b ≠ c	$\alpha = \gamma = 90°, \neq \beta$
Orthorhombic	a ≠ b ≠ c	$\alpha = \beta = \gamma = 90°$
Rhombohedral	a = b = c	$\alpha = \beta = \gamma \neq 90°$
Tetragonal	a = b ≠ c	$\alpha = \beta = \gamma = 90°$
Hexagonal	a = b ≠ c	$\alpha = \beta = 90°, \gamma = 120°$
Cubic	a = b = c	$\alpha = \beta = \gamma = 90°$

In 1880 the Curie brothers (Pierre and Jaques)[45] discovered that when certain classes of crystals are compressed or stretched, an electrical charge will appear on their surfaces. This process is called the piezoelectric effect[39]. When the crystal is mechanically strained or deformed, electrical charges appear on the surface. When the direction of the deformation reverses, the polarity of the electrical charge is reversed too. Less than a year later, Lippman[46] predicted the inverse piezoelectric effect, in which an

applied electric field resulted in a change in crystal dimensions, an effect that was verified shortly thereafter by the Curie brothers. As the direct piezoelectric effect does, if the electric field applied to a crystal is reversed, the resulting strain is reversed too. Fig. 3.3 represents the piezoelectric effect.

(a) (b)

Fig. 3. 3. Representation of the piezoelectric effect. (a) direct and (b) inverse[47].

3.3.1 Piezoelectric constitutive equations

When a small electric field/mechanical stress is applied to a piezoelectric material, it presents a linear profile. However, they may show a non-linear response if a high electrical field or mechanical stress is applied[48]. The purpose of this section is to describe the electromechanical properties of piezoelectric materials by assuming a linear behaviour[35] and that the total strain on the material is the sum of the mechanical strain induced by the mechanical stress and the controllable actuation strain caused by the applied electric voltage[48]. The representation of a piezoelectric material used for ultrasound generation is shown on Fig. 3.4, with the X, Y and Z axis represented by the number 1, 2 and 3 respectively

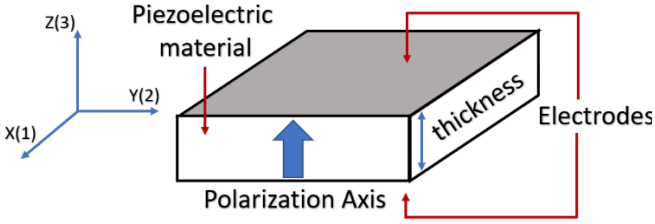

Fig. 3. 4. Piezoelectric material with electrodes attached. The polarization axis is oriented at the thickness or Z(3) direction.[48]

The conservation of energy for a linear piezoelectric medium can be represented[48] with the first law of thermodynamics as

$$\frac{\partial U_e}{\partial t} = T_{ij}\frac{\partial \xi_{ij}}{\partial t} + E_i\frac{\partial D_i}{\partial t} \tag{3.12}$$

where U_e represents the stored energy in the piezoelectric medium, T_{ij} is the stress component, ξ_{ij} is the strain component E_i is the electric field component, D_i is the electric displacement component, t is the time and $i, j = 1,2,3$ refers to the material coordinate system [35]. The electric enthalpy H can be defined by

$$H = U_e - E_i D_i \tag{3.13}$$

by differentiating (3.13) with respect to time

$$\frac{\partial H}{\partial t} = \frac{\partial U_e}{\partial t} - E_i \frac{\partial D_i}{\partial t} - \frac{\partial E_i}{\partial t} D_i \tag{3.14}$$

and substituting in (3.12) we obtain

$$\frac{\partial H}{\partial t} = T_{ij} \frac{\partial \xi_{ij}}{\partial t} - D_i \frac{\partial E_i}{\partial t} \tag{3.15}$$

that implies

$$H = H(\xi, E). \tag{3.16}$$

Differentiating (3.16) with respect to time we get

$$\frac{\partial H}{\partial t} = \frac{\partial H}{\partial \xi_{ij}} \frac{\partial \xi_{ij}}{\partial t} + \frac{\partial H}{\partial E_i} \frac{\partial E_i}{\partial t} \tag{3.17}$$

$$\left(T_{ij} - \frac{\partial H}{\partial \xi_{ij}}\right) \frac{\partial \xi_{ij}}{\partial t} - \left(D_i + \frac{\partial H}{\partial E_i}\right) \frac{\partial E_i}{\partial t} = 0 \tag{3.18}$$

Because (3.18) must hold for arbitrary[49] $\frac{\partial \xi_{ij}}{\partial t}$ and $\frac{\partial E_i}{\partial t}$ we can obtain

$$T_{ij} = \frac{\partial H}{\partial \xi_{ij}} \tag{3.19}$$

$$D_i = -\frac{\partial H}{\partial E_i} \tag{3.20}$$

A proposed[35], [49] homogeneous quadratic form for *H*

$$H = \frac{1}{2} c_{ijkl}^E \xi_{ij} \xi_{kl} - e_{kij} E_i \xi_{jk} - \frac{1}{2} \varepsilon_{ij}^{\xi} E_i E_j \tag{3.21}$$

where $i, j, k, l = 1,2,3$, $c_{ijkl}^E = c_{ijlk}^E = c_{jikl}^E = c_{klij}^E$ is the elastic stiffness constant (Nm^{-2}) and e_{ijk} and ε_{ij}^{ξ} represent the piezoelectric (Cm^{-2}) and dielectric constant (Fm^{-1}), respectively.

By differentiating (3.21) with respect to ξ_{ij} and substituting the (3.19)

$$T_{ij} = c_{ijkl}^E \xi_{kl} - e_{kij} E_k \tag{3.22}$$

which can be written in terms of the strain ξ_{ij}

$$\xi_{ij} = S^E_{ijkl} T_{kl} + d_{kij} E_k \tag{3.23}$$

with $S^E_{ijkl} = \frac{1}{c^E_{ijkl}}$ is the matrix of compliance coefficients and d_{kij} is the piezoelectric constant (mV^{-1}). Also, if we differentiate (3.21) with respect to E_i and substituting (3.20) we get

$$D_i = e_{ikl} \xi_{kl} + \varepsilon^{\xi}_{ik} E_k \tag{3.24}$$

which can be written as

$$D_i = d_{ikl} T_{kl} + \varepsilon^{T}_{ik} E_k \tag{3.25}$$

(3.22 – 3.25) describe the electromechanical equations for a linear piezoelectric material. (3.22) and (3.23) express the inverse piezoelectric effect while (3.24) and (3.25) the direct piezoelectric effect[48].

The material coefficients matrices for a particular symmetry needs to be considered[49] to determine the solution of piezoelectric vibration problems. For this reason, the compressed matrix notation turns out to be more useful than the extended tensor notation[48].

For the equation that describes the inverse piezoelectric effect (3.23), the strain components ξ_{ij} are usually a symmetric second-rank tensor[35] which lead to have $\xi_{ij} = \xi_{ji} = \xi_n$ allowing $d_{kij} = d_{kji} = d_{kn}$. If only pure stresses (i.e., no body torques) are considered[35], then $T_{kl} = T_{lk} = T_m$, and because $S^E_{ijkl} = S^E_{ijlk} = S^E_{jikl} = S^E_{klij}$ the compliance matrix can be written as S^E_{nm} resulting in the compressed matrix form of the inverse piezoelectric effect

$$\xi_n = S^E_{nm} T_m + d_{kn} E_k \ (k = 1 - 3; n, m = 1 - 6) \tag{3.26}$$

For the equation that describes the direct piezoelectric effect (3.25), if only pure stresses (absence of body torques) are considered[35], then $T_{kl} = T_{lk} = T_m$ allows the piezoelectric constant $d_{ikl} = d_{ilk} = d_m$, which can transform (3.25) as

$$D_i = d_{im} T_m + \varepsilon^{T}_{ik} E_k \ (i, k = 1 - 3;\ m = 1 - 6) \tag{3.27}$$

Eq. 3.26 (with d_{kn}transposed) and 3.27 can be written, respectively, as its matrix form as

$$\begin{bmatrix} \xi_1 \\ \xi_2 \\ \xi_3 \\ \xi_4 \\ \xi_5 \\ \xi_6 \end{bmatrix} = \begin{bmatrix} S_{11} & S_{12} & S_{13} & S_{14} & S_{51} & S_{61} \\ S_{21} & S_{22} & S_{23} & S_{24} & S_{52} & S_{62} \\ S_{31} & S_{32} & S_{33} & S_{34} & S_{53} & S_{63} \\ S_{41} & S_{42} & S_{43} & S_{44} & S_{54} & S_{64} \\ S_{51} & S_{52} & S_{53} & S_{54} & S_{55} & S_{65} \\ S_{61} & S_{62} & S_{63} & S_{64} & S_{65} & S_{66} \end{bmatrix} \begin{bmatrix} T_1 \\ T_2 \\ T_3 \\ T_4 \\ T_5 \\ T_6 \end{bmatrix} + \begin{bmatrix} d_{11} & d_{21} & d_{31} \\ d_{12} & d_{22} & d_{32} \\ d_{13} & d_{23} & d_{33} \\ d_{14} & d_{24} & d_{34} \\ d_{15} & d_{25} & d_{35} \\ d_{16} & d_{26} & d_{36} \end{bmatrix} \begin{bmatrix} E_1 \\ E_2 \\ E_3 \end{bmatrix} \tag{3.28}$$

and

$$\begin{bmatrix} D_1 \\ D_2 \\ D_3 \end{bmatrix} = \begin{bmatrix} d_{11} & d_{12} & d_{13} & d_{14} & d_{15} & d_{16} \\ d_{21} & d_{22} & d_{23} & d_{24} & d_{25} & d_{26} \\ d_{31} & d_{32} & d_{33} & d_{34} & d_{35} & d_{36} \end{bmatrix} \begin{bmatrix} T_1 \\ T_2 \\ T_3 \\ T_4 \\ T_5 \\ T_6 \end{bmatrix} + \begin{bmatrix} \varepsilon_{11} & \varepsilon_{12} & \varepsilon_{13} \\ \varepsilon_{21} & \varepsilon_{22} & \varepsilon_{23} \\ \varepsilon_{31} & \varepsilon_{32} & \varepsilon_{33} \end{bmatrix} \begin{bmatrix} E_1 \\ E_2 \\ E_3 \end{bmatrix} \tag{3.29}$$

Assuming the most typical case, where a piezoelectric material transversely isotropic (piezoelectric ceramic) is poled along the axis 3[49], many parameters of (3.28) and (3.29) become zero or can be expressed in terms of other parameters. Table 3.3 shows the equivalence parameters for a transversely isotropic piezoelectric material[48].

Table 3. 3 Non-zero coefficient for transversely isotropic piezoelectric materials

Non-zero coefficients		
Compliance	**Piezoelectric strain**	**Dielectric**
$S_{11} = S_{22}$		
$S_{13} = S_{31} = S_{23} = S_{32}$	$d_{31} = d_{32}$	$\varepsilon_{11} = \varepsilon_{22}$
$S_{12} = S_{21}$	$d_{15} = d_{24}$	ε_{33}
$S_{44} = S_{55}$		
$S_{66} = 2(S_{11} - S_{12})$		

With the information of Table 3.3, (3.28) and (3.29) can be simplified to

$$\begin{bmatrix} \xi_1 \\ \xi_2 \\ \xi_3 \\ \xi_4 \\ \xi_5 \\ \xi_6 \end{bmatrix} = \begin{bmatrix} S_{11} & S_{12} & S_{13} & 0 & 0 & 0 \\ S_{12} & S_{11} & S_{13} & 0 & 0 & 0 \\ S_{13} & S_{13} & S_{33} & 0 & 0 & 0 \\ 0 & 0 & 0 & S_{44} & 0 & 0 \\ 0 & 0 & 0 & 0 & S_{55} & 0 \\ 0 & 0 & 0 & 0 & 0 & 2(S_{11} - S_{12}) \end{bmatrix} \begin{bmatrix} T_1 \\ T_2 \\ T_3 \\ T_4 \\ T_5 \\ T_6 \end{bmatrix} + \begin{bmatrix} 0 & 0 & d_{31} \\ 0 & 0 & d_{31} \\ 0 & 0 & d_{33} \\ 0 & d_{15} & 0 \\ d_{15} & 0 & 0 \\ 0 & 0 & 0 \end{bmatrix} \begin{bmatrix} E_1 \\ E_2 \\ E_3 \end{bmatrix} \tag{3.30}$$

and

$$\begin{bmatrix} D_1 \\ D_2 \\ D_3 \end{bmatrix} = \begin{bmatrix} 0 & 0 & 0 & 0 & d_{15} & 0 \\ 0 & 0 & 0 & d_{15} & 0 & 0 \\ d_{31} & d_{31} & d_{33} & 0 & 0 & 0 \end{bmatrix} \begin{bmatrix} T_1 \\ T_2 \\ T_3 \\ T_4 \\ T_5 \\ T_6 \end{bmatrix} + \begin{bmatrix} \varepsilon_{11} & 0 & 0 \\ 0 & \varepsilon_{11} & 0 \\ 0 & 0 & \varepsilon_{33} \end{bmatrix} \begin{bmatrix} E_1 \\ E_2 \\ E_3 \end{bmatrix} \quad (3.31)$$

3.4 Ferroelectric materials

From the 32 crystal classes mentioned in section 3.3, 21 are non-centrosymmetric, and in 20 of those 21 groups, the lack of inversion symmetry leads them to show the piezoelectricity property. From those 20 crystal types, only 10 have a spontaneous electrical polarization, which means that they have a non-vanishing dipole moment per unit of volume and are called polar[50]. When a change in temperature is produced into a polar crystal, the internal or external electrical conduction cannot provide enough current to compensate for the changes of polarization produced by the temperature, so the crystal develops an electric charge on its surface[50]. This effect is called the pyroelectric effect, which makes that polar crystals are called pyroelectric crystals. The pyroelectric effect analysis is not going to be included in this work.

Ferroelectric materials are a subgroup of the polar materials, which means that ferroelectrics possess both pyroelectric and piezoelectric properties, and they can be differentiated from other pyroelectric crystals due to the fact that ferroelectrics can reverse or produce a reorientation of its spontaneous polarization P_s. The spontaneous polarization can be defined as the magnitude of the polarization at the absence of an applied electrical field, which is a fundamental characteristic of polar crystals[50]. A ferroelectric crystal has two or more stable orientation of its spontaneous polarization in the absence of an applied electrical field, and it can be switchable from one to another state by a realizable electric field. A ferroelectric crystal has regions where it exhibits homogeneous and uniform spontaneous polarization. Those regions are called domains, and a ferroelectric material can have a complex domain structure consisting of many domains, each with a different polarization orientation. The boundary between regions that separates two domains is known as the domain wall[50].

The polarization response of a ferroelectric material with respect to the applied electric field can be described by the hysteresis loop shown in Fig. 3.5. Starting from the point where the polarization and the electric field is equal to zero, after increasing the electrical field, the polarization increases until it reaches a point where it saturates. This saturation of the polarization means that all the domains were completely oriented onto the direction of the electrical field. If the saturation of the polarization were extrapolated to the point of zero electrical field, it would correspond to the spontaneous polarization. When decreasing

the electrical field back to a zero value, the polarization decreases as well but remains with an amount of polarization at the zero point; this is called the remnant polarization P_r. Ideally, P_s and P_r should be identical, but in reality, P_s is higher because the formation of opposite domains when decreasing the field to zero, but it can be very close in single crystals[51]. When reducing the electric field to negative values, the polarization switches at a specific value of the electrical field until it reaches its saturation point. At this moment, if the electrical field is increased, the polarization increases again, switching its state at a specific value of the electrical field, and the whole process is repeated. The value of the electrical field that produces that switches in the polarization state is known as the coercive field (E_c); the whole process of changing the polarization state is known as the polarization switching. The switching process occurs through nucleation and growth of domains that are favourably oriented with respect to the electrical field[50].

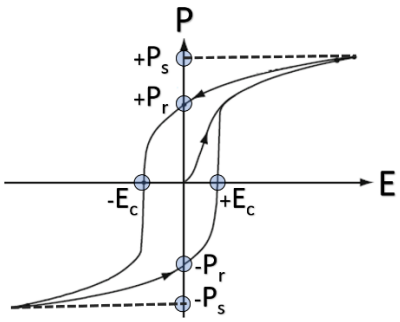

*Fig. 3. 5. Hysteresis response of the ferroelectric polarization (*P*) in an applied electrical field (*E*)*[52].

In most ferroelectrics, there is a phase transition from the ferroelectric phase, to a nonpolar paraelectric phase while increasing the temperature[52]. The temperature value that produces this phase transitions ranges from 1 °K to over 1000 °K, and there is the possibility that the material melts before reaching this temperature[52]. At the paraelectric phase, the material does not exhibit spontaneous polarization, but as it is cooled down below a critical temperature point called Curie temperature T_c, it undergoes a lower crystal symmetry phase that allows the spontaneous polarization[53].

3.5 Piezoelectric Ceramics

For many years, natural crystals such as quartz and tourmaline were the sole source of piezoelectric capabilities. However, at the end of the Second World War, independent groups in the former Soviet Union and the United States revealed a new man-made ferroelectric material consisting of $BaTiO_3$ in a polycrystalline ceramic form[20]. It was created by making a balanced mixture with an appropriate binder, followed by pressing and then heated at a high temperature. Regions (or domains) of the same polarization direction are formed within the polycrystalline, and these are bounded by other domains with

different polar directions. By applying a high DC electric field at a temperature close to the Curie point and with the field present when the temperature is lowered, many of the domains become aligned with the applied electrical field, and some grow in volume, enhancing the piezoelectric properties of the material. This process is called poling[20]. Fig. 3.6 represents the poling process. In addition to the high piezoelectric enhancement, piezoelectric ceramics have an important advantage as they can be fabricated into different shapes.

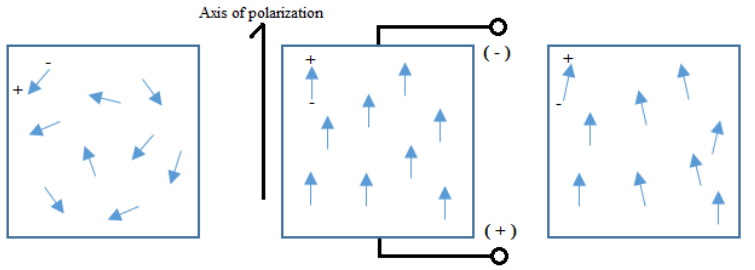

Fig. 3. 6. Poling process of a piezoelectric ceramic. (a) Random orientation of polar domains prior to polarization. (b) Polarization in DC electric field. (c) Remanent polarization after electric field removed[54].

After these developments, in 1954 Jaffe *et al.*[55]reported strong piezoelectric effects in lead-zirconate and lead-titanate solid compositions. This led to the development of a wide variety of polycrystalline lead-zirconate-titanate {$Pb(Zr_{1-x},Ti_x)O_3$} ceramics, which are better known as PZT[20].

3.6 Material parameters

3.6.1 Piezoelectric constant

The piezoelectric constant d_{ij} represents, for the inverse piezoelectric effect, the mechanical strain experienced in the *j*-axis by a piezoelectric material per unit of the electrical field applied at the *i*-axis[54] when all external stresses are held constant. When a voltage V is applied to a piezoelectric material with thickness t_h that is polarized along the axis 3 (Fig. 3.7), this voltage generates the electric field[48]

$$E_3 = \frac{V}{t_h} \tag{3.32}$$

which strains the length l of the material

$$\xi_1 = \frac{\Delta l}{l} \tag{3.33}$$

for

$$\Delta l = \frac{d_{31} V l}{t_h} \tag{3.34}$$

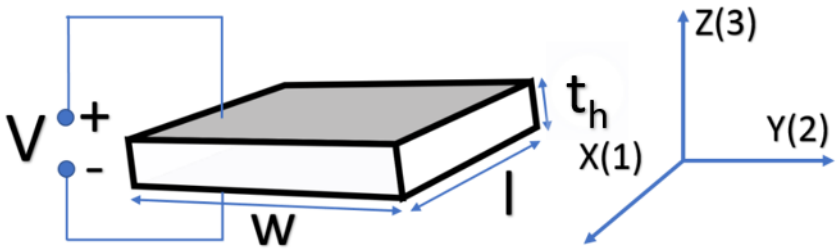

Fig. 3. 7. Voltage applied to a piezoelectric material poled along the axis 3. w, l and t_h are, respectively, the width, length and thickness of the material.

For the direct piezoelectric effect, the piezoelectric constant d_{ij} represents the charge per unit of area flowing between electrodes (connected in a short-circuit) perpendicular to the *j*-axis by applying stress in the *i*-axis[48]. When a force F is applied to a piezoelectric material with width w and length l (poled at axis 3) in direction 3, it generates the stress described by

$$T_3 = \frac{F}{lw} \tag{3.35}$$

resulting in the electric charge q flowing through the short circuit (Fig. 3.8)

$$q = d_{33} F \tag{3.36}$$

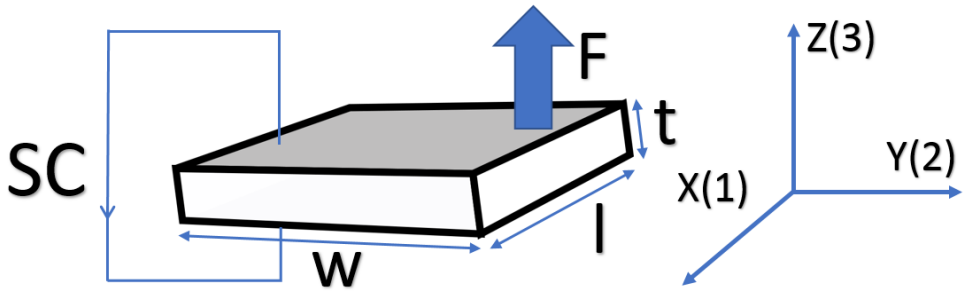

Fig. 3. 8. Force (F) applied to a piezoelectric material poled along the axis 3. An equal, but opposite force F is not shown[48]. SC = short circuit.

3.6.2 Elastic Compliance

The elastic compliance S_{ij} can be described as the ratio of the strain in the *i*-direction to the stress in the *j*-direction, considering that there are no stresses at the other directions[48]. Sometimes, the elastic compliance can be expressed with a superscript, E or D, to represent that the measurement was taken with a constant electric field (electrodes short-circuited) or electric displacement (electrodes open-circuited), respectively.

3.6.3 Dielectric coefficient

The dielectric coefficient, or permittivity, ε_{ij} for a piezoelectric material determines the charge per unit area in the *i*-axis due to an electric field applied in the *j*-axis[48]. Sometimes, the permittivity can be expressed with a superscript, ξ or T, to represent that the measurement was taken with a constant strain or stress, respectively. The relative dielectric constant, defined as the ratio of the absolute permittivity of the material by the permittivity of the free space ε_0, is denoted by k.

3.6.4 Piezoelectric coupling coefficient

The piezoelectric coupling coefficient or electromechanical coupling coefficient k_{ij} is an indicator of the effectiveness with which a piezoelectric material converts electrical energy into mechanical energy (direct piezoelectric effect) or mechanical energy into electrical energy (inverse piezoelectric effect)[54]. One way to calculate k_{ij} is to apply a force to the piezoelectric element. The element will deflect (Δz) and mechanical work (W_M) done by the applied force F can be calculated with

$$W_M = \frac{F\Delta z}{2} \tag{3.37}$$

Due to the piezoelectric effect, the electrical charge q will be accumulated on the electrodes and not flowing through them (open-circuit). This amount of energy (E_w) can be calculated by

$$E_w = \frac{q^2}{2C_p} \tag{3.38}$$

which is stored in the piezoelectric capacitor C_p. Therefore

$$k_{33} = \sqrt{\frac{E_w}{W_M}} = \frac{q}{\sqrt{F\Delta z C_p}} \tag{3.39}$$

and expressed in terms of the others piezoelectric constants[48]

$$k_{ij}^2 = \frac{d_{ij}^2}{S_{ij}^E \varepsilon_{ij}^T} \tag{3.40}$$

3.6.5 Dielectric dissipation factor

The dielectric dissipation factor, $\tan\sigma$, express the parasitic loss that results by subjecting a material to alternating electrical fields. It is a measure of the electrical loss of the materials. When an electrical field, E, is applied to an ideal dielectric material, the resultant charging current finds itself out phase by 90° with the applied electrical field. However, in a real ferroelectric material, the current also has a loss component in phase with the applied E, and the resultant net current makes an angle σ with the ideal charging current. This loss current is a result of the dissipation of energy heat. This loss can be interpreted using the parameter σ which is the ratio of loss current I'' and charging current I'[54].

$$\tan(\sigma) = \frac{I''}{I'} \tag{3.41}$$

Typical values for some of the above parameters, for some common materials, are listed on Table 3.4.

Table 3. 4 Piezoelectric material properties[56]

	Quartz	PZT-4	PZT-5A	Lead metaniobate	PVDF
Dielectric constant	5.0	1300	1700	22.5	8
Coupling factor: k_{33}	0.1	0.7	0.7	0.38	0.19
Piezoelectric constant: d_{33}	2	290	370	85	17.5
Dissipation factor: $\tan\sigma$	10^{-4}	0.004	0.02	0.01	-
Acoustic impedance: $Z(10^6\ Rayl)$	15.2	34.5	33.7	20	3.4

3.7 Ultrasound transducer

An ultrasound transducer is a device capable of generating or detecting ultrasound waves[37]. The classical single-element transducer is based on a piezoelectric plate, disc or ring poled along the thickness direction and used in its thickness mode, so its thickness defines the f_r of the device through the relation: thickness = half wavelength. When an electrical impulse is applied to the plate, an acoustical resonance is induced, which will lead the generation of pressure waves both in the front and back direction. On the rear face of the active element, a thick layer is usually added and is referred to as backing. It serves as a mechanical support for the active element, but it also allows acoustic energy to flow by the rear face and thus induces damping of the transducer resonance. Between the piezoceramic and the propagation medium, one or several matching layers are used. Their design is optimized to increase the transfer of

energy from the active layer to the propagation medium. Typically, the thickness of this layer is around a quarter wavelength of f_r [57]. Fig. 3.9 shows the typical configuration of a single element transducer.

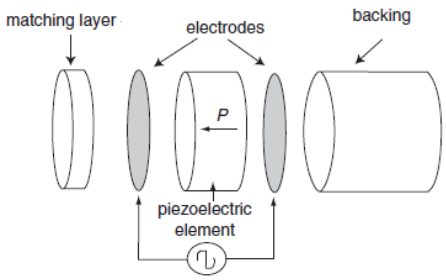

Fig. 3. 9. Essentials of a single-element transducer assembly[57]. P = poling axis in the thickness direction.

3.7.1 Polyvinylidene Fluoride Transducers

The acoustic impedance mismatch between water and PZT or other ceramics has motivated a shift in the focus in material development to include piezoelectric polymers, most notably Polyvinylidene Fluoride (PVDF). PVDF is a fluoropolymer whose piezoelectricity was discovered by Heiji Kawai in 1969 and is a common materials used in acoustic imaging devices[58]. Typical piezoelectric polymers have a crystalline region with a dipole moment randomly oriented without any mechanical or electrical poling process with a net dipole moment equal to zero in this condition. This type of structure is called the α-phase PVDF film and has not a piezoelectric response[59]. By applying a mechanical stretching and electrical poling under a high electric field, crystalline regions inside the bulk PVDF film will align in the electric field direction. This type of structure is called the β-phase PVDF film and exhibits piezoelectricity[59]. One of its most important applications is broadband hydrophones [58].

3.7.2 Piezocomposite transducers

Conventional piezoelectric ceramics such as PZT, lead metaniobate and modified lead titanates are useful for making ultrasonic transducers used in medical imaging because of their high electromechanical coupling coefficients. Their principal limitation lies in their high acoustic impedance, which makes coupling to tissue difficult. Piezoelectric polymers, such as polyvinylidene difluoride (PVDF), present a different set of material properties. Their low acoustic impedance simplifies efficient coupling, but their low electromechanical coupling, low dielectric constant and high dielectric losses show additional limitations when integrating these materials into medical imaging transducers[60]. Simply stated, a piezocomposite is a combination of a piezoelectric ceramic and a non-piezoelectric polymer to form a new piezoelectric material with the properties enhanced. In general, however, the term piezocomposite applies to any piezoelectric resulting from combining any piezoelectric polymer or ceramic with other non-piezoelectric

material[61]. The advantage of such an arrangement is that it combines the superior piezoelectric properties of the chosen ceramic with the lower acoustic impedance of the polymer[20]. This type of transducers is fabricated with common piezoelectric materials, but not in one piece. The material is selected and filled with a vibration absorbent material to isolate cuts on the piezoelectric[37]. In a two-phase system, e.g., ceramic and polymer, there are ten possible connectivities, of which only a few are of practical interest for transducer fabrication[20].

3.7.3 Capacitive micromachined ultrasound transducer (CMUT)

A CMUT is a micromachined transducer formed from numerous unit cells electrically connected in parallel, with each cell consisting of a metalized membrane suspended above a heavily doped silicon substrate (top and bottom electrodes, respectively)[62]. Fig. 3.10 represents a CMUT unit cell.

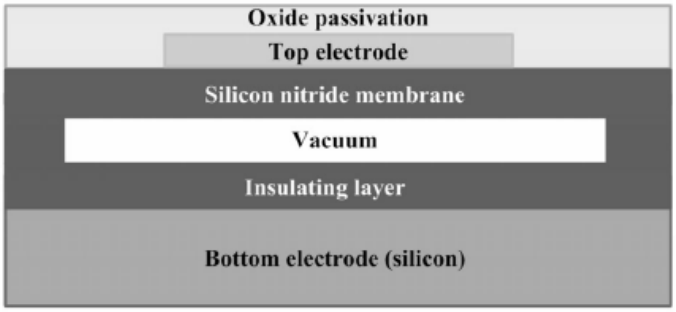

Fig. 3. 10. Schematic cross-section of a CMUT unit cell[62].

During operation, a DC voltage is applied between both electrodes. This DC bias voltage causes the membrane to deflect downward to a static operating point, which determines the sensitivity, frequency response and total acoustic pressure[53]. If an alternating voltage is superimposed on the bias voltage, then the modulation of the electrostatic force results in the vibration of the membrane with subsequent generation of ultrasonography at the same frequency of the modulation[55]. Conversely, if the biased membrane is subjected to ultrasound waves, an output current is generated as a result of the capacitance changes due to membrane vibrations.

The advances in microfabrication technology have made building capacitive ultrasound transducers possible, which can compete with piezoelectric transducers. CMUTs offers advantages of improved bandwidth, ease of fabrication of large arrays with individual electrical connections, and integration with electronics[62]. CMUTs are fabricated using silicon micromachining methods with submicrometer accuracy and uniformity, which allow fabrication flexibility. Since silicon micromachining determines the

shapes, sizes and spacing between neighbouring elements, flexible shapes and multiple elements with transducer spacing as small as 3 µm can be fabricated[63].

Besides medical and underwater imaging, CMUTs have some potential applications that include air-coupled non-destructive evaluation[64], microphones with RF detection[65] and smart microfluidic channels[66].

3.8 Acoustic propagation and acoustic waves

The physical nature of the medium where an acoustic wave is going to propagate can be modelled as stationary, with a spatially varying density $\rho_0(r)$, where r denotes the location vector with Cartesian components (*x,y,z*). If we first consider only the one-dimensional arrangement, the medium may be considered to be specified by its constant pressure p_0, and by its varying density, $\rho_0(x)$. The static state of the medium will be perturbed in the presence of a propagation pressure wave, and the total (time-varying) pressure p_T at the location *x* will be denoted by[56]

$$p_T(x,t) = p_0 + p(x,t) \tag{3.42}$$

where t denotes time and p, the pressure perturbation caused by the wave is called the "acoustic pressure". Furthermore, the density of the medium will also be disturbed by the wave, and the total, time-varying, density can be written as

$$\rho_T(x,t) = \rho_0(x) + \rho(x,t) \tag{3.43}$$

A passing ultrasound wave not only modifies the density and pressure of the supporting medium but also sets it into local motion, displacing small elements of the medium and imparting them with a particle velocity, *u(x,t)*. The displacement at time *t*, of the particle that was located at x at some reference point (normally *t = 0*) is called the particle displacement and is noted as $\delta(x,t)$.

The force acting on any element of the continuous medium then depends on the pressure gradient, and Newton's second law may be written as

$$-\frac{\partial p_T}{\partial x} = \rho_T \frac{Du}{Dt} \tag{3.44}$$

The time derivative $\frac{Du}{Dt}$ has its conventional meaning of total rate of change with time

$$\frac{D}{Dt}[u(x,t)] \equiv \lim_{\Delta t \to 0} \frac{u(x+\Delta x, t+\Delta t) - u(x,t)}{\Delta t} \tag{3.45}$$

where $x + \Delta x$ indicates the new spatial position that the particle located initially at x, at time t. has moved to during the time interval Δt. And we have that

$$\Delta x = u(x,t)\Delta t \tag{3.46}$$

And an application of Taylor´s expansion theorem results in

$$\frac{D}{Dr}[u(x,t)] = \frac{\partial u}{\partial t} + u\frac{\partial u}{\partial x} \tag{3.47}$$

Using (3.47) to reduce (3.44)

$$-\frac{\partial p_T}{\partial x} = \rho_T \frac{\partial u}{\partial t} + \rho_T u \frac{\partial u}{\partial x} \tag{3.48}$$

It is assumed that the wave produces only small perturbations

$$\left|{}^{p}/_{p_0}\right| \ll 1;\ \left|{}^{\rho}/_{\rho_0}\right| \ll 1 \tag{3.49}$$

If only the dominant terms no higher than first order are retained, then the of motion may be expressed by

$$-\frac{\partial p}{\partial x} = \rho_0 \frac{\partial u}{\partial t} \tag{3.50}$$

(3.50) implies that any local change in the density of the medium must be the result of the exchange of mass between the surroundings and the location under consideration. Since the mass flux across a plane fixed in space, at location *x*, is given $\rho_T(x,t)u(x,t)$, the continuity, for mass conservation, can be written as

$$-\frac{\partial \rho_T}{\partial t} = \frac{\partial}{\partial x}[\rho_T u] \tag{3.51}$$

Linearization of (3.51) results in

$$-\frac{\partial \rho}{\partial t} = \rho_0 \frac{\partial u}{\partial x} \tag{3.52}$$

One particularly simple constitutive equation is to limit that any change in the local density induced by the wave is some function, G, of the acoustic pressure only, i.e.

$$\rho = G(p) \tag{3.53}$$

with $G(0) = 0$ and considering only small acoustic pressure excursions, a Taylor expansion gives

$$G(p) = \left[\frac{dG}{dp}\right]_{p=0} p + \text{neglible higher-order } p\text{-terms} \tag{3.54}$$

After excluding the higher-order terms in p, a linearized constitutive equation is given by

$$\rho = \left[\frac{d\rho}{dp}\right]_{p=0} p \equiv \rho_0 \beta_0 p \tag{3.55}$$

where the compressibility of the medium, β_0, is given by

$$\beta_0 \equiv -\frac{1}{V}\left[\frac{\partial V}{\partial p}\right]_{ad} = \frac{1}{\rho_0}\left[\frac{\partial \rho}{\partial p}\right]_{ad} \tag{3.56}$$

with V denoting the volume of a region of the unperturbed medium that contains a fixed mass of material, and which is small enough for the density to be regarded as virtually constant throughout the material. (3.50), (3.52) and (3.55) can be combined to give a wave for the pressure,

$$\frac{\partial^2 p}{\partial x^2} - \frac{1}{c_0^2}\frac{\partial^2 p}{\partial t^2} = \left(\frac{\partial}{\partial x}\ln\rho_0\right)\frac{\partial p}{\partial x} \tag{3.57}$$

with $c_0^2 \equiv (\rho_0 \beta_0)^{-1}$. (3.57) can be converted into a more physically transparent canonical form by introducing density and compressibility fluctuation terms ($\tilde{\rho}$ and $\tilde{\beta}$ respectively) defined as

$$\tilde{\rho} = \frac{\rho_0 - \bar{\rho}}{\rho_0} \tag{3.57A}$$

$$\tilde{\beta} = \frac{\beta_0 - \bar{\beta}}{\beta} \tag{3.57B}$$

Here, $\bar{\rho}$ and $\bar{\beta}$ denote the spatial mean values of the density and compressibility. With some algebraic manipulations, (3.57) can be transformed into

$$\frac{\partial^2 p}{\partial x^2} - \frac{1}{\bar{c}^2}\frac{\partial^2 p}{\partial t^2} = \frac{1}{\bar{c}^2}\tilde{\beta}\frac{\partial^2 p}{\partial t^2} + \frac{\partial}{\partial x}\left[\tilde{\rho}\frac{\partial p}{\partial x}\right] \tag{3.58}$$

where $\bar{c} \equiv 1\Big/\sqrt{\bar{\rho}, \bar{k},}$ and which has a constant positive value, dependent only on the physical properties of the medium. The three-dimensional form of (3.58) is

$$\nabla^2 p - \frac{1}{c^2}\frac{\partial^2 p}{\partial t^2} = \frac{1}{\bar{c}^2}\tilde{\beta}\frac{\partial^2 p}{\partial t^2} + \nabla \cdot [\tilde{\rho}\nabla p] \tag{3.59}$$

where p now is a function of three-dimensional variable, r, and the time, t. If $\tilde{\rho}$ and $\tilde{\beta}$ vanish (uniformly constant density and compressibility medium), then the wave propagation is described by the homogeneous equation

$$\nabla^2 p - \frac{1}{c^2}\frac{\partial^2 p}{\partial t^2} = 0 \tag{3.60}$$

where for notational convenience, $\bar{c}$ has been replaced by $c \equiv {1}\Big/{\sqrt{\rho_0 \beta_0}}$ which represents the speed of sound as a function of the compressibility and density of the medium[56].

3.9 Ultrasound in medical applications

Ultrasound technology offers a wide variety of advantages in medical applications, which includes being totally harmless to the human body when low intensities are used, in contrast to ionizing radiation imaging modalities; it does have a real-time capability to reconstruct images of the body due to the fact that the time it takes an ultrasound wave to cover the distance of the intended reconstructed zone is short due the speed of sound in soft tissues has values around ~1540 ms^{-1}. Ultrasound imaging is cost-effective as it does not require a large infrastructure as the RF shielded rooms of magnetic resonance or expensive and dangerous materials such as nuclear medicine[19]. Ultrasound in the medical field can be found in a wide range of applications, which can be divided into two major categories, diagnostic and therapeutic applications and the frequency used on any specific application is based on the considerations of sound absorption, penetration and resolution[67].

3.9.1 Diagnostic ultrasound

Diagnostic medical sonography (sometimes called ultrasonography) is an ultrasound-based imaging technique used to visualize subcutaneous body structures such as tendons, muscles, joints and internal organs[2]. Sonography is typically performed with a hand-held probe called ultrasound transducer, which is placed and moved over the patient body. Water-based gels are used as a coupling between the probe and the body. Usually, the frequency range for ultrasonography lies between 2 and 18 MHz and is very common for clinic imaging of soft tissues[2].

Commonly, ultrasound imaging systems use the pulse-echo measurement technique[68], which is represented in Fig. 3.11-A. The main component of this technique is the transducer, which serves for both the generation of ultrasound waves toward the desired reconstruction object and to detect the acoustic echoes produced by that object. When the ultrasound wave is generated, it travels through a medium until it reaches an object with different acoustic impedance (Fig. 3.11, B), where part of the wave is reflected by the object to the transducer and part of it travels through it (Fig. 3.11, C). The reflected wave or echo is then reconverted into an electric signal by the transducer. A transmitter electronic circuit is used to generate the electric signal used to drive the ultrasound transducer to produce the ultrasound

wave, and a receiver circuit is used to amplify, rectify and demodulate the electrical echo signal produced by the transducer when receiving the acoustic echo. With the known speed of sound c of the medium and the time t the echo took to reach the transducer, the distance d of the object can be calculated as

$$d = \frac{ct}{2} \tag{3.61}$$

By knowing the distance of the object and the amplitude of the echo signal an image can be reconstructed and displayed.

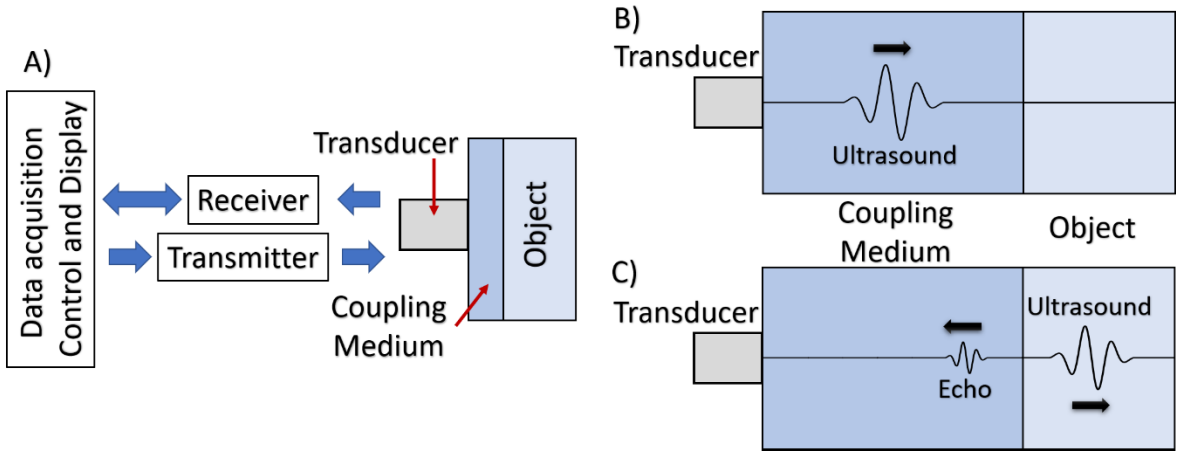

Fig. 3. 11. Ultrasound pulse-echo system. A) Simplified diagram of a pulse-echo system. B) Ultrasound generation from the transducer. C) Echo produced by an object of different acoustic impedance.

There are mainly four different modes for ultrasound imaging, The A-mode or amplitude mode, B-mode or brightness mode, M-mode or motion mode and the doppler mode.

3.9.1.1 The A-mode

The amplitude mode is the oldest and most basic of the four. In the A-mode display data, the vertical axis represents the amplitude of the registered echo, while the horizontal axis represents the time or distance. This mode is primarily used to make internal distance measurements.

3.9.1.2 The B-mode

The B-mode is the most popular imaging method based on ultrasound. Within the medical applications, an image reconstruction with B-mode is a cross-sectional image representation of tissues within the body generated by the echoes produced by the boundaries and scattering of the tissue of tissue irregularities. Each echo is represented as a point in the reconstructed image relative to the position of the reflector object, and the amplitude of each echo describes the brightness or shade of gray at each pixel of the

image[41]. Finally, the reconstructed 2D image is formed by concatenating multiple pulse-echo lines and the physical scanning required to acquire the number of pulse-echo lines can be effected in two ways:

- A physical movement of the ultrasound transducer with a fixed beam axis.
- An electronically controlled positioning of the acoustic beam using an array of transducers.

The echoes detected by the transducer or array of transducers may have many rapid changes in the amplitude due to the many reflections that the wave encounter along its path, which may produce false detections on the reconstruction. Due to this, the envelope of the signal $S(t)$ is used and can be calculated by using the Hilbert transform $Hl\{\}$ defined as[69]

$$Hl\{S(t)\} = \frac{1}{\pi}\int_{-\infty}^{\infty}\frac{S(\tau)}{(t-\tau)}d\tau \tag{3.62}$$

$$Hl(\omega) = -j\cdot sign(\omega) \equiv \begin{cases} -j & \omega > 0 \\ j & \omega < 0 \end{cases} \tag{3.63}$$

which changes the phase of negative and positive frequencies by 90° and -90° respectively and the envelope $\boldsymbol{S}(t)$ of the signal can be calculated with[19]

$$\boldsymbol{S}(t) = |S(t) + jHl\{S(t)\}| \tag{3.64}$$

Lastly, to convert the signal into grayscale values $\widetilde{\boldsymbol{S}(t)}$ a display window $\{GS_{min}, GS_{max}\}$ and the number of scale levels Ng are required to be set with[19]

$$\widetilde{\boldsymbol{S}(t)} = \begin{cases} \boldsymbol{S}(t) < GS_{min} \rightarrow Black \\ \boldsymbol{S}(t) > GS_{max} \rightarrow White \\ else \quad \widetilde{\boldsymbol{S}(t)} = round\left\{Ng\cdot\frac{(\boldsymbol{S}(t) - GS_{min})}{(GS_{max} - GS_{min})}\right\} \end{cases} \tag{3.65}$$

Received signals from deeper distances suffer more attenuation producing a significant reduction in amplitude. To partially compensate this attenuation, an amplification over time called time-gain-compensation (TGC) is typically implemented into the electronic receiver circuit. The compensated signal $S_c(t)$ can be described by

$$S_c(t) = S(t)e^{+\alpha f t} \tag{3.66}$$

with α representing the attenuation factor.

3.9.1.3 The M-mode

The M-mode is used to observe the motion of moving reflectors[67]. It employs the B-mode principle, the ultrasound transducer is placed in front of a moving target and echoes signals are repeatedly acquired in the same position. The resulting image enabled the movement and velocity of specific structures. A calculation of the M-mode slope's trace at any instant of time gives the instantaneous velocity of the reflector[70]. It is used in non-invasive cardiac diagnosis[20].

3.9.1.4 The Doppler mode

The Doppler shift detection measures the rate of change of phase in the reflected signal from a moving target relative to the transmitted signal[56]. By considering that the ultrasound transducer produces an acoustic wave of frequency f which propagates at a speed of sound c which encounters a blood vessel with a blood flow of instantaneous velocity $\vec{v}$. The angle between the acoustic beam and the blood vessel's axis is θ_b as shown in Fig. 3.12. The blood cells can reflect the acoustic wave, but the frequency of the echo has changed to f' due to the doppler effect. The induced frequency change is given by[41]

$$\Delta f = \frac{2f\vec{v}\cos\theta_b}{c} \tag{3.67}$$

The angle θ can change due to the vessels or transducer orientation. Also, as the speed of sound is not constant through the body, there is an error due to the speed of sound ratio induced[19]. In addition to the visualization of the blood flow, the doppler shift detection can also be used to detect fetal heart rate[67].

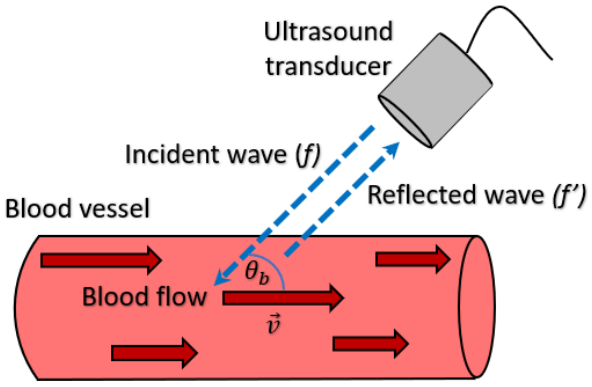

Fig. 3. 12. Ultrasound wave frequency shift produced by the blood flow.

3.9.2 Contrast, Signal-to-noise ratio and Spatial resolution

For the two-dimensional images produced by the ultrasound transducer through the conversion of the echoes amplitude into pixel intensity, the ability to distinguish between the echo amplitudes of two neighbouring regions is called contrast. Contrast can be measured by using[71]

$$\text{Contrast} = \frac{S_{out} - S_{in}}{S_{out}} \tag{3.68}$$

where S_{in} is the mean signal measured inside the region of the object and S_{out} the average signal measured in the same region without the object. The minimum contrast required to differentiate an object from the noise is called contrast resolution[72].

Noise in an image can be defined as an unwanted signal coming from sources different than the imaged object. Those unwanted sources include the transducer, preamplifier, acoustic interferences or the medium itself. A standard method to evaluate the quality of the acquired image is by using the signal-to-noise ratio (*SNR*)[19], which for an ultrasound imaging system depends on the differentiation of the acquired meaningful echoes from the produced noise. The *SNR* can be calculated as

$$\text{SNR} = \frac{\mu_S}{\sigma_n} \tag{3.69}$$

where μ_S is the average signal and σ_n the standard deviation of the noise.

Another parameter to measure the quality of an image is the smallest separation of which two adjacent objects can be differentiated, which is called the spatial resolution and is classified in axial and lateral resolution. The axial resolution describes how close two objects in an image can be differentiated from each other along the ultrasound propagation axis and can be computed from the period T and the speed of sound as[73]

$$\text{Axial resolution} = \frac{cT}{2} \tag{3.70}$$

The minimum separation at which two different objects can be differentiated on the axis perpendicular to the direction of the ultrasound beam is called lateral resolution. The spatial resolution can be affected by the length of the transmitted ultrasound pulse and the degree of focusing[74].

3.9.3 Therapeutic ultrasound

The application for the ultrasound in therapy “predates its use in imaging”[75]. During 1917, Paul Langevin was the first person to observe that ultrasonic energy could have a detrimental effect on biological

material[76] by reporting that 'fish placed in the beam in the neighbourhood of the source operation in a small tank were killed immediately, and certain observers experienced a painful sensation on plunging the hand in this region'. A decade after (1927), Wood and Loomis investigated Langevin's observations, showing with experimental studies that ultrasonic energy had a range of effect from a rupture of Spirogyra and Paramecium to the death of small fishes and frog during a 1-2 min exposure time. This realization of the heating effect produced the idea that ultrasound could have potential applications for therapy.

The versatility of ultrasound in medical therapies relies on the interaction with the cells and tissues. The mechanisms that describe the tissue-ultrasound interaction include the heating or thermal mechanisms and the non-thermal mechanisms, which include cavitation (growth and collapse or motion of bubbles), gas body activation or mechanical stress[77]. The type of effects produced by the interaction of the tissues with ultrasound waves depends on several parameters, but the most important are the attenuation, frequency, duty cycle and amplitude of the ultrasound wave[78].

3.9.3.1 Thermal mechanisms

The intensity of the acoustic wave is attenuated as it passes through the body, as described by (2.5). The absorption mechanisms of tissues are the main factor of heat generation as the acoustic energy is converted in a temperature elevation, which is different for every tissue due to the fact that the attenuation coefficient depends of the composition of the structure. Solid structures within the body, bones and teeth, for example, tend to have a higher attenuation coefficient than soft tissues and hence the heating produced due to absorption is also higher. The attenuation coefficient is also dependent of the frequency, with a tendency of higher frequencies producing higher attenuations. The biological effects produced by the ultrasound-induced heating depend mainly on the magnitude and duration of the ultrasound exposure, and the sensitivity of the targeted tissues[19]. If we consider the ultrasound wave as a source of heating $\dot{Q}$ and in the case where blood flow works as a cooling mechanism, the temperature rise in tissue can be described with the bioheat transfer function[67], [79]

$$\rho_t C_t \frac{\partial T}{\partial t} = k_t \nabla^2 T - W_b C_{tb}(T - T_b) + \dot{Q} \tag{3.71}$$

Where ρ_t, C_t, k_t and T correspond to the density, specific heat, thermal conductivity and temperature of the tissue respectively, and W_b, C_{tb} and T_b to the perfusion, specific heat and temperature of the blood, respectively. (3.71) can be solved numerically using the finite-difference time-difference and finite element methods[67].

The therapeutic applications based on the thermal mechanisms use a longer duration of heating for unfocused ultrasound beams or short durations for focused ultrasound (FUS) beams[77]. For the unfocused beams, the most common application is physiotherapy, which relies on the healing of highly absorbing tissues like bones or tendons. The focused beam applications are commonly used for tissue ablation, as is the case of the high intensity focused ultrasound[77].

3.9.3.1.1 High intensity focused ultrasound

High intensity focused ultrasound (HIFU), is a non-invasive thermal ablation technique used for the treatment[80] of tumours in the prostate, uterine fibroids, bone metastases and brain disorders such as refractory essential tremor[81]. It is also being studied for the treatment of tumours in pancreas, liver, kidney, breast, and sarcomas[80]. It is also used for the treatment of brain disorders such as refractory essential tremor[81]. The first suggestion that HIFU could be applied to therapy was made in 1942 by Lynn et al[80], [82] while studying the effects of focused ultrasound in beef liver and the brain of living cats and dogs. However, the first report of the application of HIFU into humans was made in 1954 by Fry et al[80], [83] while treating tissue related to Parkinson's disease.

The HIFU technique concentrates the ultrasound beam through the use of a concave focused transducer or an array of transducers. The focused transducer is placed near the desired treated zone and generates an ultrasonic beam which is concentrated on a focal zone. The temperature on the focal zone raises due to the absorption of the high acoustic energy until a lesion of a few mm in diameter is produced on the zone without damaging the surrounded tissues. The HIFU's principle of operation is illustrated in Fig. 3.13.

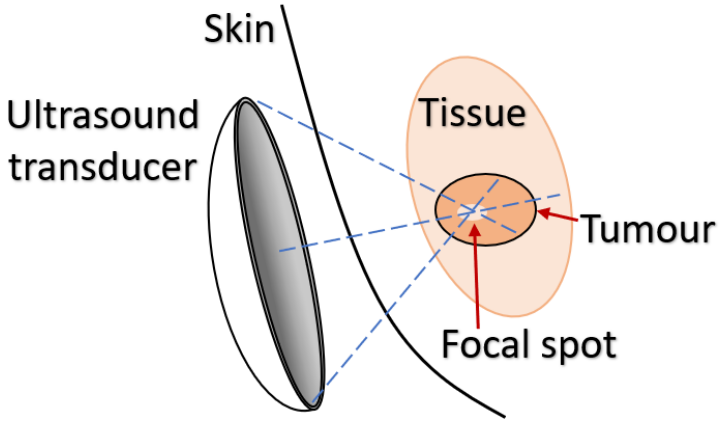

Fig. 3. 13. Operational principle of the high intensity focused ultrasound. The focal spot is placed within the target to produce an increment in temperature to generate a coagulative necrosis and cells death without damaging surrounding structures.

The temperature increment within the targeted tissue volume produced by the focal spot of the HIFU treatment is intended to be raised up to 55 °C or more for periods longer than 1 s to produce coagulative necrosis and immediate cell death[75] while keeping temperatures outside the treated zone at non-cytotoxic levels. The acoustic intensities produced at the focal spot have values greater than $1\ \mathrm{kW \cdot cm^{-2}}$ for driving frequencies of 0.5 – 7 MHz[77]. The focal spot has an elliptical shape similar to a cigar, and the size of the focal spot can reach values as small as 3-4 mm in length and 1-2 mm in diameter depending in the application[67].

The targeting of the treatment zone can be done with magnetic resonance imaging (MRI) or ultrasound imaging. The MRI approach provides the ability to produce high-quality anatomical images and real-time non-invasive temperature monitoring during the procedure at the expense of high costs and limited access to the patient. Ultrasound imaging is more cost-effective than MRI, but the image quality is inferior and does not provide real-time temperature monitoring. Under magnetic resonance guidance, HIFU is approved by the FDA for the treatment of uterine fibroids[3], [84], essential tremors[85] and pain palliation of bone-metastatic cancer[86]. Under ultrasound-guided, HIFU is approved by the FDA for the treatment of prostate cancer[87]. Many other indications (oncological and non-oncological) are at different research-level stages (from pre-clinical to clinical trials) including pancreatic cancer, liver cancer, epilepsy, Parkinson's disease-related motion disorder, just to mention a few[88].

3.9.3.2 Non-thermal mechanisms

The primary non-thermal mechanism is cavitation. According to Gail Ter Haar[67], cavitation can be defined as "the formation and activity of gas- or vapour-filled cavities (bubbles) in a medium exposed to an ultrasonic field". Two types of cavitation can be described, inertial and non-inertial. Inertial cavitation occurs when a gas-filled cavity oscillates violently, expanding during the ultrasound cycle and then collapsing abruptly to the size to a fraction of its initial volume. The collapse produces a high-pressure shock wave and high temperature within its microenvironment. The non-inertial cavitation is created when a low amplitude ultrasound wave is applied, producing oscillations of the bubble without collapsing, producing a rapid movement of the fluid surrounding it, which is called microstreaming[80].

The generation of cavitation bubbles during an ultrasound treatment is influenced by the magnitude of its respective negative peak pressure[19].

3.9.3.2.1 Histotripsy

High intensity focused ultrasound can produce thermal (section 3.9.3.1.1) and mechanical effects on tissues depending of the used parameters to produce ablation[89]. The mechanical HIFU ablation involves non-thermal effects for tissue destruction and is called histotripsy[90]. Histotripsy uses short (micro- to miliseconds) high amplitude burst of ultrasound waves to generate a cluster of microbubbles at the focal spot to fractionate down the targeted tissue by using the expansion and collapse of the bubbles[89]–[91]. The intensity of each pulse is higher than that of the HIFU thermal application, but the time-average intensity lower due to the burst having a low repetition frequency[89] and low duty cycle (<0.1%). With the proper number of pulses, the targeted tissues can be completely fractionated with no recognizable structures[91].

Within its advantages include that as it is not a thermal application, histotripsy is not affected by the heat sink effect of blood vessels[91], and as histotripsy is a pure mechanical fragmentation of tissue, the residual tissue debris can be drained or absorbed as part of the physiological healing response[90], which is an advantage over thermal ablation, where scar tissue is generated. It is non-invasive, and the tissue treatment can be monitored by using ultrasound imaging or MRI[91]. Animal studies have demonstrated that boiling histotripsy can properly fractionate lesions in kidney[92], heart[93] and liver[94] sharply demarcated between treated and untreated regions without thermal damage[95]. The first study in humans was treated for prostate hypertrophy in 25 patients while using shock wave scattering histotripsy. Transient improvement was an observer with no intraoperative complications and 1 case of urinary retention[96].

3.9.3.2.2 Blood-brain barrier opening

Many central nervous system diseases are challenging to treat due to the limitation of the amount of medication that can reach the diseased brain target because the larger molecule size can not adequately penetrate the blood-brain barrier (BBB)[97], [98]. The BBB is a physical barrier composed of endothelial cells tightly joined that lines the blood vessels in the brain and prevents harmful agents from diffusing into the surrounding brain tissue[97], [99]. Although it protects the brain from toxic agents, it also reduces the efficacy of brain targeted drugs, so safely and temporarily opening of the BBB is a goal for delivering drugs with therapeutic concentrations to treat neurological conditions. Several methods to overcome the BBB have been developed, including hyperosmotic agents that force water out of the endothelial cells to disrupt the tight junction between cells[100], invasive options like convection-enhanced delivery, which surgically implants a cannula to deliver drugs within the targeted region[101], and vasodilators like

bradykinin[102]. Usually, those approaches are limited by lack of specificity, safety concerns or inadequate drug concentration deliveries to brain tissue[103].

The combination of FUS and injected microbubbles (contrast agents) has demonstrated to be an effective method to open the BBB transiently[97], [99], [104]. The exact mechanism for which the FUS enhances the BBB permeability is not fully understood, but the leading hypothesis regarding it is that microbubbles formed through cavitation vibrate due to the ultrasound waves producing pressure on the endothelium, which widens the tight junction of the BBB[99]. Two common types of ultrasound contrast agents approved by the FDA are the lipid-coated Sonovue® and Definity®, and the protein-coated Optison®[99].

Phased-arrays are usually used to deliver the ultrasound waves due to their sub-millimetric targeting accuracy, with a driving frequency in the range of 0.4 MHz to 1.5 MHz with a pulse repetition frequency of 1 Hz with a 10 ms burst[99]. FUS-induced drug treatment is currently investigated for glioma[105], [106] and has already being used for BBB disruption in human patients with Alzheimer's disease[103] and amyotrophic lateral sclerosis[107].

3.9.3.2.3 Lithotripsy

Commonly known as extracorporeal shock wave lithotripsy (ESWL), this technique has been used since 1980 for treating stone related problems within the bladder, urethra or the kidney [77], [108]. The ESWL is a non-invasive ultrasound-based method that involves the generation, outside of the body, of a focused high amplitude pulsed ultrasound wave with center frequency around the 150 kHz[77] used to disintegrate calculi at a specific depth in tissues[108] based on two fundamental mechanisms, shock wave-related effects and cavitation phenomenon[4]. To properly deliver the acoustic energy to the stones, a coupling media which is normally water or a rubber sleeve filled with fluid, is used between the region of interest and the ultrasound generator. The stones are visualized by using an x-rays imaging system or ultrasound imaging. After approximately 3000 shock waves of 80 MPa peak pressure with a pulse repetition frequency of 2 Hz[77] a 2 mm stone can be reduced to debris and washed out through the urinary tract. During the lithotripsy treatment, the healthy surrounding tissue can be damaged and side-effects of the treatment include haematuria, renal colic, haematomas, pancreatitis and arrythmias[4].

Chapter 4: BIAXIAL DRIVING TECHNIQUE AND MODELLING

4.1 Biaxial Driving

Commonly used ferroelectric actuators are driven by applying the electric field along a poling axis to maximize their mechanical response[109]. Low coercivity and low hysteresis loss are desired properties for ferroelectric materials used in high power and high-frequency applications[29].

In addition to the reorientation of polar domains by an applied electrical field, a polarization rotation was proposed[110] to describe a piezoelectric enhanced response in PZN-PT and PMN-PT single crystals, where a non-aligned field alternates the material strain vectors between tetragonal and rhombohedral configurations[30]. During the structural transformation associated with the polarization rotation, the polarization vector P does not disappear, it just changes its direction and maintains a magnitude similar to the spontaneous polarization P_s[30]. Simulation results with ferroelectric switching in $PbTiO_3$[29] suggest that it is possible to reduce coercivity (threshold at which the polarization switching occurs) and, consequently, the energy dissipation during operation of ferroelectric transducers by employing a two-dimensional excitation with modulation on the applied electrical fields. The energy surface for single-domain ferroelectric $PbTiO_3$, calculated using first principles[110] modelling, is shown in Fig 4.1. The lowest energy corresponds to a tetragonal phase with four minima, and the highest energy corresponds to the cubic structures. If a system is allowed to have several alternative states, it will choose the one with the lowest energy[111]. The candidate to reach the opposite polarization state from the tetragonal state is the orthorhombic structure positioned at the saddle point of Fig. 4.1, with an energy of approximately 20 meV more than the tetragonal structure.

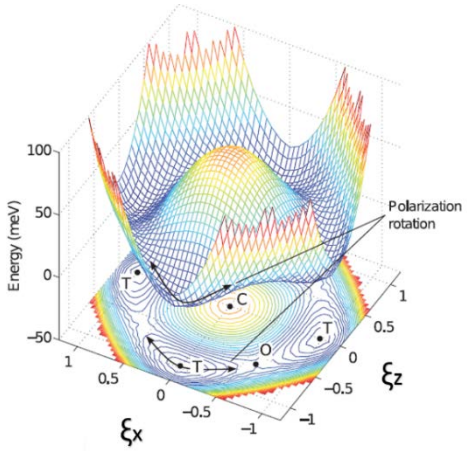

Fig. 4. 1. Energy surface for polarization inversion in the (0 1 0) plane of $PbTiO_3$.C, T and O refers to cubic, tetragonal and orthogonal structures, respectively. The arrows indicate the modulation of polarization in a rotational manner[30].

A natural way to describe a ferroelectric material is provided by the theory of phase transitions, which predicts the sudden disappearance of a given symmetry element leading to another element with lower symmetry[53]. Landau-Devonshire (LD) principle is an analysis of equilibrium behaviour near a phase transition based on the consideration of crystal symmetry. Landau characterizes the transition[112] in terms of an order parameter, which in the case of a paraelectric-ferroelectric transition is the polarization vector P, and the free energy at the vicinity of that transition region can be described as a power series of P. Without applying an electrical field, the free energy density of a ferroelectric crystal as a function of polarization P can be expressed with the Landau-Devonshire parametrization[29]

$$U_{LD}(P) = -\alpha P^2 + \beta P^4 + \gamma(P_x^2 P_y^2 + P_y^2 P_z^2 + P_x^2 P_z^2) \tag{4.1}$$

The parameters α, β, γ are related to material characteristics by

$$\alpha = \frac{2U_b}{P_s^2}, \beta = \frac{U_b}{P_s^4}, \gamma = \frac{4U_b}{P_s^4}\left(\frac{U_b}{U_b^*} - 1\right) \tag{4.2}$$

And in the case of $PbTiO_3$, U_b is the energy barrier height for the tetragonal to cubic phase (-72 meV), U_b^* is the energy barrier height for the orthorhombic to cubic phase (-54 meV), and P_s is the spontaneous polarization of the tetragonal phase (0.8 Cm^{-2}). Considering a uniaxial electric field E antiparallel to the spontaneous polarization, for a two-dimensional coordinate system (ξ_x, ξ_z), which represents an arbitrary transition structure[29], the position of stationary points that correspond to zero gradient of the enthalpy surface can be described with

$$\frac{\partial U_{LD}(P)}{\partial P_z} = E_z \tag{4.3}$$

$$\frac{\partial U_{LD}(P)}{\partial P_x} = E_x \tag{4.4}$$

The condition for the polarization rotation is that the polarization on the X-axis and Z-axis needs to be the same for both, tetragonal and orthorhombic structures as

$$P_x^{(T)} = P_x^{(O)}, P_z^{(T)} = P_z^{(O)} \tag{4.5}$$

and with the assumption that $E_x = 0$, (4.3) and (4.4) can describe the coercive field in terms of the model by

$$E_{c,rot} = 2\gamma\left(\frac{\alpha}{2\beta + \gamma}\right)^{3/2} = 8k(1 + 2K)^{-3/2}\frac{U_b}{P_s} \tag{4.6}$$

where $K = (\frac{U_b}{U_b^*} - 1)$ characterizes the degree of anisotropy of the free energy surface. The coercivity approaches the maximum limit at $\gamma = 4\beta$ or $K = 1$, as can be seen in the Fig. 4.2, which describes the coercive field as a function of K.

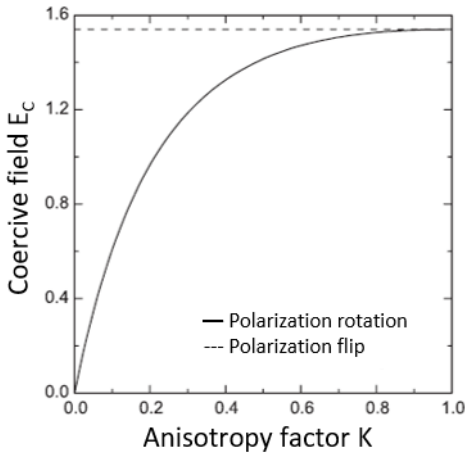

Fig. 4. 2. The coercive field as a function of the energy surface anisotropy for a uniaxial electric field[29]. $E_c = \frac{EP_s}{U_b}$.

At $K = 1$, the coercivity recovers the polarization flip through the cubic structure[29]

$$E_{c,fl} = (\frac{2}{3}\alpha)^{3/2}\beta^{-1/2} = \frac{8}{3^{3/2}}\frac{U_b}{P_s} \tag{4.7}$$

concluding that the condition $U_b/U_b^* < 2$ needs to be fulfilled for the polarization rotation remains energetically favourable for the ferroelectric switching.

The coercive field for an arbitrary direction electric field E can be obtained by solving (4.3) and (4.4) numerically[29] by using the polarization rotation condition

$$P_{x,z}^{(T)} = P_{x,z}^{(O)} \tag{4.8}$$

Where x, z is the direction of the electric field with respect to the polarization axis. Fig. 4.3 describes the ferroelectric hysteresis response at $K = 0.25$ for an E applied along the spontaneous polarization axis (0°) and an E directed 45° from the polarization axis. Both the coercive field and polarization are higher for the electric field along the polarization axis, and even when the coercive field was reduced for E at 45°, the polarization was reduced as well, and consequently, a lower mechanical response is produced.

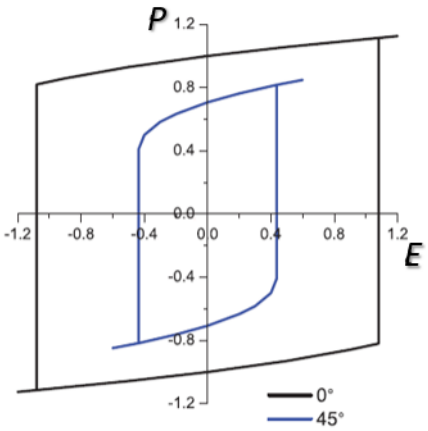

Fig. 4. 3. Ferroelectric hysteresis for arbitrary directions (0° and 45°) of the electric field[29].

To take advantage of the reduced coercivity and to maximize the mechanical response, the direction and magnitude of the field need to be controlled during the switching, which is the basis of the biaxial driving technique.

The **biaxial** driving technique is based on the polarization rotation achieved by dephasing two orthogonal sinusoidal electrical fields along the *x* (lateral) and *z* (propagation) axis of a piezoelectric actuator to reduce the coercivity produced by the ferroelectric switching resulting in an enhanced mechanical response[29], [30], [113], [114]. An experimental validation of the biaxial driving technique using PZT transducers was presented in[30] by comparing the acoustic efficiency of PZT transducers excited with a single electrical field vs. PZT transducers excited with two orthogonal electrical fields (biaxial driving technique). Results on[30] showed that the output acoustic power from a biaxial transducer depends on the phase difference of the applied electrical fields (Fig. 4.4), which is different at every transducer and needs to be characterized for all of them.

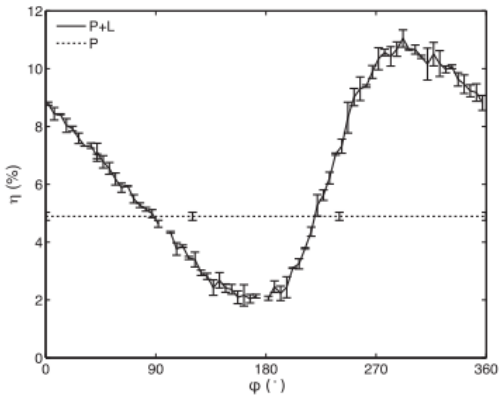

Fig. 4. 4. Plots of efficiency (η) as a function of the phase ϕ [30]. P+L and P indicate, respectively, when the biaxial mode and the single mode are used.

4.2 Finite Element Analysis (FEA)

The modelling of ultrasound transducers usually utilizes numerical methods such as the finite element method[115]. The finite element analysis (FEA) method, which was introduced by Turner *et al.* in 1956 for the analysis of aircraft structural problems[116], is a powerful computational technique to approximate solutions into a variety of real-world problems having complex domains subjected to general boundary conditions[117]. Over the years and due to the advances in high-speed computing, the finite element technique is considered one of the best methods for solving a wide variety of problems efficiently[118]. From a general perspective, the FEA is the representation of a domain into smaller subdomains called elements for which the approximate systematic solution is constructed as an exact solution that can not be solved by existing analytical formulations. These elements are considered to be interconnected by junction points called nodes, which are located on the element boundaries in the vicinity of different elements, as is shown in Fig. 4.5. The variation of the field variable (such as displacement, pressure and voltage) inside a finite element can be approximated by an interpolation function defined in terms of the field variables at the nodes[118], which are also called degrees-of-freedom (DOFs). By solving the field equations, the nodal values are obtained, and hence the interpolation function can define the field variable throughout the assembled elements. To reduce computational resources during the solution, typically, only the DOFs are calculated and stored, and the other variables that might be useful for further analysis can be obtained with postprocessing.

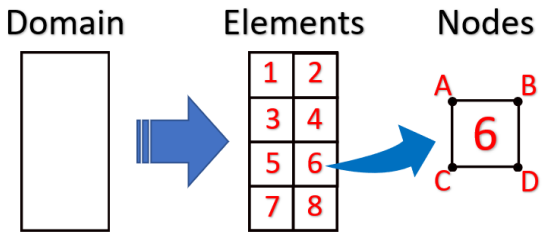

Fig. 4. 5. Decomposition of a two-dimensional domain into elements and the representation of the nodes forming it. Each independent element has a specific number and known nodes

The solution of a continuum problem with the finite element analysis requires the assembly of the element characteristic matrix and vectors that can be described by a global system of equations[117]

$$K_A U = F_A \tag{4.9}$$

where K_A is the assembly element characteristic matrix, U the nodal DOFs and F_A is the assembly of element vectors. The FEA method requires at least the next set of major steps to reach the solution of a continuum problem[37], [117], [118]:

- Discretize the structure into subdomains (elements). The type, size and arrangement of the element is described here.
- Select an interpolation method, which generally is in the form of a polynomial.
- Develop the individual element matrices and vectors $K_A^{(e)}$ and $F_A^{(e)}$, which are derived by using equilibrium conditions or variational principle.
- Assemble the element equations to obtain the global matrix of the entire domain. The individual characteristic element matrices need to be assembled into the global matrix by the summation

$$K_A = \sum_{e=1}^{E} K_A^{(e)} \tag{4.10}$$

  with *E* being the total number of elements. Similarly, the assembled form for the individual element vectors is obtained by the summation

$$F_A = \sum_{e=1}^{E} F_A^{(e)} \tag{4.11}$$

- Assign the proper boundary conditions, which correspond to the known state of specific nodes DOFs.
- Solve the global assembly equation (4.9).
- Post-processing. From the known nodal solution, several variables of interest can be calculated.

4.3 Finite element software

Few finite elements analysis packages are available that strongly coupled the piezoelectric material with the fluid medium[119]. Ansys (Ansys Inc., PA, USA) is a finite element method software developed in 1970 that can be applied to carry out a variety of coupled physics problems like piezoelectric and acoustic analysis that allow us to optimize ultrasound transducers designs for 2D, 3D or 2D-axisymmetric models. The standard procedure to perform a finite element analysis within the Ansys software consists of three typical steps:

- Model design. The design of the finite element model should include the building of the 2D, 3D or 2D-axisymmetric model and its subdivision into elements, the selection of the element type and the material properties.
- Model preparation. The selection of the analysis type should be set according to the nature of the problem (static, modal, harmonic, transient). The type of load needs to be specified (structural, thermal, electrical or fluid) and the boundary conditions.
- Solution and postprocessing. Acquisition of the DOFs of the problem and calculation of complementary field variables with its respective graphical representation.

These steps are similar in other FEA software packages, such as COMSOL Multyphysics (COMSOL, Inc., MA, USA) or PZFlex (OnScale, CA, USA).

4.3.1 Analysis types

The dynamic analyses are the most common analyses to perform into an acoustic and piezoelectric coupling problem when the acoustic pressure fields and electric responses are meant to be obtained. There are three commonly used dynamic analysis: the modal analysis, which is used to calculate the natural frequencies and vibration modes; the harmonic analysis, which describes the piezoelectric and acoustic response due to a sinusoidal excitation; and the transient analysis, which is based in the time-history response of the system due to a time-variating excitation[120]. For simplicity, matrix variables are represented with brackets [ ] while vectors with curly brackets { }.

4.3.1.1 Modal analysis

When structural vibrations are of concern with the absence of a time-dependent load, modal analysis is performed[117]. The goal of the modal analysis is to determine the mode shapes and natural frequencies of an acoustic or piezoelectric system or a combination of both. The equations of motion for an acoustic or structural system can be written as[120]–[122]

$$[M]\{\ddot{u}\} + [C]\{\dot{u}\} + [K]\{u\} = \{F\} \tag{4.12}$$

With $[M]$ is the mass matrix, $\{u\}$ is the nodal degree of freedom (pressure or displacement), $[C]$ is the damping matrix, $[K]$ the structure stiffness matrix and $\{F\}$ the load (force) vector. When damping is not considered, and no load is applied to the system, (4.12) can be reduced to

$$[M]\{\ddot{u}\} + [K]\{u\} = 0 \tag{4.13}$$

The free oscillations of the system will be harmonic of the form

$$\{u\} = \{\varphi\}_n \cos \omega_n t \tag{4.14}$$

Where $\{\varphi\}_n$ is the eigenvector representing the mode shape of the nth natural frequency, ω_n is the *nth* natural angular frequency (radians/s), and t is the time. Combining (4.14) with (4.13) and by considering only the solution where the determinant is equal to zero, the system solution to find the natural frequencies ω_n and vibration modes $\{\varphi\}_n$ is written in the form

$$|[K] - \omega_n^2[M]| = 0 \tag{4.15}$$

4.3.1.2 Harmonic analysis

When a system follows a cyclic loading, the resulting response is expected to be cyclic as well[117]. The harmonic response analysis is employed to determine the time-dependent equations of motion for steady-state vibrations systems. The goal of harmonic analysis is to calculate the structure response (nodal degrees-of-freedom) as a function of the frequency. Consider the general equation of motion

$$[M]\{\ddot{u_d}\} + [C]\{\dot{u_d}\} + [K]\{u_d\} = \{F\} \tag{4.16}$$

where $\{u_d\}$ represents the nodal displacement. All nodes within the structure are moving harmonically at the same frequency, but they do not have the same phase, therefore the displacement $\{u_d\}$ and the applied force $\{F\}$ vectors are defined as

$$\{u_d\} = \left\{u_{d_{max}} e^{ij}\right\} e^{j\omega t}\,, \tag{4.17}$$

$$\{F\} = \left\{F_{max} e^{ij}\right\} e^{j\omega t}\,, \tag{4.18}$$

with $u_{d_{max}}$ and F_{max} being the maximum displacement and force respectively, ϕ_u and ϕ_F the phase shift, ω the angular frequency and t the time. (4.17) and (4.18) can be rewritten as

$$\{u_d\} = \left\{u_{d_{max}}(\cos \phi_u + j \sin \phi_u)\right\} e^{j\omega t}\,, \tag{4.19}$$

$$\{u_d\} = \left\{u_{d_1} + j u_{d_2}\right\} e^{j\omega t}\,, \tag{4.20}$$

$$\{F\} = \{F_{max}(\cos \phi_F + j \sin \phi_F)\} e^{j\omega t}\,, \tag{4.21}$$

$$\{F\} = \{F_1 + i F_2\} e^{j\omega t}\,, \tag{4.22}$$

where the real part of the displacement and force vectors are represented by $u_{d_1} = u_{d_{max}} \cos \phi_u$ and $F_1 = F_{max} \cos \phi_F$ while the imaginary part is represented by $u_{d_2} = u_{d_{max}} \sin \phi_u$ and $F_2 = F_{max} \sin \phi_F$,

respectively. By substituting (4.16) and reducing it the system solution for the harmonic response analysis can be written as

$$([K]\omega^2[M] + i\omega[C])\left(\{u_{d_1}\} + i\{u_{d_2}\}\right) = \{F_1\} + j\{F_2\}\,. \tag{4.23}$$

4.3.1.3 Transient analysis

Transient analysis is performed when the response to non-cyclic transient load is required. The goal of a transient analysis is to determine the response of a system to any time-dependent load. The equation of motion that is solved by the transient analysis is[120], [122]

$$[M]\{\ddot{u_d}\} + [C]\{\dot{u_d}\} + [K]\{u_d\} = \{F(t)\}\,, \tag{4.24}$$

which contains the same terms as the harmonic analysis (4.16) with the difference that the applied load $\{F(t)\}$ now is time-dependent.

4.3.2 Acoustics module

The finite element analysis of acoustic systems involves the discretization of an acoustic region into elements and nodes which might be surrounded by a structural medium[120]. Tools such as Ansys and COMSOL supports FEA for acoustic problems, including its structural and thermal interaction, and have the capacity to solve them by using any of the three types analysis for a 2D, 3D or 2D-axisymmetric modelling. The degrees-of-freedom present in an acoustic analysis are commonly the pressure and displacement components. The solution of the acoustic analyses relies on the formulation of the acoustic wave equation for a compressible inviscid fluid of uniform mean density and pressure and no mean flow. The lossless acoustic wave equation was shown in section 3.8 with the (3.60)

$$\nabla^2 p - \frac{1}{c^2}\frac{\partial^2 p}{\partial t^2} = 0 \tag{3.60}$$

Where p is the acoustic pressure as a function of the three-dimensional system and the time t, and c is the speed of sound in the fluid medium which can be written as a function of compressibility of the medium β_0 and the fluid density ρ_o as $c = 1\Big/\sqrt{\rho_0\beta_0}$. To simplify future operations, the gradient and divergence operators can be written respectively as

$$\{L\} = \nabla() \tag{4.25A}$$

$$\{L\}^T = \nabla \cdot (\quad) = \left[\frac{\partial}{\partial x}\frac{\partial}{\partial y}\frac{\partial}{\partial z}\right] \tag{4.25B}$$

And then, (3.60) can be rewritten as

$$\{L\}^T(\{L\}p) - \frac{1}{c^2}\frac{\partial^2 p}{\partial t^2} = 0 \tag{4.26}$$

Element matrices can be obtained by discretizing (4.26) using a Galekin procedure[122]–[125], and by multiplying (4.26) for a virtual change of pressure and integrating over the volume of the domain

$$\int_{\mathrm{Vol}} \frac{1}{c^2}\delta p \frac{\partial^2 p}{\partial t^2} d(\mathrm{Vol}) + \int_{\mathrm{Vol}} (\{L\}^T \delta p)(\{L\}p) d(\mathrm{Vol}) = \int_s \{n\}^T \delta p(\{L\}p) d(s) \tag{4.27}$$

Where:

- $\mathrm{Vol} =$ volume of the acoustic domain.
- $\delta p =$ virtual change in pressure.
- $s =$ surface where the derivative of pressure normal to the surface is applied. For a fluid-structure interaction, s represents the interface.
- $\{n\} =$ unit normal to s.

The relationship between the normal pressure gradient of the fluid and the normal acceleration at the interface s (fluid-structure) can be written in matrix notation as

$$\{n\}^T(\{L\}p) = -\rho_o\{n\}^T\left(\frac{\partial^2}{\partial t^2}\{u_d\}\right) \tag{4.28}$$

for $\{u_d\}$ representing the nodal displacement vector. By substituting (4.28) into (4.27) results into

$$\int_{\mathrm{Vol}} \frac{1}{c^2}\delta p \frac{\partial^2 p}{\partial t^2} d(\mathrm{Vol}) + \int_{\mathrm{Vol}} (\{L\}^T \delta p)(\{L\}p) d(\mathrm{Vol}) = -\int_s \rho_o \delta p\{n\}^T\left(\frac{\partial^2}{\partial t^2}\{u_d\}\right) d(s)\,, \tag{4.29}$$

which contains the pressure and displacement components as the variables to solve.

The fluid pressure p, the displacement components $\{u_d\}$ and the virtual change in nodal pressure δp can be represented by their finite element approximating shape function

$$p = \{N\}^T\{p_e\} \tag{4.30}$$

$$u_d = \{\acute{N}\}^T\{u_{d_e}\} \tag{4.31}$$

$$\delta p = \{N\}^T\{\delta p_e\} \tag{4.32}$$

The element shape function for the pressure and displacements are represented by $\{N\}$ and $\{\acute{N}\}$, respectively. If the matrix operator $\{L\}$ is applied to the shape functions $\{N\}$ as

$$[B] = \{L\}\{N\}^T, \tag{4.33}$$

and factoring out δp_e (different than zero), (4.29) becomes

$$\frac{1}{c^2}\int_{\text{Vol}}\{N\}\{N\}^T d(\text{Vol})\{\ddot{p_e}\} + \int_{\text{Vol}}[B]^T[B]d(\text{Vol})\{p_e\} + \rho_o\int_s \{N\}\{n\}^T\{\acute{N}\}^T d(s)\{\ddot{u_{d_e}}\} = \{0\} \tag{4.34}$$

If (4.34) is written in the matrix notation, the discretized wave equation is obtained

$$[M_f]\{\ddot{p_e}\} + [K_f]\{p_e\} + \rho_o[R]^T\{\ddot{u_{d_e}}\} = 0, \tag{4.35}$$

where:

- $[M_f] = \frac{1}{c^2}\int_{\text{Vol}}\{N\}\{N\}^T d(\text{Vol})$ represents the fluid mass matrix,
- $[K_f] = \int_{\text{Vol}}[B]^T[B]d(\text{Vol})$ represents the fluid stiffness matrix,
- and $\rho_o[R]^T = \rho_o\int_s \{N\}\{n\}^T\{\acute{N}\}^T d(s)$ is the coupling mass matrix for a fluid-structure interaction.

If there is any dissipation of energy due to damping that should be considered, then (4.35) becomes

$$[M_f]\{\ddot{p_e}\} + [C_F]\{\dot{p_e}\} + [K_f]\{p_e\} + \rho_o[R]^T\{\ddot{u_{d_e}}\} = 0, \tag{4.36}$$

where $[C_F] = \frac{\beta}{c}\int_s \{N\}\{N\}^T d(s)$ is the fluid damping matrix, $\beta = \frac{r_{ab}}{\rho_o c}$ is the boundary absorption coefficient and r_{ab} is the absorption at the boundary.

4.3.3 Piezoelectric modeling

The piezoelectric material vibration is described within the finite element analysis as the coupling between the structural and electrostatic physics[126]. When a voltage is applied to the piezoelectric material, it will vibrate producing a displacement vector $\{u_d\}$. In linear piezoelectric theory[35] the charge equations are coupled with the elasticity equations by using piezoelectric constants (section 3.3.1). FEA

tools support the coupling physics analysis that represents the piezoelectricity for the three dynamic analyses shown in section 4.2.1 for the 2D, 3D and 2D-axisymmetric modelling, as well as the fluid-solid interaction. The degrees-of-freedom involved in a piezoelectric analysis is the displacement components and voltage. One of the main advantages of the FEA applied to calculate the piezoelectric response is that it considers each of the elements forming the piezoelectric material with its own orientation of lattice axes producing an interaction similar to a domain-domain interaction as the one present in piezoelectric ceramics[127]. The constitutive equations representing a piezoelectric material given in section 3.3.1 (3.22 and 3.24) can be simplified as

$$\{T\} = [c^E]\{\xi\} - [e]\{E\}, \tag{4.37}$$

$$\{D\} = [e]^T\{\xi\} + \left[\varepsilon^\xi\right]\{E\}, \tag{4.38}$$

which can also be rewritten into a matrix notation

$$\begin{Bmatrix}\{T\}\\ \{D\}\end{Bmatrix} = \begin{bmatrix}[c^E] & [e]\\ [e]^T & -\left[\varepsilon^\xi\right]\end{bmatrix}\begin{Bmatrix}\{\xi\}\\ -\{E\}\end{Bmatrix}, \tag{4.39}$$

where:

- $\{T\}$ is the stress vector,
- $\{D\}$ is the electric displacement vector,
- $[c^E]$ represents the elasticity matrix for a constant electric field,
- $[e]$ is the piezoelectric stress constant ($^C/_{m^2}$),
- $\left[\varepsilon^\xi\right]$ is the dielectric matrix obtained at constant strain,
- $\{\xi\}$ represents the elastic strain vector,
- and $\{E\}$ represents the electric field intensity vector.

After the application of the variational principle and finite element discretization[128] to (4.39), the couple finite element matrix equation derived for a one-element model is[122]:

$$\begin{bmatrix}[M] & 0\\ 0 & 0\end{bmatrix}\begin{Bmatrix}\{\ddot{u_d}\}\\ \{\ddot{V}\}\end{Bmatrix} + \begin{bmatrix}[C] & 0\\ 0 & -[C^{vh}]\end{bmatrix}\begin{Bmatrix}\{\dot{u_d}\}\\ \{\dot{V}\}\end{Bmatrix} + \begin{bmatrix}[K] & [K^z]\\ [K^z]^T & -[K^d]\end{bmatrix}\begin{Bmatrix}u_d\\ V\end{Bmatrix} = \begin{Bmatrix}\{F\}\\ \{J\} + \{J^{th}\}\end{Bmatrix} \tag{4.40}$$

Where$[M]$ is the element mass matrix, $\{u_d\}$ represents the displacement components, $\{V\}$ represent the applied voltage, $[C]$ is the element structural damping matrix, $[C^{vh}]$ represent the element electric damping matrix, $[K]$ is the element stiffness matrix, $[K^d]$ is the element dielectric permittivity coefficient

matrix, $[K^z] = \int_V [B]^T[e][B]d(V)$ is the piezoelectric coupling matrix, $[B]$ is the strain-displacement matrix, $\{F\}$ represents the vector of nodal or surface applied loads, $\{J\}$ represent the vector of nodal, body or surface charges and, $\{J^{th}\}$ is the element thermo-piezoelectric load vector.

4.3.4 Fluid-structure interaction

The fluid-structure interaction describes the response of the acoustic pressure to structural vibration, and so the converse effect when the acoustic pressure acts on a structure which causes it to vibrate. In a fluid-structure problem, both the acoustic wave equation and the general equation of motion need to be coupled to each other[122], [129]. A fluid pressure load $\{F_F\}$ needs to be consider in the general equation of motion described in 3.2.1.2 (4.16)

$$[M]\{\ddot{u_d}\} + [C]\{\dot{u_d}\} + [K]\{u_d\} = \{F\} + \{F_F\}. \tag{4.41}$$

The fluid pressure vector $\{F_F\}$ at the interface, *s* can be written as

$$\{F_F\} = [R]\{p_e\}, \tag{4.42}$$

for $[R] = \int_s [N]\acute{\{N\}}^T\{n\}d(s)$ and $\{p_e\}$ is the nodal pressure vector. By substituting (4.42) into (4.41)

$$[M]\{\ddot{u_d}\} + [C]\{\dot{u_d}\} + [K]\{u_d\} - [R]\{p_e\} = \{F\} \tag{4.43}$$

(4.36) and (4.43) are assembled to describe the finite element equation for the fluid-structure interaction problem

$$\begin{bmatrix} [M] & [0] \\ [M^{fs}] & [M_f] \end{bmatrix} \begin{Bmatrix} \{\ddot{u_d}\} \\ \{\ddot{p_e}\} \end{Bmatrix} + \begin{bmatrix} [C] & [0] \\ [0] & [C_f] \end{bmatrix} \begin{Bmatrix} \{\dot{u_d}\} \\ \{\dot{p_e}\} \end{Bmatrix} + \begin{bmatrix} [K] & [K^{fs}] \\ [0] & [K_f] \end{bmatrix} \begin{Bmatrix} \{u_d\} \\ \{p_e\} \end{Bmatrix} = \begin{Bmatrix} \{F\} \\ \{0\} \end{Bmatrix} \tag{4.44}$$

With $[K^{fs}] = -[R]$ and $[M^{fs}] = \rho_o[R]^T$

4.3.5 Material parameters

To model a piezoelectric material within an FEA software is required to set the right material parameters correctly. The parameters needed to define before starting the analysis are: The elastic stiffness (c) or compliance (S) matrix, the piezoelectric constant $e(Cm^{-2})$ or $d(Nm^{-1})$, the dielectric matrix ε and density ρ of the material. Because most of the material parameters follow the format suggested by the IEEE standard of piezoelectricity[35] following the polarization axis along the Z-direction, for the case of ANSYS FEA software several arrangements need to be done to the property matrices due the fact that the ANSYS format for a property matrix follows the polarization axis along the Y-direction[130]. The restructuration from IEEE format to ANSYS format of the matrix for the piezoelectric constants e and d are shown within Appendix B.

Chapter 5: SINGLE ELEMENT BIAXIAL TRANSDUCER

Within this chapter, a finite element formulation is presented to establish the theoretical model that describes the biaxial technique to drive transducers. The primary objective in the present research work is to characterize and optimize the parameters that produce a contribution to the efficiency response and the acoustic beam steering of ferroelectric transducers while being driven by the biaxial driving technique. This chapter presents FEA models and experimental validation on different ferroelectric materials and shapes that are meant to demonstrate their response under biaxial driving as a function of the applied effective power, phase and driving frequency. Experimental validation is presented for the different simulated shapes using PZT as ferroelectric material. The first part of this chapter describes the FEA model used to simulate a prismatic shaped ultrasound transducer by testing different ferroelectric materials; the second part corresponds to the experimental validation of PZT ultrasound prismatic transducers. The third part is dedicated to the simulation and experimental validation of PZT ring-shaped ultrasound transducers.

5.1 3D FEA simulation: Single element prismatic shape transducer for different ferroelectric materials

A 3D-FEA model was defined using the software Ansys Workbench to describe the conventional and biaxial response of single-element prismatic shaped transducers made of different ferroelectric materials. For conventional transducers, an electric field is applied in the thickness mode direction. For biaxial transducers, two independent electric fields are applied: one in the thickness mode and one in the lateral mode. Three different ferroelectric materials were tested in the simulations, two from the same crystallographic point group p4mm: Lead Zirconate Titanate (PZT, DL-47, Del Piezo Specialities, LLC, West Palm Beach, FL, USA) and Barium Titanate ($\mathrm{BaTiO_3}$, DL-21, Del Piezo Specialities, LLC, West Palm Beach, FL, USA); and one from the point group p3m: Lithium Niobate ($\mathrm{LiNbO_3}$, Boston Piezo Optics Inc., Bellingham, MA, USA)[35], [57]. The three materials share the ABO_3 perovskite structure[57], [131]. The purpose of simulating different materials was to compare how different crystal structures respond to the biaxial driving conditions and to demonstrate that the biaxial response is not inherent to a specific material.

Harmonic analysis was performed with enough frequency range to cover the first vibration modes of each material. The rectangular piezoceramic block (7 mm x 6.9 mm x 10.6 mm) was poled along the propagation axis (Z), and it was enclosed in a 20 mm x 20 mm x 20 mm acrylonitrile-butadiene-styrene (ABS) plastic cube, with air as backing material. A 0.6 mm thick silicone layer was placed on the lateral electrodes on

the region covering the piezoceramic and the ABS case. A water cylinder with a radius of 15.5 mm and a height 37.5 mm was used in simulations as the propagation medium. The mesh model had a size of 1.5 mm. The propagation (*P*, front and back faces) and lateral (*L*, right and left faces) electrodes were modelled as coupled equipotential sets of nodes. For this initial set of simulations, no damping was considered in the simulation. Damping was later added when comparing with experimental devices (section 5.2). An acoustic absorption boundary condition was applied on the outer walls of the water medium to avoid reflected waves[119], [121], [126], [132]. Fig. 5.1 shows the complete 3D model used for the simulation. The material properties for piezoelectric, acoustic and structural domains are shown in Appendix A.

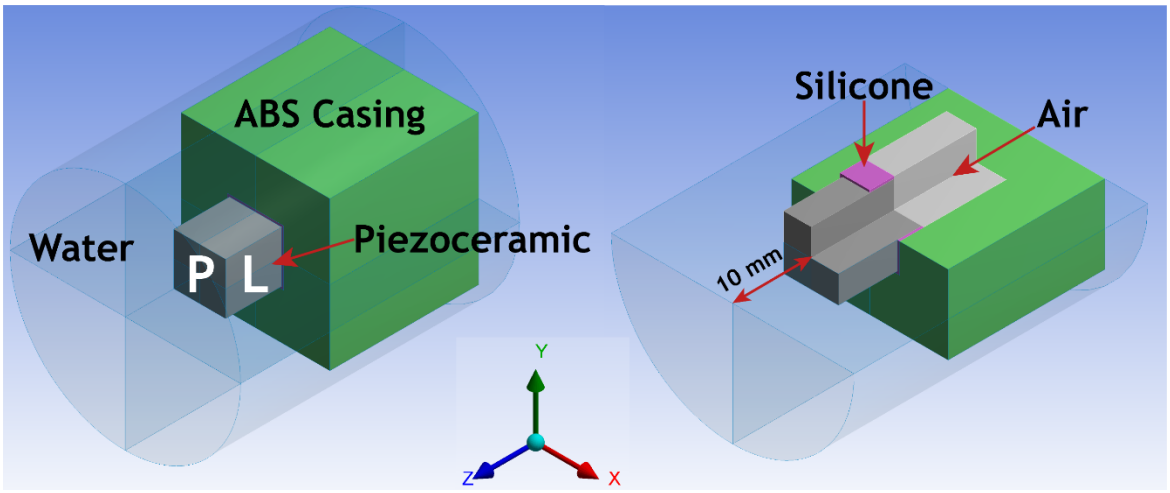

Fig. 5. 1. FEA 3D model of a biaxial transducer poled along the propagation direction (Z-Axis). Conventional excitation of the transducer was carried out by applying an electric field to the propagation faces *P* (Z-Axis). Biaxial excitation was accomplished by applying an additional orthogonal electric field to the lateral faces L (X-Axis).

For the structural part of the model, the couple-field element solid226 is used to model the piezoelectric effect for the ferroelectric material. Solid226 is a 3D element with 20 nodes that can withstand different shapes (brick, tetrahedral, prism and pyramid) and can have up to six degrees of freedom (x, y and z displacement, voltage, temperature and concentration). However, to model the piezoelectric effect, only the displacement and voltage DOFs are required. The ABS case and the silicone are all meshed with the solid187 element, which is a 10-node element with the nodal displacement in x, y and z as its DOFs.

The acoustic bodies of the model correspond to the water and air medium, which were modelled with a combination of elements fluid220 and fluid221, and 20 and 10 nodes elements, respectively. This choice of models was made to improve the meshing accuracy of the structure. Fluid220 and fluid221 can have up to 4 degrees-of-freedom (x, y and z displacement and pressure) and they were all used within the fluid-

structure interface; otherwise, only pressure DOF was active to reduce simulation time. Fluid220 is a hexahedral shaped element while fluid221 posses a tetrahedral shape.

A radiation boundary condition was applied to the exterior faces of the water cylinder to absorb the outgoing acoustic waves. The radiation boundary condition on the impedance boundary can be expressed as the acoustic pressure gradient at the normal to an absorbing boundary as[120]

$$\frac{\partial p(r)}{\partial n} + j\omega\rho_o Y_o p(r) = 0, \tag{5.1}$$

where $Y_o = \frac{1}{Z_o} = \frac{1}{(\rho_o c_o)}$ is the fluid admittance. This expression produces the absorption of all the acoustic waves ongoing normal to the absorbing interface. However, acoustic waves that are not normal to the absorbing interface would produce some reflection.

The excitation applied to the active electrode face corresponds to a time-harmonic potential difference[122]

$$V(r,t) = V_{(r)} \cos\left(\omega t + \phi_{(r)}\right), \tag{5.2}$$

or

$$V(r,t) = V_{(r)\text{Real}} \cos(\omega t) - V_{(r)\text{Imag}} \sin(\omega t) \tag{5.3}$$

Where r is the location vector, t is the time, ω the angular frequency and, $V_{(r)}$ and $\phi_{(r)}$ are the magnitude of the amplitude and phase angle which are related by

$$V_{(r)} = \sqrt{V_{(r)\text{Real}}^2 + V_{(r)\text{Imag}}^2}, \tag{5.4}$$

$$V_{(r)\text{Real}} = V_{(r)} \sin(\phi_{(r)}), \tag{5.5}$$

and

$$V_{(r)\text{Imag}} = V_{(r)} \cos(\phi_{(r)}). \tag{5.6}$$

The real and imaginary part of the applied harmonic potential difference is used to calculate the electric impedance at the respective electrode with the equation

$$Z = \frac{V_{(r)\text{Real}} + jV_{(r)\text{Imag}}}{2\pi f Q j}, \tag{5.7}$$

where Z is the complex impedance, Q is the complex charge obtained as a reaction force on the propagation (front face) or lateral (right face) electrode, $V_{(r)\mathrm{Real}}$ and $V_{(r)\mathrm{Imag}}$ represents the complex amplitude of the time-harmonic voltage applied and f the tested frequency. The complex impedance is used within the FEA model to determine the respective active electrode (Propagation and/or lateral) applied effective power W_E at a specific frequency with the relation

$$W_E = \frac{V_{RMS}^2}{|Z|^2}|Z|\cos\phi\,. \tag{5.8}$$

Knowing that $\cos\phi = \frac{R\{Z\}}{|Z|}$, (5.8) is reduced to

$$W_E = \frac{V_{RMS}^2}{|Z|^2}R\{Z\}\,. \tag{5.9}$$

The acoustic pressure was obtained from the FEA model solution nodes of the water region covering 10 mm from the transducer and the top face of the water on the XZ-Plane. The acoustic pressure on the water cylinder face at 10 mm from the piezoceramic on the XY-Plane was obtained to calculate the time-averaged acoustic power W_A delivered[122]

$$W_A = \frac{1}{2\rho c}\int_s P_A^2(r)ds\,, \tag{5.10}$$

where ρ is the density of the water, c is the speed of sound in water and $P_A(r)$ is the acoustic pressure at the nodes of the surface s.

5.1.1 Conventional driving

A single electric field was applied to the propagation electrodes (P-electrodes) to represent the conventional transducer driving in the FEA model, while the L-electrode remained coupled (no voltage applied, high impedance). The applied sinusoidal signal had a power of 2 W at the propagation resonance frequency f_r of each material, and this power was kept constant across the harmonic analysis. The electric impedance, the applied electric power (W_E) on the P-electrodes, the acoustic power (W_A) on the face of the water cylinder 10 mm away from the transducer face, the acoustic pressure on the XZ-plane, and the acoustic efficiency (η) were calculated. Acoustic efficiency was calculated with[133]

$$\eta = \frac{W_A}{W_E} \times 100\%. \tag{5.11}$$

5.1.2 Biaxial driving

Two orthogonal electric fields connected to independent unbalanced sinusoidal signals were applied to the P-electrodes and lateral electrodes (L-electrodes) to model the biaxial driving of the single element transducers. A series of FEA simulations were executed to study the acoustic efficiency and beam profile as a function of the **phase ϕ between the driving signals** and **power p_l** applied to the L-electrodes. Power at the P-electrodes was kept constant for all simulations and at 1 W at the f_r. The phase ϕ was varied from 0° to 315° with a 45° step for $p_l = 0.1$, 0.5 and 1 W. A harmonic analysis was performed where the electric impedance at both electrodes, the sum of the effective electric power at both electrodes (W_E), the acoustic power (W_A) on the water cylinder 10 mm away from the face of the transducer, and the acoustic pressure on the XZ-plane were calculated at every value of ϕ and p_l tested. The acoustic efficiency (η) as a function of ϕ and p_l was calculated with [30], [36]

$$\eta(\phi, p_l) = \frac{W_A(\phi,p_l)}{W_E(\phi,p_l)} \times 100\%. \tag{5.12}$$

5.1.3 Steering calculation

The degree of the ultrasound beam steering was calculated by analyzing the acoustic beam profiles generated by the transducer with biaxial and conventional drivings. Firstly, the centroid (Ψ) was calculated in the XZ-plane within –3 dB of the normalized acoustic pressure distribution for conventional (Ψ_C) and biaxial (Ψ_B) driving conditions, as shown in Fig. 5.2. The steering angle γ was defined as the angle between the vectors formed by Ψ_C and Ψ_B at all the tested combinations of ϕ and p_l at the propagation f_r. A 2 mm-offset was applied in the calculations of the acoustic field centroids Ψ_C and Ψ_B to match experimental acoustic pressure measurements, as is not possible to experimentally measure the acoustic field on the surface of the transducer.

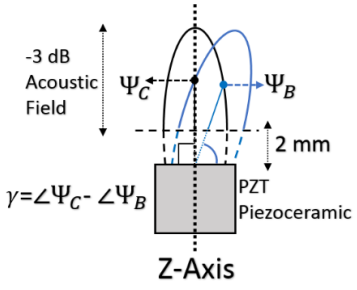

*Fig. 5. 2. Calculation of γ between the vectors formed by Ψ_C and Ψ_B within a –3 dB normalized acoustic pressure field at different ϕ and p_l values.*A 2 mm compensation was applied on the Z-axis to match experimental measurement conditions.

5.1.4 Impedance FEA results

Predictions of the f_r and impedance at the P- and L-electrodes for PZT, $BaTiO_3$ and $LiNbO_3$ are summarized in Table 5.1. It is worth noting that for the specific case of the $LiNbO_3$, the resonance frequency on the propagation mode is significantly affected by the addition of the L-electrodes even without a signal applied on them, and this can be clearly distinguished on an electric charge vs. frequency plot. Fig. 5.3 shows the simulated impedance response for the three ferroelectric materials.

Table 5. 1 PZT, $BaTiO_3$ and $LiNbO_3$ resonance frequencies.

Material	Frequency range (kHz)	f_r Propagation (kHz)	f_r Lateral (kHz)	Driving frequency (kHz)
PZT	100 – 150	130	145	130
$BaTiO_3$	150 – 250	201	209	201
$LiNbO_3$	250 – 350	288	270	288

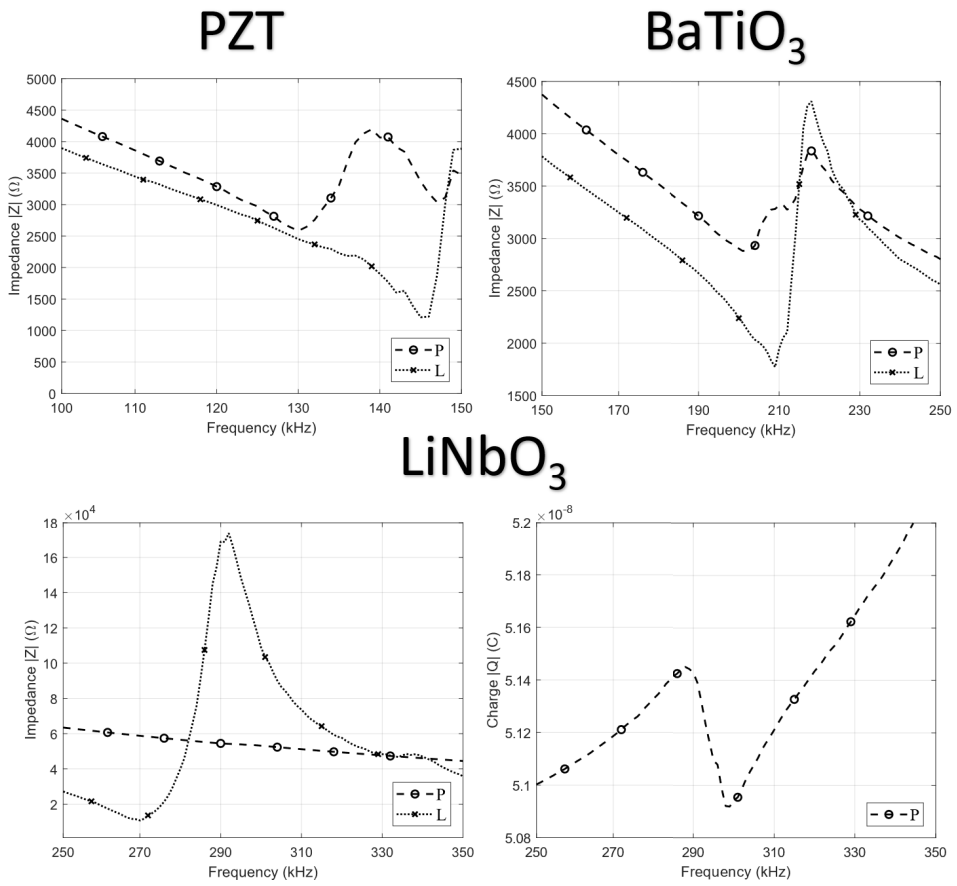

Fig. 5. 3. Comparison of impedance at the P- L −electrodes of the FEA transducer model for the three different ferroelectric materials. For the $LiNbO_3$ case, the charge vs frequency plot is also shown.

5.1.5 FEA predictions for the acoustic pressure fields: Steering analysis

Fig. 5.4 shows the normalized acoustic pressure field for $LiNbO_3$, $BaTiO_3$ and PZT ferroelectric materials along the XZ-Plane on a logarithmic scale. When using conventional driving, FEA predicted an ultrasound beam directed at an angle of 0° relative to the Z-axis, which is expected in ideal conditions. The largest steering angles (γ) for $LiNbO_3$ were predicted with a lateral power $p_l = 1$ W (top row in Fig. 5.4), with $\gamma = -30.7°$ at $\phi = 270°$, and $\gamma = 29°$ at $\phi = 90°$. The largest value of γ for $BaTiO_3$ was observed with $p_l = 1$ W (mid row in Fig. 5.4), with $\gamma = -27.7°$ at $\phi = 90°$ and $\gamma = 29.6°$ at $\phi = 270°$. The largest value of γ for PZT were observed with $p_l = 1$ W (bottom row in Fig. 5.4), with $\gamma = 40.8°$ at $\phi = 315°$ and $\gamma = -25.3°$ at $\phi = 90°$. The acoustic field for three materials was calculated at their respective propagation frequency f_r (Table 5.1). The FEA acoustic profile exhibited a nonsymmetric response between the achieved steering in the positive (right) and negative (left) directions for the three ferroelectric materials.

The results for γ in function of ϕ and p_l are shown in Fig. 5.5. Predictions showed a sinusoidal-type response between γ and ϕ, and the limit values of γ were proportional to p_l. Table 5.2 shows a summary of the findings.

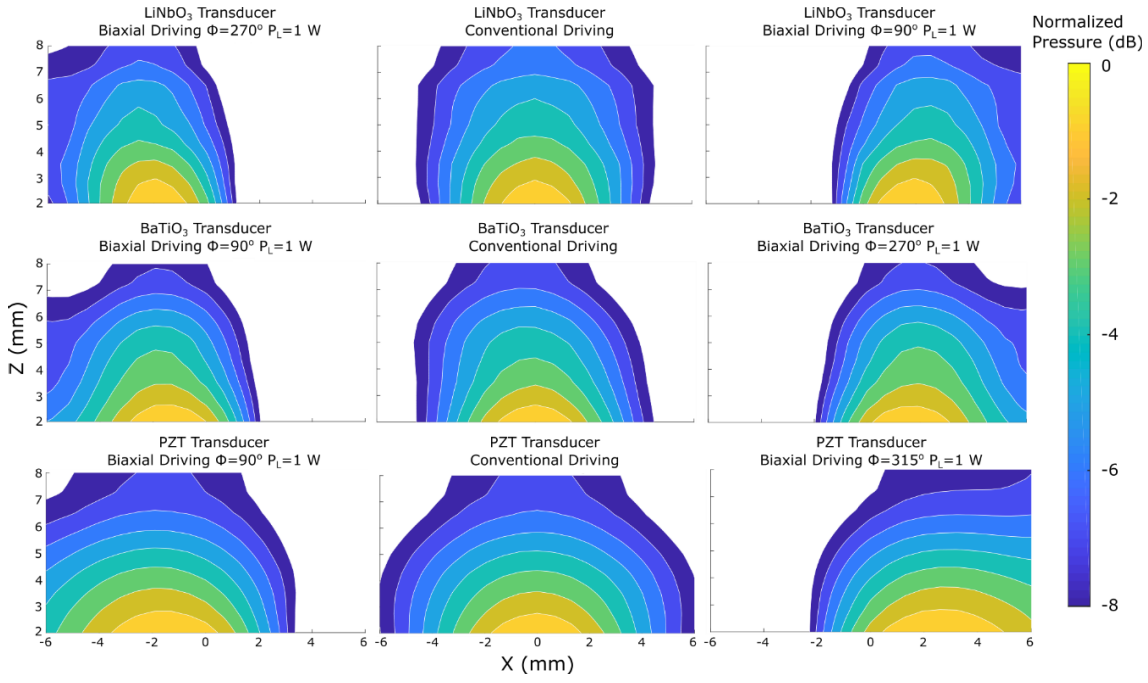

Fig. 5. 4. Predictions of the normalized acoustic pressure fields with a contours cutout at −8 dB produced by the $LiNbO_3$ (top), $BaTiO_3$ (middle) and PZT (bottom) biaxial transducers while applying 1 W on both P- and L-electrodes. Beam profiles of the maximum positive (right) and negative (left) steering are shown, along with the profile observed with the conventional driving (center).

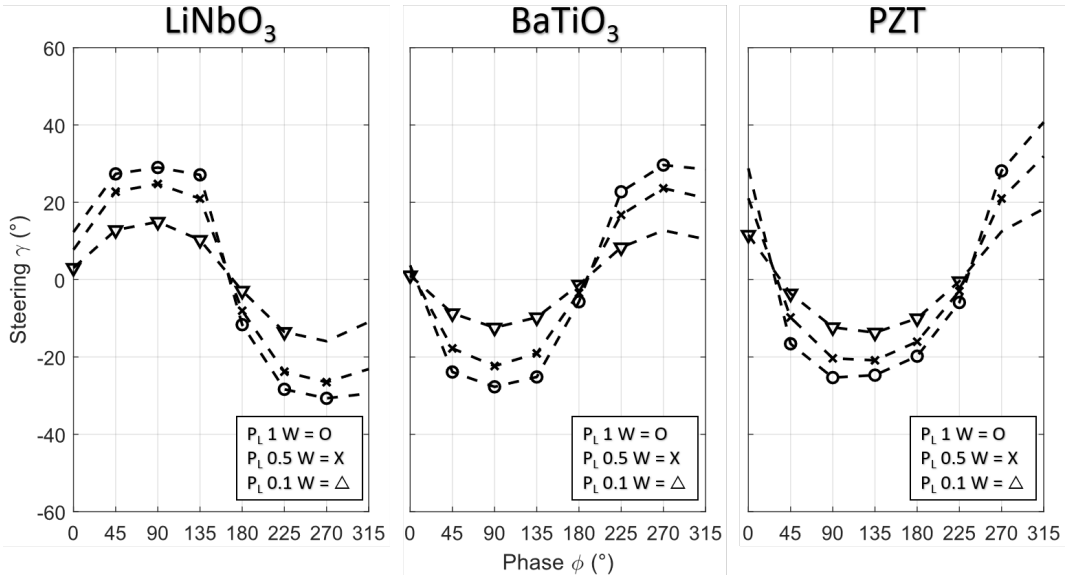

Fig. 5. 5. Predictions of the steering (γ) as a function of phase difference (ϕ) between the P- and L- electrodes for the $LiNbO_3$, $BaTiO_3$ and PZT transducers model at different applied power levels on the L-electrode.

Table 5. 2 Maximal steering predicted by the FEA model for different ferroelectric materials

$LiNbO_3$					
p_l **(W)**	**Negative steering (left)**		**Positive steering (right)**		**Peak-peak steering**
	ϕ (°)	γ (°)	ϕ (°)	γ (°)	(°)
0.1	270	-15.9	90	15	30.9
0.5	270	-26.5	90	24.8	51.3
1.0	270	-30.7	90	29	59.7
$BaTiO_3$					
p_l **(W)**	**Negative steering (left)**		**Positive steering (right)**		**Peak-peak steering**
	ϕ (°)	γ (°)	ϕ (°)	γ (°)	(°)
0.1	90	-12.4	270	12.7	25.1
0.5	90	-22.3	270	23.6	45.9
1.0	90	-27.7	270	29.6	57.3
PZT					
p_l **(W)**	**Negative steering (left)**		**Positive steering (right)**		**Peak-peak steering**
	ϕ (°)	γ (°)	ϕ (°)	γ (°)	(°)
0.1	135	–13.7	315	18.3	32
0.5	90	–20.4	315	31.9	52.3
1.0	90	–25.3	315	40.8	66.1

5.1.6 Efficiency (η) as a function of phase and power

Fig. 5.6 illustrates the simulated relationship between η and ϕ for different power levels applied to the L-electrodes. For the three tested materials, a sinusoidal relationship between η and ϕ was observed. The values of η were inversely proportional to p_l. For all materials, the biaxial driving simulations showed a maximal value of η (η_{max}) when applying $p_l = 0.1$ W. Baseline values (only-P) of η were calculated with the conventional driving. For PZT, η_{max} was 41.4% at $\phi = 90°$, with a baseline η of 43.4%. For $\mathrm{LiNbO_3}$ η_{max} was 69.3% at $\phi = 90°$, with a baseline η of 72.2%. Finally, for $\mathrm{BaTiO_3}$ η_{max} was 54% at $\phi = 45°$, with a baseline η of 54.8%.

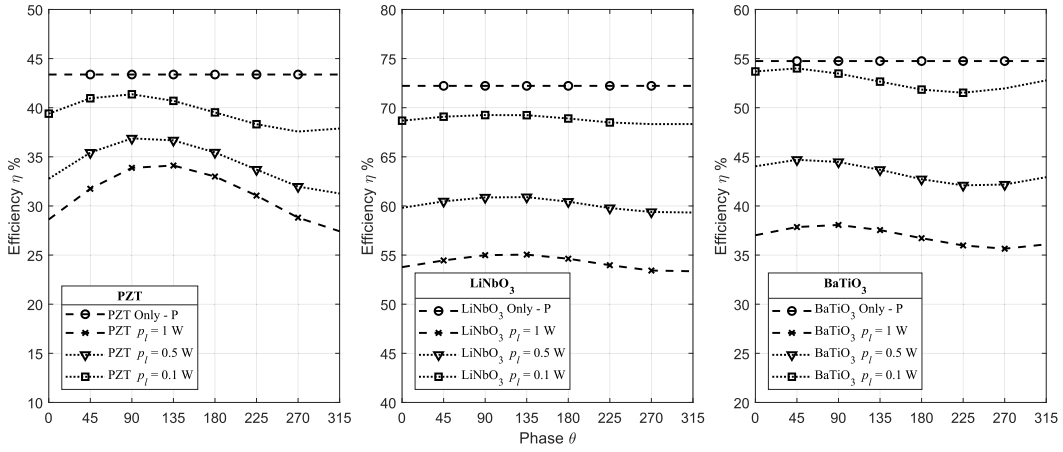

Fig. 5. 6. η vs. ϕ FEA predictions for the PZT (left), LiNbO₃ (center) and BaTiO₃ (right) biaxial transducers at different values of p_l.

5.1.7 Analysis of FEA predictions for biaxial driving for different ferroelectric materials

The finite element simulations described in section 5.1 presented for the first time that single element ultrasound transducers made of other ferroelectric materials can control the direction of the transmitted ultrasound beam up to 40.8° when using the biaxial driving. Highly relevant, we identified how this steering depends on the dephasing of the signals applied to the P- and L-electrodes, and the power applied on the L-electrodes.

The driving frequency (propagation f_r) for each material in the FEA model was different due to their different properties (Appendix A). The lowest f_r corresponds to the PZT material with a frequency of 130 kHz followed by the $\mathrm{BaTiO_3}$ with 201 kHz and the highest frequency is the $\mathrm{LiNbO_3}$ with 288 kHz. The value of the impedance at propagation f_r for PZT and $\mathrm{BaTiO_3}$ was really close to each other, with values of 2582 Ω and 2881 Ω, respectively. $\mathrm{LiNbO_3}$ showed a high impedance at its propagation f_r with a value of 54.8 kΩ, resulting in a limitation when compared to the other two materials, as higher voltages are required to reach the same power, regardless of its efficiency. Also, within the FEA simulations, the first

resonance peak for the $LiNbO_3$ material can not easily be identified while plotting the impedance vs. frequency response as the differences in the charge (Fig. 5.3, left-bottom) are small and compensated by the 1 kHz resolution step in frequency. This small change in the charge within the $LiNbO_3$ material can be attributed to the charge contributions made by the additional set of electrodes due to its material property e_{22} being different from 0. This condition implies that there are contributions to the charge surface density on the X-axis produced by a deformation in the same axis. In addition, the biaxial transducer can be seen as a 2-port device implying that the impedance seen at one port is dependant to the excitation of the second port, which might generate a big contribution to the impedance response depending on the material properties.

The three different ferroelectric materials exhibited a sinusoidal response of γ with respect to ϕ with the maximum peak-peak steering reached by the PZT material with a value of ϕ = 66.1° followed by the $LiNbO_3$ with ϕ = 59.7° , and then $BaTiO_3$ with ϕ = 57.3°. The PZT material showed its maximum positive and negative steering response at a ϕ of 90° and 270°, respectively. For both $BaTiO_3$ and $LiNbO_3$, these maximum positive and negative steering were observed at a ϕ of 90° and 270°, respectively. However, the $LiNbO_3$ material showed an inverse response in phase for the maximum positive and negative steering when compared with $BaTiO_3$. This inverse response can be related to the fact that the lateral resonance frequency is lower than its propagation resonance frequency, as shown in Fig. 5.3. The inversion of the maximum steering phases can be changed by changing the direction of the applied electric field on the lateral electrodes. The maximum steering was always reached for a $P_l = 1$ W and gradually reduced while decreasing P_l values.

The biaxial efficiency followed a sinusoidal response as described for Pichardo *et al*[30], and it increased as P_l was reduced. The maximum biaxial efficiency values were reached for $LiNbO_3$ with a η value of 69.3% at $\phi = 90°$, however, for the described total power applied of 2 W within this lossless simulation, conventional driving got higher efficiencies than biaxial, suggesting that a higher total power or lower P_l values should be tested in order to get a high biaxial efficiency. Additionally, it was observed that there is a trade-off between the maximum steering and efficiency values as they do not share the same ϕ and P_l, which is an important behaviour to consider when implementing biaxial driving.

5.2 Experimental validation: PZT

Due to the fact that the characterization of the simulated PZT transducer produced the highest possible peak-peak steering value, and that PZT is the most widely used material in medical applications, it was decided to validate those results experimentally. Three biaxial transducers were fabricated with the same

mechanical design used in FEA simulations (identified as B_i, where i is the transducer number) and three conventional transducers (identified as C_i) using the same piezoceramic material and dimensions. Both the biaxial and conventional transducers were poled along the propagation axis, as described in Fig. 5.1. In the case of conventional transducers, silver electrodes were only present on the faces of the propagation axis. On the biaxial transducers, silver electrodes were present on both the propagation axis faces and the lateral axis faces. We applied a drop of silver epoxy (8331S-15G, MG Chemicals, B.C., Canada) to strengthen the solder joint of each electrode. Based on our previous work[30], [36], we used silicone (Silicone I*, Momentive Performance Materials Inc., NC, USA) to hold the 3D-printed ABS casing (Taz 5, Lulzbot, CO, USA) to the piezoceramic and to waterproof the inside of the transducer. Air was used as the backing material. The single element biaxial and conventional transducers are shown in Fig. 5.7. The electric impedance characterization to determine the f_r of each transducer was performed by using a vector network analyzer (ZNL3, Rode & Schwarz, Munich, Germany) and is shown in Fig. 5.8. The transducer impedance was matched to 50 Ω at the resonance frequency. In the case of biaxial transducers, the propagation and the lateral modes were matched separately.

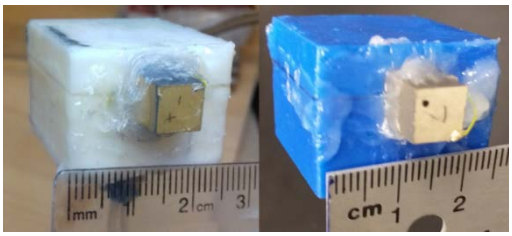

Fig. 5. 7. Single element biaxial transducer (white case). Front-back faces correspond to the propagation electrodes while the left-right faces to the lateral electrodes. Single element conventional transducer (blue case). Front-back faces correspond to the propagation electrodes.

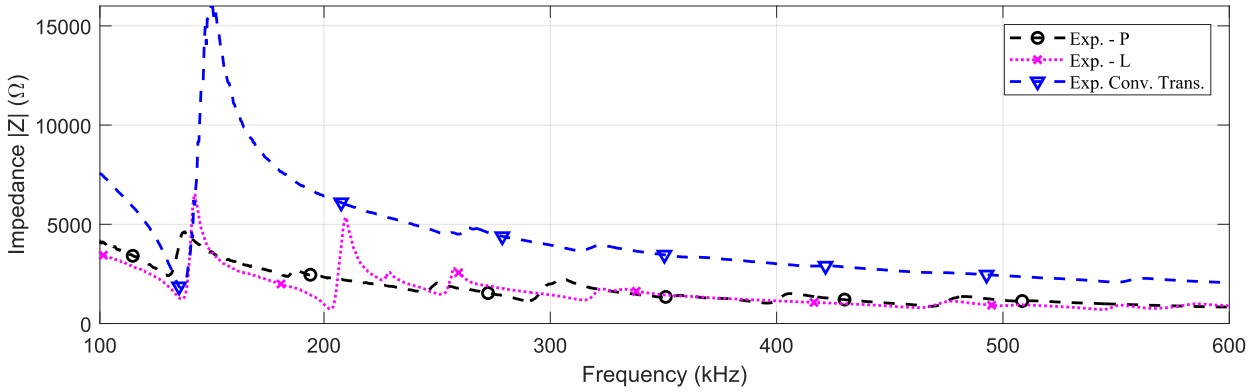

Fig. 5. 8. Average impedance response for the experimental single-element prismatic-shaped biaxial and conventional transducers.

By using the electrical characterization from the experimental transducer, viscous damping C_β can be added to the FEA model to properly match results by adding losses. When a structure is under a harmonic excitation, C_β can be approximated as[134]

$$C_\beta = \frac{1}{\omega Q_m} \tag{5.13}$$

With ω being the angular frequency and Q_m the quality factor. The quality factor in a transducer represents the crystal's resonance quality[19] and is inversely proportional to the bandwidth, implying that narrow band transducers (therapy) have a large Q_m and wider band transducers (imaging) a low Q_m.The Q_m can be calculated by analyzing the admittance response of the transducer and using[135]

$$Q_m = \frac{f_r}{f_2 - f_1} \tag{5.14}$$

with f_r representing the resonance frequency, f_2 and f_1 the left and right -3 dB frequency. For the simulated model, a value of $\beta = 1.78x10^{-8}$ was used. In addition, the mesh size of the piezoceramic element was reduced to 0.5 mm to cover a broader band of frequencies (100 kHz to 600 kHz).

5.2.1 Acoustic field distribution

The acoustic pressure characterization of each transducer was performed by using a 2 mm-diameter needle hydrophone (NH2000, Precision Acoustics, Dorset, UK). The hydrophone was mounted on a robotic 3D-positioner system (UMS3 Scanning tank, Precision Acoustics, Dorset, UK) placed 2 mm away from the transducer inside a tank filled with deionized and degassed water. The conventional transducers were driven with a 10-cycle sinusoidal burst , to avoid damaging the hydrophone, with a repetition frequency of 100 Hz produced by a dual-channel function generator (33522A, Agilent Technologies, CA, USA) and amplified (240L, E&I, NY, USA). The voltage amplitude was set to reach an electrical power of 1 W in continuous mode at the resonance frequency of the transducer.

The biaxial transducers were driven with a 10-cycle sinusoidal burst using the propagation resonance frequency with a burst repetition frequency of 100 Hz and power of 1 W at the P-electrodes. The same range of values of ϕ and p_l as in simulations were tested: ϕ was varied from 0° to 315° with a 45° step and p_l was maintained at 0.1, 0.5, and 1 W. For hydrophone measurements of the biaxial transducers, the order of combination of ϕ and p_l were randomized to avoid any hysteresis error or contributions related to heating. The acoustic field was measured with the hydrophone on the XZ-plane using a 0.5 mm-resolution step. The region covered on the X-axis ranged from –5 mm to +5 mm from the center of the

transducer while on the Z-axis, it went from 2 mm to 8 mm away from the transducer. The hydrophone acoustic measurement signal was coupled (DC Coupler, Precision Acoustics, Dorset, UK), amplified (Hydrophone Booster Amplifier, Precision Acoustics, Dorset, UK), and digitized with an oscilloscope (DSOX3024A, Keysight, Santa Rosa, CA). The diagram for the setup is shown in Fig. 5.9. Also, to have a baseline of the beam profile for calculating the steering angle, the acoustic pressure was measured using only the P-electrodes. The voltage was set to produce 1 W of electrical power in continuous mode.

For each of the biaxial transducers, the steering angle γ was calculated as described in section *5.1.3*. The measured acoustic pressure fields were normalized and interpolated to a 0.1 mm resolution.

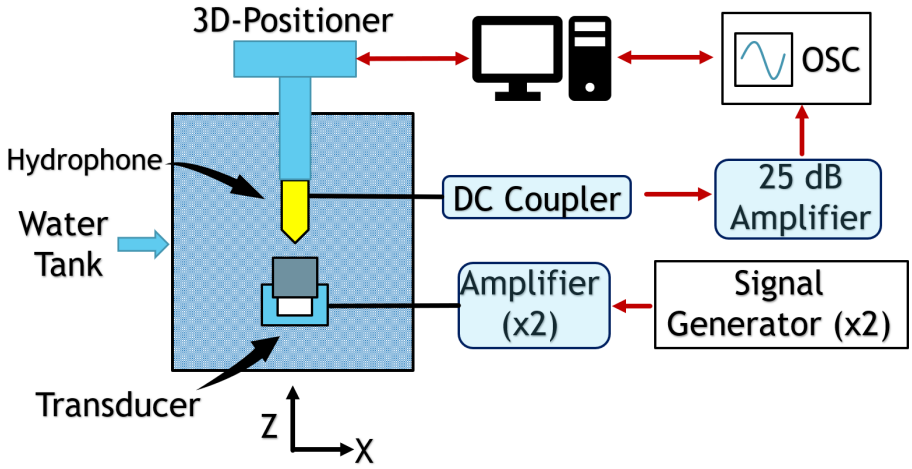

Fig. 5. 9. Setup for the acoustic field characterization of a biaxial ultrasound transducer.

5.2.2 Acoustic efficiency

For the characterization of the acoustic efficiency of conventional transducers, a continuous sinusoidal signal was produced by a dual-channel function generator (33522A, Agilent Technologies, Santa Clara, CA) and amplified it (240L, E&I, Rochester, NY). The signal had a power of 2 W at the transducer f_r measured with a power meter (N1914A, Agilent Technologies, Santa Clara, CA). The acoustic power was calculated with the radiation force method[136] and an analytical scale (NewClassic MS, Mettler Toledo, Columbus, USA). The transducer was placed directing downward at a distance of 2 cm from a 6 cm-diameter absorber (HAM A, Precision Acoustics, Dorchester, Dorset, UK) located on the bottom of a vessel filled with deionized and degassed water. The acoustic power was calculated using the following equation[68], [136]

$$W_A = \frac{mgc}{\cos\gamma} \tag{5.15}$$

where m is the change in mass measured by the analytical scale 8 s after continuous driving, g is the acceleration due to gravity ($9.81\ ms^{-1}$), c is the speed of sound in water at room temperature, and γ is

the steering angle. The coefficient $(\cos\gamma)^{-1}$ determines the vertical contribution of the steered acoustic field to the force measured by the analytical scale[68], [136]. The measurements were performed three times on different days.

For the characterization of the acoustic efficiency of the biaxial transducers, two independent sinusoidal signals were applied to each set of electrodes and varied ϕ and p_l at the L-electrodes while maintaining the power of 1 W at the P-electrodes. Each biaxial transducer was driven with a dual-channel function generator (33522A, Agilent Technologies, Santa Clara, CA) and two power amplifiers (240L, E&I, Rochester, NY and AG 1021; T&C Power Conversion, Rochester, NY). The driving signal frequency for both pairs of electrodes was set to the propagation f_r . The effective electrical power delivered to each set of electrodes was measured with two power meters (N1914A & E4419B, Agilent Technologies, Santa Clara, CA). The experimental setup for the efficiency characterization of the biaxial transducer is shown in Fig. 5.10. ϕ was varied from 0° to 350° with a 10° step for each value of p_l (0.1, 0.5, and 1.0 W). Three repeated measurements were performed per transducer for each combination of ϕ and p_l, and the order of those combinations was randomized. W_A was also measured with the biaxial transducers being driven with only the P-electrodes with 2 W to produce a baseline of conventional mode driving.

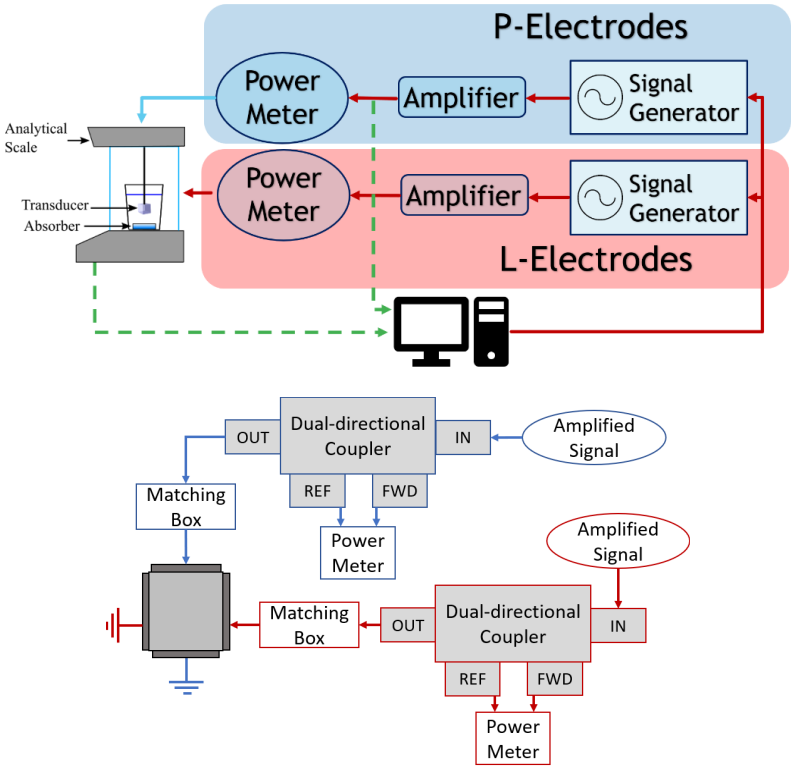

Fig. 5. 10. Setup for the efficiency characterization of a biaxial ultrasound transducer. Top) General setting describing the transducer positioning within the balance. Bot) Description of the power meter connection and piezoceramic.

5.2.3 Electrical impedance validation

Fig. 5.11 compares the simulated and experimental impedance measurements. For the prismatic biaxial transducer, simulations predicted a f_r and impedance of 133 kHz and 2352 Ω at the P-electrodes, respectively. For the L-electrodes, the model predicted values of 145 kHz and 1829 Ω. The experimental f_r average (± s.d.) for the three biaxial transducers was 131.0 ± 0.0 kHz on the P-electrodes with an impedance of 2399 ± 53 Ω. In the case of L-electrodes, the average f_r and impedance were 137.2 ± 0.6 kHz and 1210 ± 156 Ω, respectively. For three conventional transducers (no L-electrodes), the average resonance frequency was 137.5 ± 0.9 kHz with an average impedance of 1856 Ω ± 215 Ω. The simulation for a conventional transducer presented an impedance of 3919 Ω with resonance frequency at 133 kHz.

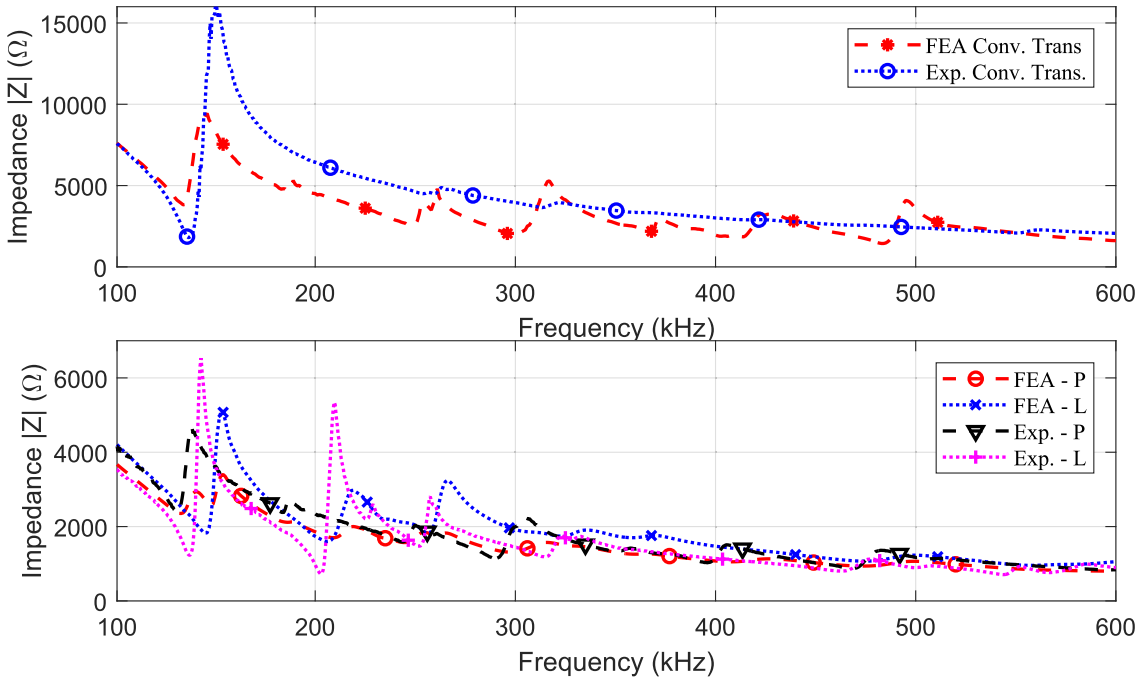

Fig. 5. 11. Comparison of average impedance at the propagation (P) and lateral (L) electrodes between the simulation (FEA) and experimental (Exp) conventional (top) and biaxial (bottom) transducers.

5.2.4 Acoustic pressure response: Steering validation

Fig. 5.12 shows the normalized acoustic pressure field of the biaxial transducer B_1, conventional transducer C_1, and the simulated model along the XZ-Plane on a logarithmic scale. When using conventional driving, simulations predicted an ultrasound beam directed at an angle of 0° relative to the Z-axis, which is expected in ideal conditions. The highest values of γ for the simulation were predicted with $p_l = 1$ W (bot-left and bot-right row in Fig. 5.12), with a maximum value of $\gamma = -28.3°$ at $\phi = 90°$ and $\gamma = 30.9°$ at $\phi = 315°$. The middle-left and middle-right rows in Fig. 5.12 shows the experimental

acoustic profiles of the biaxial transducer B_1 at $\phi = 135$ and $\phi = 270°$ for $p_l = 1$ W corresponding to γ values of $-25.5°$ and $25.9°$. The simulated and experimental acoustic profiles exhibited an asymmetric response between the achieved steering in the positive (right) and negative (left) directions.

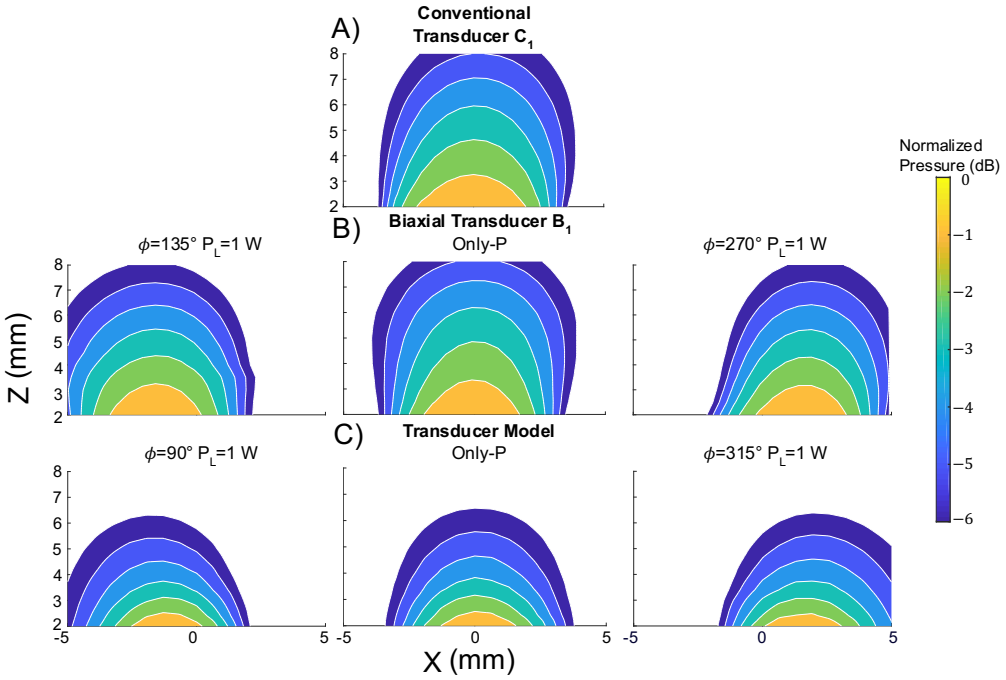

Fig. 5. 12. Normalized acoustic pressure fields with contours at −6 dB. A) Acoustic pressure measured on the conventional transducer C_1. B) Propagation-only mode for the biaxial transducer B_1 (center) with its respective maximum negative and positive steering acoustic field (left and right). C) Maximum negative and positive steering (left and right) produced by the biaxial model and compared with its respective conventional driving mode (center).

Fig. 5.13 shows the simulated and experimental results of γ as a function of ϕ at all the tested values of p_l. The model predicted a sinusoidal-type response between γ and ϕ, which experimental validation agreed well with the predicted shape response. Maximal steering increased as a function of the applied lateral power. The highest experimental γ for the biaxial transducers was $30.2° \pm 4.4°$ at $\phi = 270°$ and $-24.5° \pm 3.9°$ at $\phi = 135°$, at $p_l = 1$ W. Table 5.3 shows a summary of the findings.

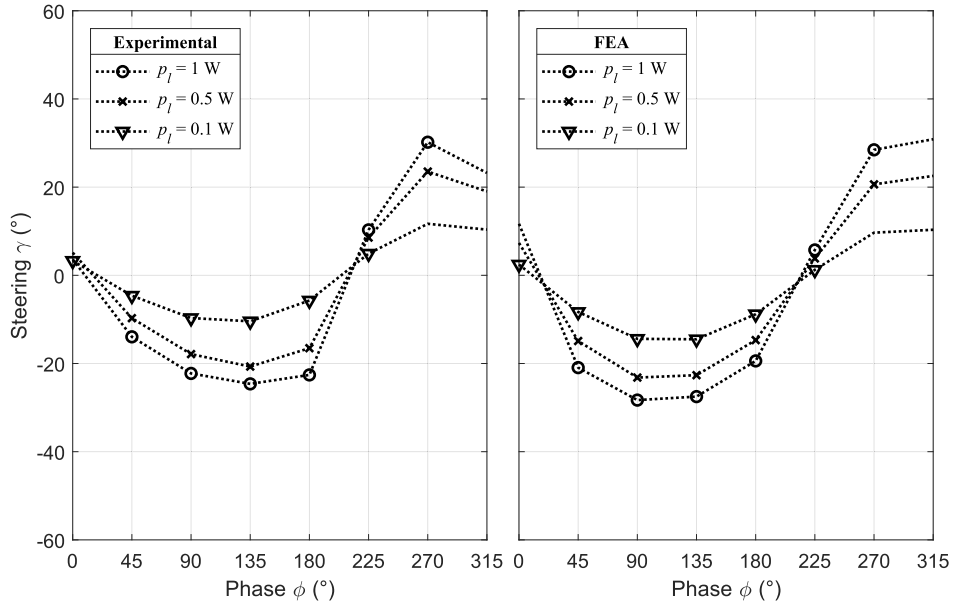

Fig. 5. 13. Steering response as a function of phase difference for three experimental biaxial transducers and the simulated transducer model at different p_l.

Table 5. 3 Maximal steering predicted by the FEA PZT model and experimental measurements (n=3)

p_l **(W)**	**Negative steering (left)**				**Positive steering (right)**				**Peak-peak steering**		
	FEA		Experiments		FEA		Experiments		FEA	Experiments	Difference
	ϕ (°)	γ (°)	ϕ (°)	γ (°)	ϕ (°)	γ (°)	ϕ (°)	γ (°)	(°)	(°)	%
0.1	135	–14.5	135	–10.4 (±1.5)	315	10.3	270	11.7 (±1.9)	24.8	22.1	4.5
0.5	90	–23.2	135	–20.7 (±2.2)	315	22.6	270	23.5 (±3.5)	45.8	44.2	3.5
1.0	90	–28.3	135	–24.5 (±3.9)	315	30.9	270	30.2 (±4.4)	59.2	54.7	7.6

5.2.5 Efficiency (η) as a function of phase and power

Fig. 5.14 illustrates the simulated and experimental relationship between η and ϕ with different power levels applied to the L-electrodes. A sinusoidal relationship between η and as ϕ was observed, and the overall η was inversely proportional to p_l. Biaxial driving simulations showed a maximum η of 36.5% at 133 kHz for $\phi = 45°$ and $p_l = 0.1$ W. With conventional driving by applying 2 W at 133 kHz, the value of η was calculated to be 37.9%. For biaxial driving experiments of transducers B_1, B_2, and B_3, the maximal η was, respectively, 34% ± 2.8%, 34.3% ± 2.1%, and 28.3% ± 2.2%, at $p_l = 0.1$ W and ϕ = 20°, 30°, and 50°, respectively. When the three biaxial transducers were driven through P-electrodes alone, the average η was 30.3% ± 3.9% at their respective propagation f_r. Experimental results for the three conventional transducers showed an average η of 31.2% ± 2.3%.

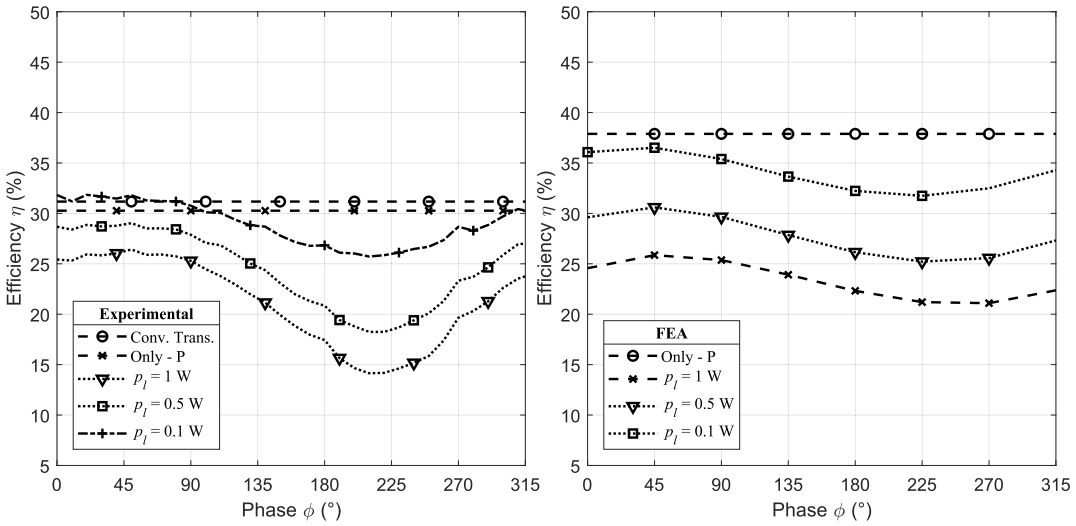

Fig. 5. 14. Average η vs. ϕ for the three biaxial transducers (left) and corresponding FEA predictions (right) for η vs. ϕ for the same values of p_l.

5.2.6 Discussion

The simulated and experimental results for the PZT biaxial transducer demonstrated that the biaxial driving of a single-element transducer can effectively steer the ultrasound beam, and that the steering can be controlled using the phase and power applied to L-electrodes. To the best of our knowledge, this is the **first time that ultrasound beam steering using a single-element transducer has been demonstrated**.

As shown in Fig. 5.13 the beam steering angle exhibits a sinusoidal response with respect to ϕ, with maximum steering angles for simulated and experimental measurements at ϕ values of 90° ± 45° and 285° ± 26°, for left and right steering, respectively. Decreasing the power from 1 W to 0.1 W on the L-electrode while maintaining it at 1 W on the P-electrode reduced the maximum steering value that could be obtained, meaning that we could control steering by either reducing power on the L-electrodes or by changing the phase difference between electrodes. The average difference for the peak-peak steering between the simulated model and the averaged biaxial transducers was 5.2%.

An excellent agreement could be observed between the impedance response obtained from simulations and experiments for the PZT biaxial transducers. Relative to the predictions, $f_r$of the P- and L-modes showed an absolute difference between FEA and experiments of 2 kHz and 7.8 kHz, corresponding to a difference of 1.5% and 5.4%, respectively. The experimental difference between the propagation resonance frequencies of conventional and biaxial transducers was only 4.9%, with an on-resonance impedance and an absolute difference of 22.6%, relative to the experimental biaxial transducer.The

difference in f_r for the simulated and experimental conventional transducer was only 4 kHz. However, there was an absolute impedance difference of 2134 Ω. In addition, the absolute difference in the average experimental and simulated impedance for the P-electrodes was 47 Ω, while that for the L-electrodes was 619 Ω, having relative differences of 2% and 51% in relation to the prediction. The difference in the impedance is attributed to the clamping effect of the silicone glue used to adhere to the piezoceramic material to the acrylonitrile-butadiene-styrene (ABS) casing.

While the addition of the second set of electrodes can provide control for the steering of ultrasound of a single-element transducer, compared to the conventional transducer, the second set of electrodes did not result in significant variations in the acoustic field when only the P-electrodes were driven. We can also foresee that a supplemental third set of electrodes may be implemented on such a rectangular structure to produce a steered beam on the YZ-plane in addition to the steered beam in the XZ-plane. In addition, the application of the biaxial driving in piezoceramic shapes, such as rings, can modify the ultrasound formation in the near field, as the controllable steering can have an effect given the axisymmetric configuration of a ring device.

The non-symmetric response for the steering γ observed in the simulated and experimental acoustic profiles of biaxial transducers (Fig. 5.12) can be related to changes on the amplitude deformation along the Z-axis in the piezoceramic due to the addition of the second set of electrodes and the driving frequency used on the L-electrodes. Supplementary simulations were performed to calculate the amplitude of deformation over the Z-axis of two opposite corner nodes (right and left) on the front face of the FEA model while driving only the L-electrodes. The simulations were performed for the cases where the P-electrodes are modeled as a coupled equipotential set of nodes and when P-electrodes were not modeled at al. Overall, we observed that the piezoceramic deformation due to lateral excitation loses symmetry by the presence of the P-electrodes, and this asymmetry increases as it was driven away from its resonance frequency. The deformation of the two corner nodes in the FEA models is shown in Fig. 5.15. It was found that at the simulated f_r of the L-electrodes (145 kHz), the right and left nodes underwent deformations of 693 nm and 632 nm, respectively (a difference of 61 nm) in the presence of P-electrodes while deformations of 755 nm and 744 nm (11 nm difference) were observed for the absence of P-electrodes. However as the L-electrodes were driven with the propagation f_r during biaxial excitation, the amplitude of the deformation when the propagation resonance frequency (133 kHz) was used to drive both sets of electrodes produced deformations of the right and left nodes of 237 nm and 72 nm, respectively (a difference of 165 nm) in the presence of P-electrodes. The deformation changed to 245 nm and 243 nm

(2 nm difference) when the P-electrodes were absent. These deformation differences between nodes explains the asymmetric steering response, which is produced by the addition of the two set of electrodes and increases due to driving out of resonance.

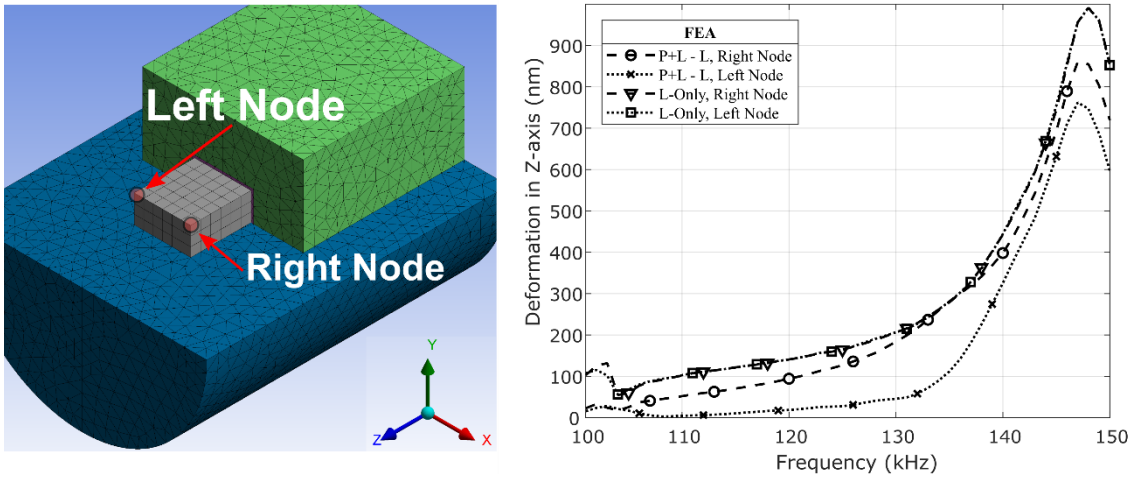

Fig. 5. 15. Left) Location of the right and left nodes on the front face of the piezoceramic material in the FEA model. Right) Deformation (Z-axis) vs frequency of the right and left nodes. The lateral and propagation resonance frequencies are 145 kHz and 130 kHz, respectively.

The biaxial method will offer new opportunities to develop a new generation of phased-arrays, where low-frequency conditions would be desirable. For the medical use of focused ultrasound for transcranial therapy[137], where the skull barrier imposes a limit to the maximum usable ultrasound frequency (often between 200 kHz and 700 kHz), a higher degree of focusing is highly desirable, especially for emerging applications such as neurostimulation with focused ultrasound[137]. Ultrasound imaging applications can certainly benefit of an improved axial resolution of imaging with phased-arrays. Also, the biaxial method may open new opportunities for innovative imaging techniques that can exploit this new type of steering.

The difference in η between conventional and biaxial transducers with propagation-only driving was only 0.9%, which was not statistically significant ($p = 0.73$, Student t-test). This observation indicated that the addition of a second set of electrodes on the lateral faces of the piezoceramic did not produce statistically significant variations in η. From these results, it was observed that steering affects the η, and that this loss of efficiency while steering will require consideration for biaxial driving. Optimization of driving conditions can be possible by testing different frequencies in addition to the propagation resonance. It has been previously reported[138], [139] that higher efficiencies can be achieved at frequencies slightly off from the propagation resonance frequency. For future work, we will explore the

use of larger elements driven at harmonic frequencies to achieve better efficiency with higher frequencies.

For both predictions and experimental measurements, the maximum steering values were found for a p_l = 1 W, while the maximum η was observed with p_l = 0.1 W. Table 5.4 shows a summary of the conditions for simulations and experiments. These results suggest that there is a trade-off between η and the steering angle γ that must be compensated for by modifying the total amount of power applied to the biaxial transducer when changing ϕ. Regarding to η, we could not find a statistically significant increment ($p = 0.69$) while using biaxial driving.

Table 5. 4 Comparison of conditions for maximum γ and η

	MAXIMUM γ		**MAXIMUM η**	
	FEA	**Exp**	**FEA**	**Exp**
γ (°)	30.9	30.2	−8.3	−2.5
η (%)	22.4	19.7	36.5	32.2
ϕ (°)	315	270	45	33.3
p_l (W)	1.0	1.0	0.1	0.1

5.3 Single element Ring-shaped transducer

The biaxial driving efficiency and steering response were described for prismatic-shaped ultrasound transducers in section 5.1 and 5.2. As different piezoceramic shapes produce different vibration modes, a ring-shaped transducer is proposed to be driven with a biaxial excitation due to its advantageous geometrical form being adequate to place the two sets of electrodes required for the biaxial driving. A 3D-FEA model was used within the software Ansys Workbench to describe the conventional and biaxial response of single-element ring-shaped transducers made of Lead Zirconate Titanate (PZT, DL-47, Del Piezo Specialities, LLC, West Palm Beach, FL, USA) and the results compared to a set of two fabricated ring biaxial transducers. The purpose of the ring-shaped transducer is to compare how different the acoustic pressure distribution is against a prismatic transducer. Prismatic transducer tends to have a non-focused response, while ring-shaped transducers are more suitable for focusing. The biaxial driving technique and its implications in the efficiency and acoustic pressure response are studied in this section.

The simulation consisted of a harmonic analysis performed in the range of 470 kHz to 530 kHz to cover the first vibration modes of the piezoelectric transducer. The ring piezoceramic has an outer diameter of 12.1 mm, an inner diameter of 7.7 mm and a thickness of 3.1 mm. The ring was poled along the propagation axis (Z), and it was enclosed in a 15 mm diameter ABS plastic disk with an inner diameter of 12.1 mm and a thickness of 4 mm. A 14 mm diameter 2 mm thickness cork disk was placed behind the

disk to work as a support. A water cylinder with a diameter of 15 mm and a height 20.7 mm was used in simulations as the propagation medium. The model has a mesh size of 0.625 mm. The P- (front and back faces) and L- (outer and inner faces) electrodes were modelled as coupled equipotential sets of nodes, and an acoustic absorption boundary condition was applied on the outer walls of the water medium to avoid reflected waves[119], [121], [126], [132]. A damping value of $C_\beta = 9.21x10^{-9}$ was used for this simulation. Fig. 5.16 shows the complete 3D model used for the simulation and the experimental transducer. The material properties for piezoelectric, acoustic and structural domains are included in Appendix A.

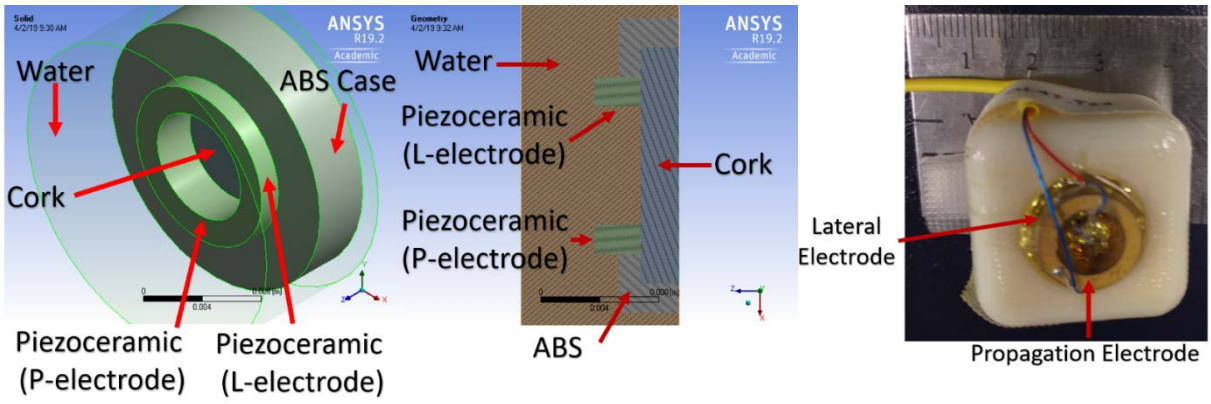

Fig. 5. 16. Left) 3D-FEA model of a ring-shaped biaxial transducer poled along the propagation direction (Z-Axis). Right) Experimental biaxial ring transducer.

The characteristic equations to calculate the impedance, applied electric power, acoustic power and acoustic pressure for the FEA model are described in section 5.1. The electric impedance characterization to determine f_r of each transducer was performed by using a vector network analyzer (ZNL3, Rode & Schwarz, Munich, Germany). The same setup described at section 5.2.1 was used to characterize the acoustic field of the biaxial ring transducers by measuring it with the hydrophone on the XZ-plane using a 0.5 mm-resolution step. The region covered on the X-axis ranged from –4 mm to +4 mm from the center of the transducer while on the Z-axis, it ranged from 2 mm to 14 mm away from the transducer. The efficiency measurements for the experimental ring transducers were performed by using the setup described in section 5.2.2. The degree of which the ultrasound focus can be repositioned by applying the biaxial driving technique was calculated by analyzing the acoustic beam profiles generated by the transducer with biaxial and conventional driving by calculating the Z-component of the centroid (Ψ) in the XZ-plane within –6 dB of the normalized acoustic pressure distribution for conventional (Ψ_C) and biaxial (Ψ_B) driving conditions for every combination of ϕ and p_l at the propagation resonance frequency.

5.3.1 Transducer driving

A single electric field was applied onto the P-electrodes of the biaxial transducer to represent the conventional driving. The applied signal consisted of a 2-cycle sinusoidal burst, to avoid heating and damaging the hydrophone, with a repetition frequency of 100 Hz for a power of 2 W at the propagation f_r and the electric impedance, the applied electric power (W_E) on the propagational electrode, the acoustic power (W_A) on the water cylinder 5 mm away from the transducer face, the acoustic pressure on the XZ-plane, and η were calculated.

For the biaxial driving of single element ring transducers, two orthogonal electric fields connected to independent sinusoidal signals (2-cycle burst, 100 Hz repetition frequency) were applied onto the propagation and lateral electrodes. For both, simulated and experimental transducers, the power at the P-electrodes was kept constant at 1 W. ϕ was varied from 0° to 315° with a 45° step for $p_l = 0.1$ and 1 W. The electric impedance at both electrodes, the sum of the effective electric power at both electrodes (W_E), acoustic power (W_A) on the water cylinder 5 mm away from the transducer, η and acoustic pressure on the XZ-plane were calculated at every value of ϕ and p_l tested.

5.3.2 Impedance analysis

The simulation predicted a f_r and impedance of 519 kHz and 320.4 Ω, respectively, at the P-electrodes and 495 kHz and 143 Ω for the L-electrodes. The averaged experimental ring transducers presented a propagation f_r of 491.3 kHz ± 2.5 kHz with an impedance value of 295.9 ± 16.4 Ω, and for the L-electrodes a f_r of 473.5 kHz ± 12.7 kHz with an impedance value of 175.2 Ω ± 4.4 Ω. Fig. 5.17 shows the simulated impedance response for the ring transducer.

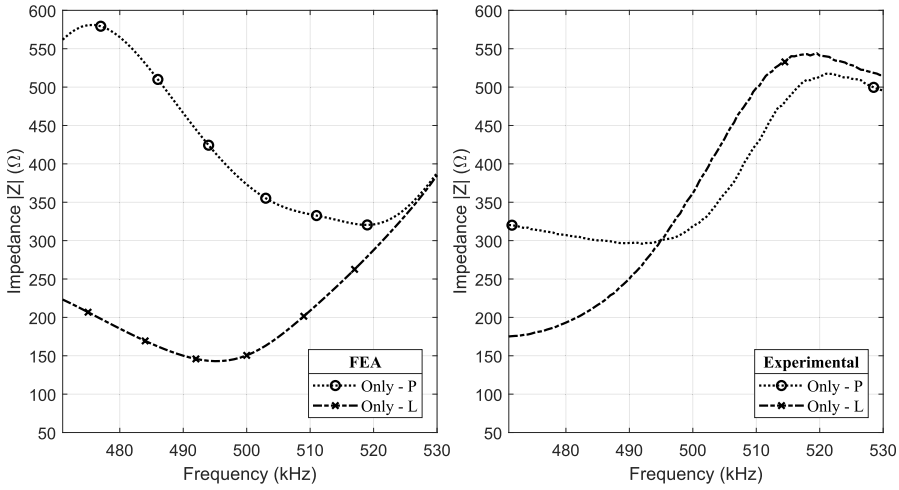

Fig. 5. 17. Electric impedance at the propagation (P) and lateral (L) electrodes of the simulated (left) and experimental biaxial ring transducer.

5.3.3 Acoustic field analysis

The normalized acoustic pressure field along the XZ-Plane on a logarithmic scale for the simulation and the biaxial ring transducer R_1 are shown in Fig. 5.18. When using conventional driving, simulations predicted an ultrasound focal point (-6 dB) positioned at a distance of 8.6 mm and can be reduced up to 0.6 mm focal length with biaxial driving at $\phi = 360°$ for $p_l = 0.1$ W. The acoustic profiles of the biaxial ring transducer R_1 (top, Fig. 5.18) shows a focal point positioned at 9 mm ± 0.2 mm for conventional driving and reduced up to 4.5 mm ± 0.2 mm at $\phi = 0$ with $p_l = 1$ W. Fig. 5.19 shows the simulated and experimental results of the focal displacement as a function of ϕ at all tested p_l. It is worth noting that the acoustic field area was reduced for both cases while reducing the focal displacement, as shown in Fig. 5.20. Table 5.5 shows a summary of the findings.

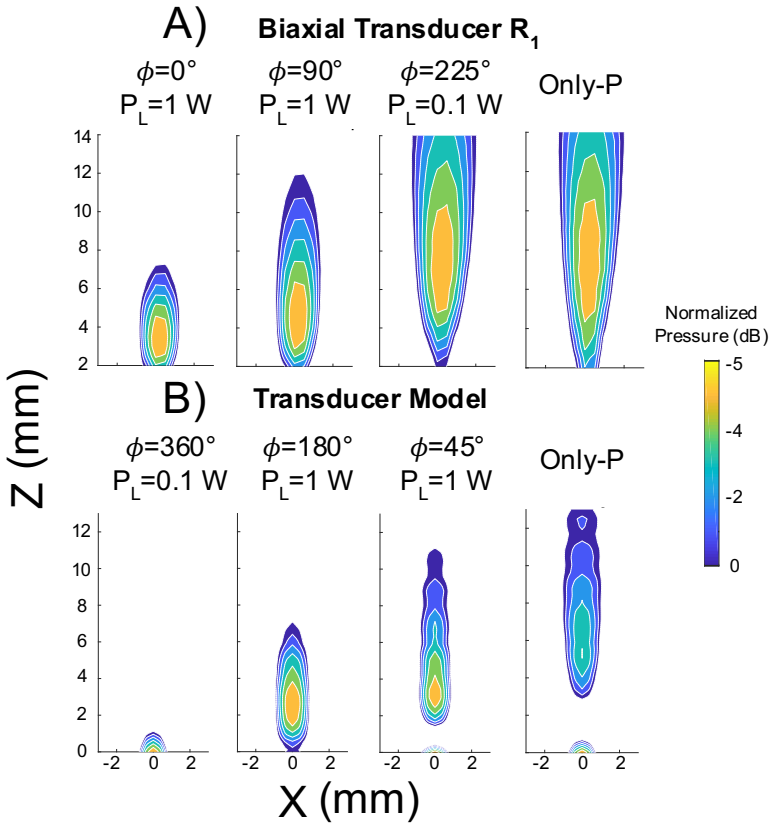

Fig. 5. 18. Normalized acoustic pressure fields with contours at −6 dB of the focal distance progression through the biaxial excitation (first 3 plots from the left) compared to conventional driving (right). A) Experimental measurements for the biaxial transducer R_1. B) FEA Simulations

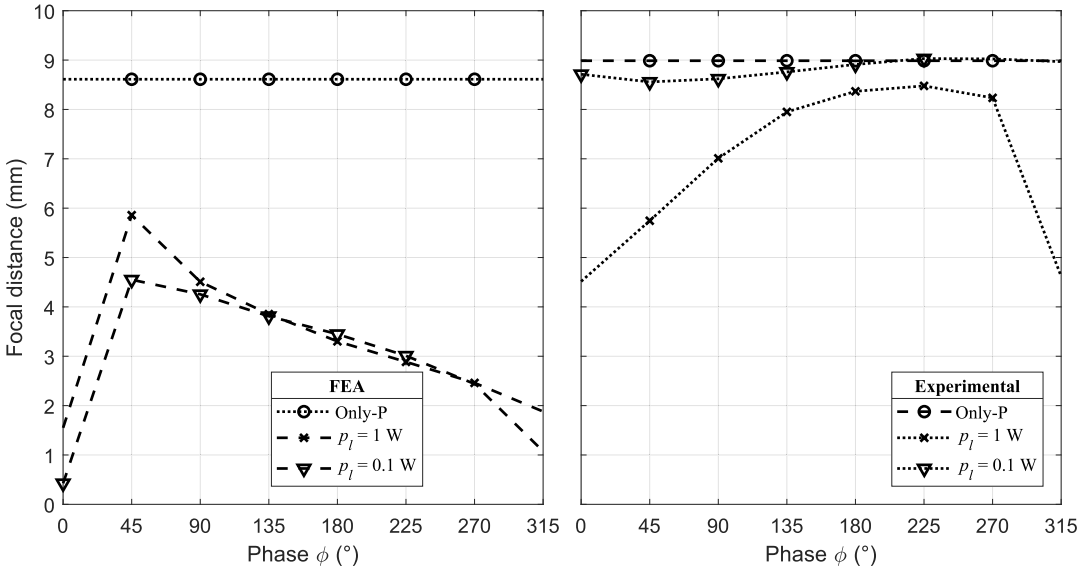

Fig. 5. 19. Focal distance as a function of ϕ and p_l for the simulation (left) and experimental biaxial ring transducer.

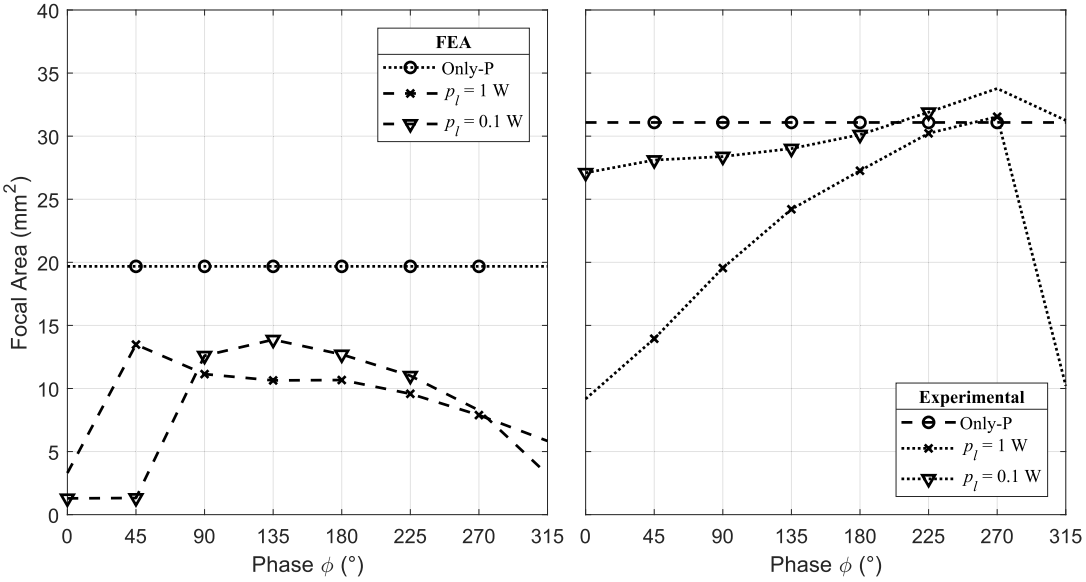

Fig. 5. 20. Focal area as a function of ϕ and p_l for the simulation (left) and experimental biaxial ring transducer.

Table 5. 5 Focal displacement predicted by the simulation and experimental measurements (n=2)

p_l **(W)**	**Minimum distance**				**Maximum distance**				**Peak-peak distance**	
	FEA model		Experiments		FEA model		Experiments		FEA Model	Experiments
	ϕ (°)	mm	ϕ (°)	mm	ϕ (°)	mm	ϕ (°)	mm	mm	mm
0.1	0	0.4	45	8.6 (±0.2)	45	4.6	270	9.0 (±0.1)	4.2	0.4
1.0	0	1.6	0	4.5 (±0.2)	45	5.9	225	8.5 (±0.1)	4.3	4

5.3.4 Efficiency (η) as a function of phase and power

Simulations showed a maximum η of 31.7% at 519 kHz for biaxial driving at $\phi = 90°$ and $p_l = 0.1$ W. Conventional driving with 2 W at 519 kHz produced a value of η = 17.5% . When the two biaxial ring transducers were driven through the P-electrodes alone, the average η was 32.2% at their respective propagationf_r. Biaxial transducers R_1 and R_2 exhibited a maximum efficiency of 33.3% and 33.4%, respectively, at $p_l = 0.1$ W and ϕ values of 40° and 330°. The average maximal efficiency of these transducers was 33.4%, which was higher than that of conventional driving. Fig. 5.21 illustrates variations in η as a function of ϕ, both experimentally and simulated, for the different values of p_l tested.

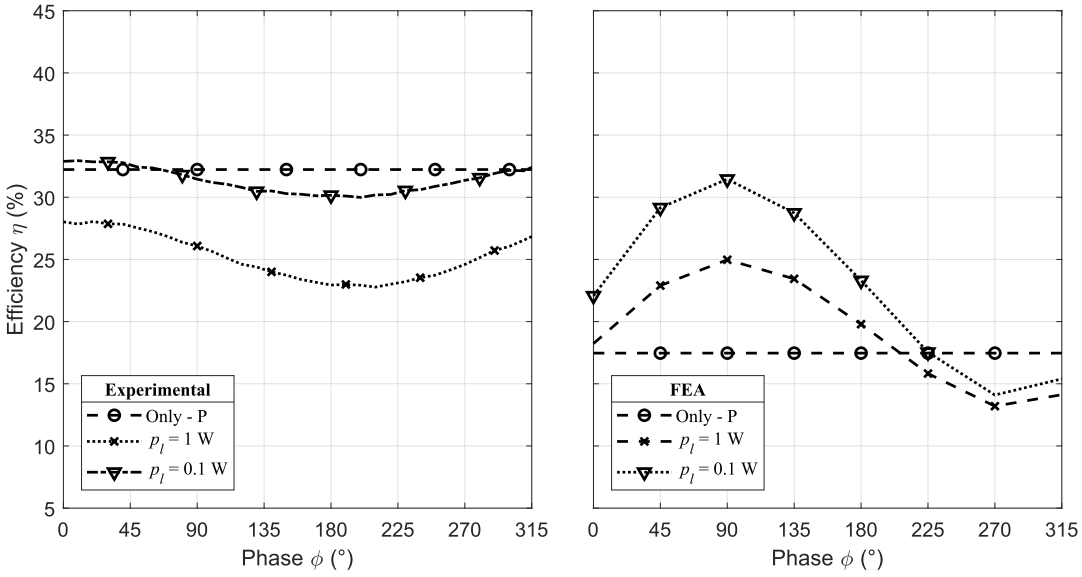

Fig. 5. 21. Average η vs ϕ for the two ring biaxial transducers (left) and corresponding FEA predictions for the same values of p_l.

5.3.5 Discussion

The simulated and experimental results for the PZT biaxial transducer demonstrated that the biaxial driving of a single-element transducer could effectively control the focal point positioning of the ultrasound beam by using different ϕ and p_l values. To the best of our knowledge, this is the first time that a controlled refocusing ultrasound beam from a single-element transducer has been demonstrated. The changes in the focus displacement did not follow the previous sinusoidal response with respect to ϕ as the efficiency or the steering presented on the prismatic transducer. Instead, it follows a response similar to an inverse parabolic shape for both cases of study. For the experimental case, decreasing the power from 1 W to 0.1 W also reduced the capability of the biaxial driving to reduce the focal distance. However, this was not shown on the simulations, which predicted no significant variations while reducing p_l. For both cases, the maximum focal distance tends to be at the focal point produced by conventional driving, meaning that we can control the focal length by either reducing p_l or changing ϕ . Also, the total acoustic pressure area was reduced while decreasing the focal point distance from 19.7 mm^2 at conventional driving to 1.3 mm^2 at $\phi = 0°$ and $p_l = 0.1$ W for the simulations and from 31.1 mm^2 ± 1.5 mm^2 at conventional driving to 9.2 mm^2 ± 0.4 mm^2 for the averaged experimental transducers, which is a 29.6% total area reduction.

An excellent agreement could be observed between the impedance response obtained from simulations and experiments for the PZT biaxial transducers. Relative to the prediction, the resonance frequencies of the propagation and lateral modes showed an absolute difference between simulations and experiments of 27.7 kHz and 21.5 kHz, corresponding to a difference of 5.3% and 4.3% with respect to the predictions. In addition, the absolute difference in the average experimental and simulated impedance for the propagation electrodes was 24.5 Ω, while that for the L-electrodes was 32 Ω, corresponding to relative differences of 7.6% and 22.4% to the prediction. The difference in the impedance was attributed to the clamping effect of the silicone glue used to adhere to the piezoceramic material to the casing.

The maximum value of η predicted by simulations was 31.7% at ϕ = 90° and p_l = 0.1 W, while the averaged maximum experimental η with the biaxial transducers was 32.9% ± 0.1% at ϕ = 10° and p_l = 0.1 W resulting in a η difference of 1.7%. For both cases, η resulted in the previously described sinusoidal shaped from prismatic transducers, giving a strong suggestion that regardless of the transducer shape, the efficiency is going to have this response. For the specific case of the simulated model, the maximum biaxial η was 14% higher than its conventional driving. However, for the experimental cases, there was only a

0.7% higher η when compared with conventional driving. This difference may be produced by the simulated material properties of the cork which are just an aproximation and the silicone not included into the simulation, which purpose was to reduce simulation time. These results for efficiency as a function of ϕ and p_l suggest that for both, the FEA biaxial model and the averaged experimental measurements, the applied power needs to be compensated while using different focal displacements while testing different ϕ and p_l is the same acoustic power is required to keep constant.

CHAPTER 6: BIAXIAL IMAGING PROBE

Ultrasound imaging is one of the most critical applications of piezoelectric transducers. Since sensitivity can significantly impact the signal-to-noise ratio (SNR) in ultrasound probes, we decided to explore the effect of the biaxial driving technique for this application. Also, the possibility to steer the beam could open new avenues for the improvement of imaging resolution by shaping the acoustic beam.

In this work, we have obtained the initial experimental results for the biaxial driving of an ultrasound transducer for imaging. We present the initial results on biaxial driving on reception mode and its impact on the signal-to-noise ratio and resolution. Future work will explore the opportunities that steering can generate for imaging applications.

6.1 Biaxial imaging prototype

A four element PZT ultrasound imaging transducer was built by the "Device Development Laboratory" (DDL, Sunnybrook Research Institute). Fig. 6.1 shows a picture of the final device. Each element has a length of 26 mm, thickness (propagation direction) of 0.6 mm and a width of 0.6 mm with a gap between elements of 1 mm to 1.4 mm. On the top and bottom part of each element (propagation direction), silver epoxy (H20E, Epoxy Technology, MA, USA) was used as conductive matching (0.14 mm-thickness) and backing (1.9 mm-thickness) layers. It was recommended by DDL to use the device at 6 MHz. However, the presence of ringing was detected on internal tests at DDL.

Fig. 6. 1. Four-Elements ultrasound imaging biaxial probe.

6.1.2 Electrical Safety tests

Before connecting the probe for the first time with the 128 Vantage system (Verasonics, Kirkland, WA, USA) a series of tests were conducted to verify the presence of short circuits on each of the four elements. The test consisted of measuring continuity with a multimeter (Fluke 117, Fluke Corporation, WA, USA) at the active and ground face of each element with its respective pin on the Canon ZIF connector. It was found that electrodes 1 and 2 on element A (Fig. 6.2) had a short circuit. Due to the fragility of the connectivity on the transducer side, and to avoid damaging to Verasonics system, it was decided not to use element A.

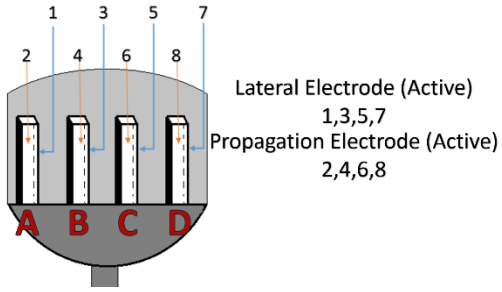

Fig. 6. 2. Biaxial probe elements configuration.

6.1.3 Hydrophone measurements of biaxial mode

Fig. 6.3 shows the experimental setup for the acoustic field acquisition. A 0.075 mm-diameter needle hydrophone (Precision Acoustics, Dorset, UK) was used to register the acoustic field produced by the ultrasound probe. The hydrophone was mounted on a robotic 3D-positioner. Acoustic pressure measurements were collected for each transducer element by placing the hydrophone 2 cm from the central region of the transducer element. Measurements with the hydrophone were coupled, amplified and then digitized with an oscilloscope (Waverunner XPS, LeCroy). Driving of the transducer was performed using the 128 Vantage system (Verasonics, Kirkland, WA, USA).

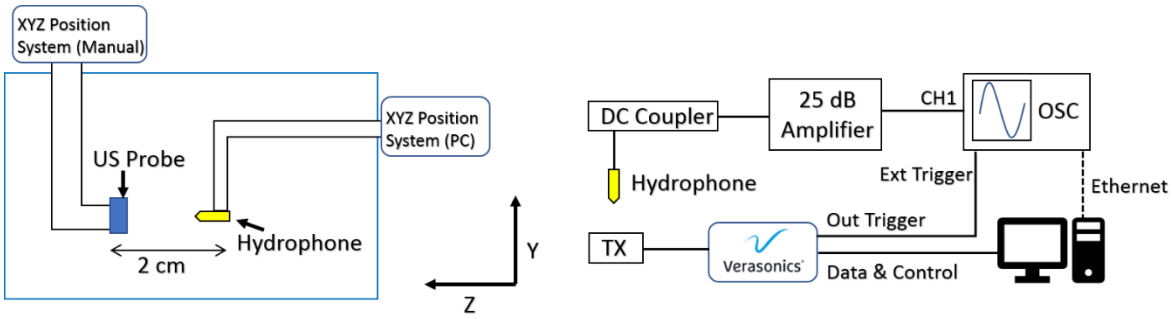

Fig. 6. 3. Left: Transducer & hydrophone setup inside a water tank. Right. Electronics setup.

6.1.3.1 Phase variation test

A series of acquisitions were performed using the Verasonics system while biaxially driving the ultrasound probe. In this series, the L-electrodes was driven with an imaging pulse by testing different ϕ values. Fig. 6.4 shows an example of the pulses sent to each transducer element.

The test consisted of applying independently a 30 V imaging pulse to the P- and L-electrodes while variating ϕ from 0° to 350° in steps of 10° and registering the acoustic pressure 2 cm away from the transducer element. For comparison, acoustic pressure acquisition was performed by only driving the P-electrodes with 30 V. For each ϕ value tested; three repetitions were performed.

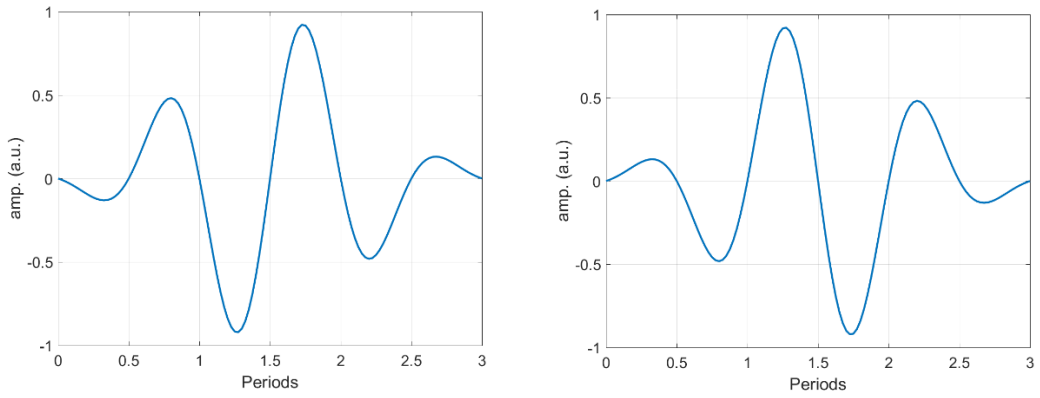

Fig. 6. 4. Electrical imaging pulse with (left) 0° and 180° (right) phase.

Fig. 6.5 shows examples of collected pulses with the hydrophone for a P+L test with 0°, 220°, 270° and with P-only. The shape of pulses and amplitude changes as a function of the phase applied on the L-electrodes. It is worth noting that a phase of 270° produced a larger amplitude compared to the P-only test, but at the same time, a broader pulse was observed, which is not optimal for imaging. The test with 220° produced a more moderate amplitude gain while preserving a short pulse duration. It Is worth noting

the test with P-only showed a small ringing effect (a trail of supplemental pulses), which is usually undesired for imaging as it reduces resolution. This ringing effect was already detected by the DDL during their internal tests.

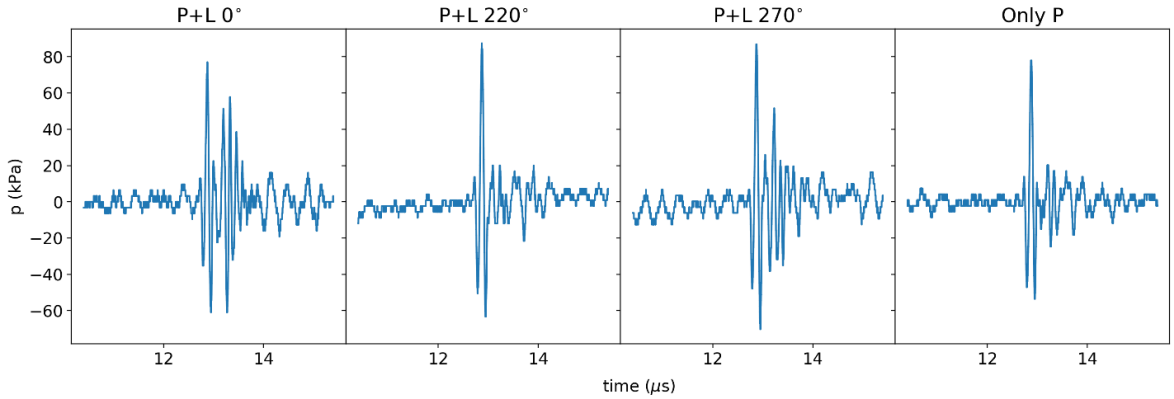

Fig. 6. 5. Hydrophone measurements of test using the biaxial driving mode with 0°, 220° and 270°.

The peak-to-peak pressure amplitude and half-width pulse duration were calculated for all measurements. Fig. 6.6 shows the results per transducer element as a function of the phase applied on the L-electrode. The biaxial effect was clearly observed as the peak-peak amplitude followed a sinusoidal relationship with the phase applied on the L-electrode, and this trend was observed for all transducer elements. Maximum peak amplitude gain for elements B, C and D was, respectively, 16%, 26% and 24%. The respective optimal phases per element were 260°, 300° and 260°, respectively, for an average optimal phase of 273°. The effect of the biaxial mode on the half-pulse transient duration, which is desired to be as narrow as possible, was similar among three transducer elements. This duration increased several times the baseline value for phase values close to 0° and dropped to a duration close to the baseline for phase values around 200°. Overall, these results showed, for the first time, the biaxial effect on imaging transducer in both the resulting amplitude and pulse shape.

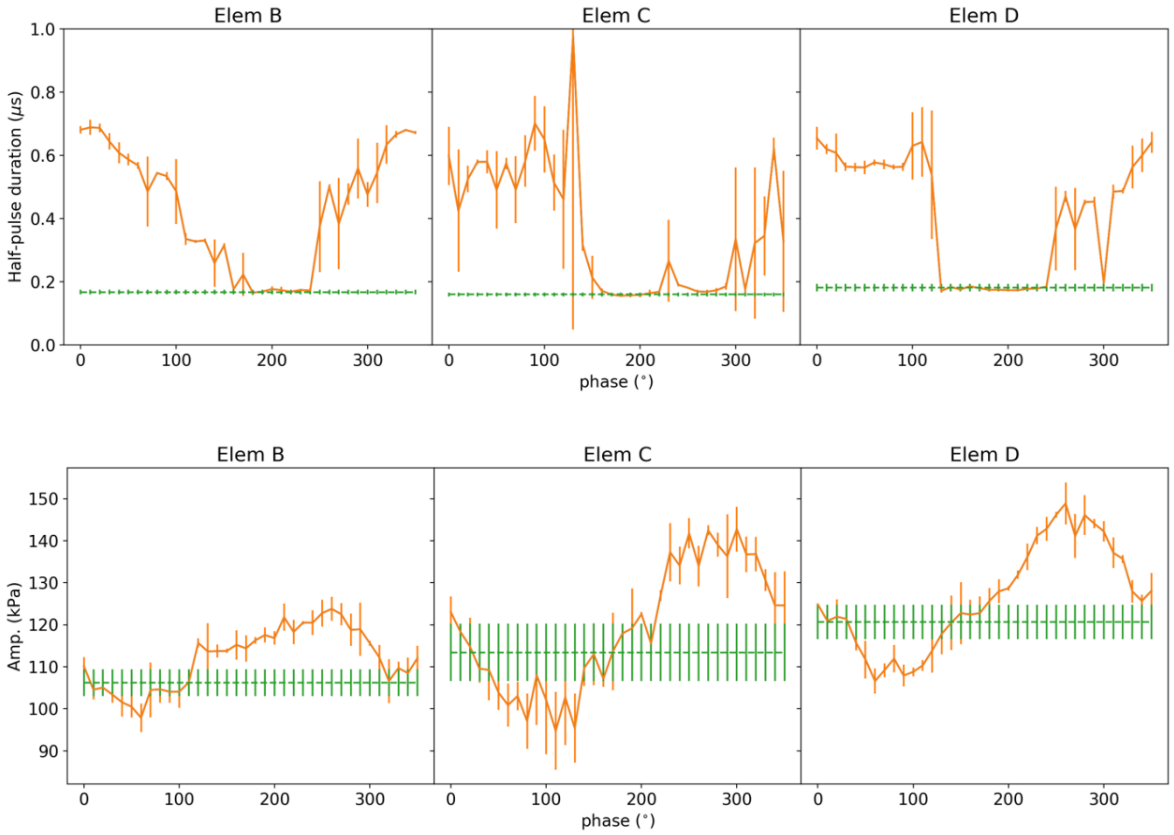

Fig. 6. 6. Measurements of the peak-peak pressure (top) and half-pulse duration (bottom) obtained with the biaxial driving mode (P+L) in function of phase on the L-electrode for each transducer element. The biaxial mode is shown in orange and the reference (only P-mode) in green.

Fig. 6.7 shows measurements of peak-peak amplitude and half-pulse duration when driving the transducer using only the L-electrodes. Driving with only the L-electrodes showed a peak-pressure much smaller than when using the P-electrodes only or when using the P+L mode. The peak pressure oscillated several times as a function of the applied phase (4 “cycles”). The observed half-pulse durations were also significantly wider when compared to the P-only and P+L tests.

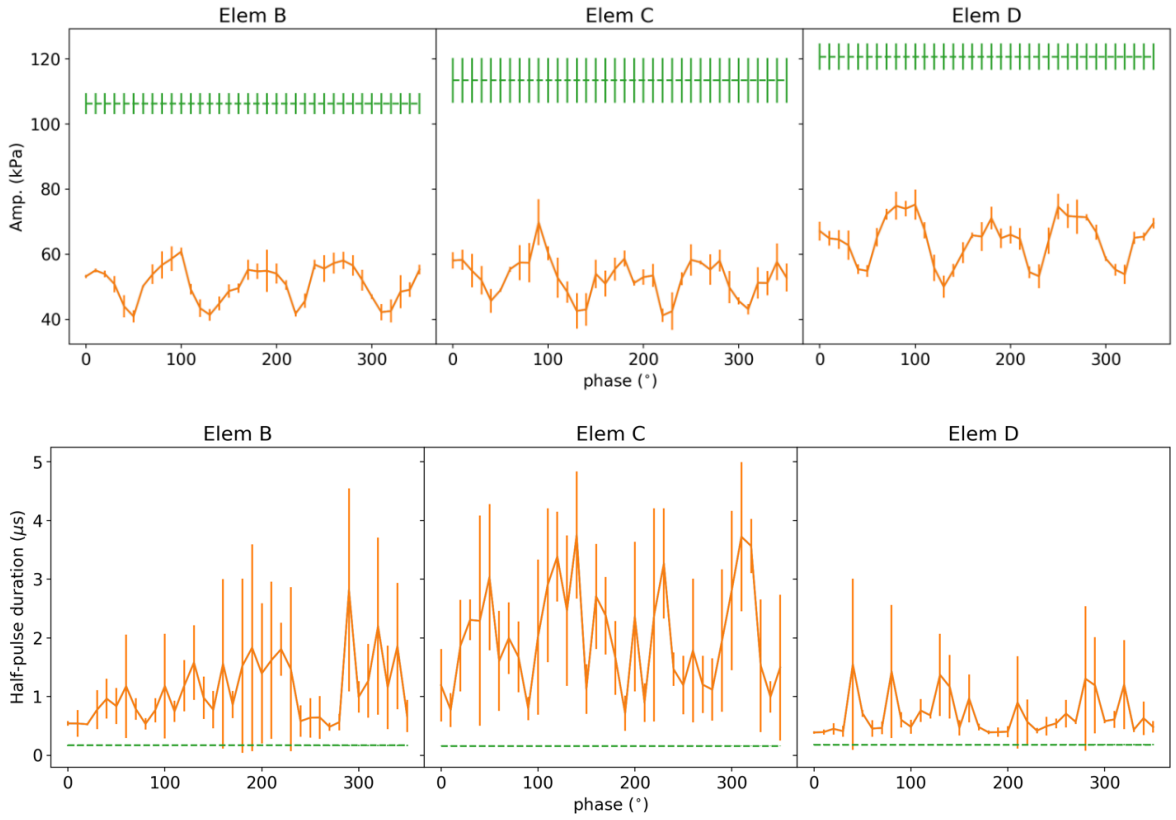

Fig. 6. 7. Measurements of the peak-peak pressure (top) and half-pulse duration (bottom) when driving only the L-electrode in each element. The L-only results are shown in orange and the reference (P-only) in green.

6.1.3.2 Delay variation test

Additional tests suggested that adding a delay (on top of the change of the phase) could also influence the biaxial effect. A set of tests were performed where the phase was varied as before and a delay to the L-electrode signal was added. This delay was expressed in periods (T) of the central frequency, with values from 0 to 3T in steps of 0.5T. It is worth noting that the imaging pulse in fig. 6.4 lasted 3 periods. The hypothesis was that different gains of the P+L mode could be observed by adding fractions of periods in the signal applied in the L-electrodes. Fig. 6.8 and 6.9 show, respectively, the peak-peak amplitude and half-pulse duration of the different tested delays. These tests were performed on element D of the transducer.

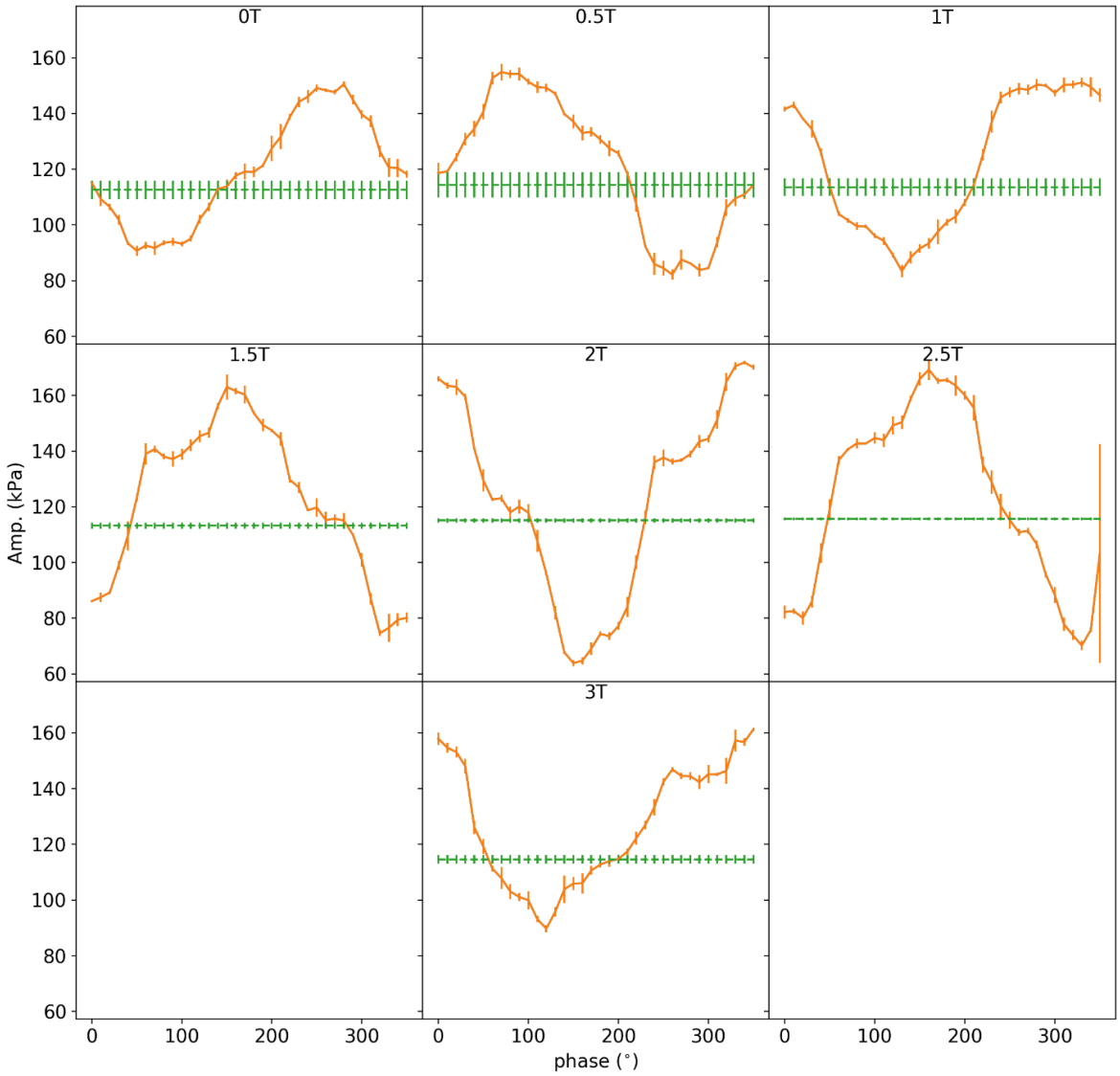

Fig. 6. 8. Measurements of the peak-peak pressure obtained with the biaxial mode (P+L) for the test with supplemental delay in the signal applied in the L-electrodes. The biaxial mode is shown in orange and the reference (P-mode) in green.

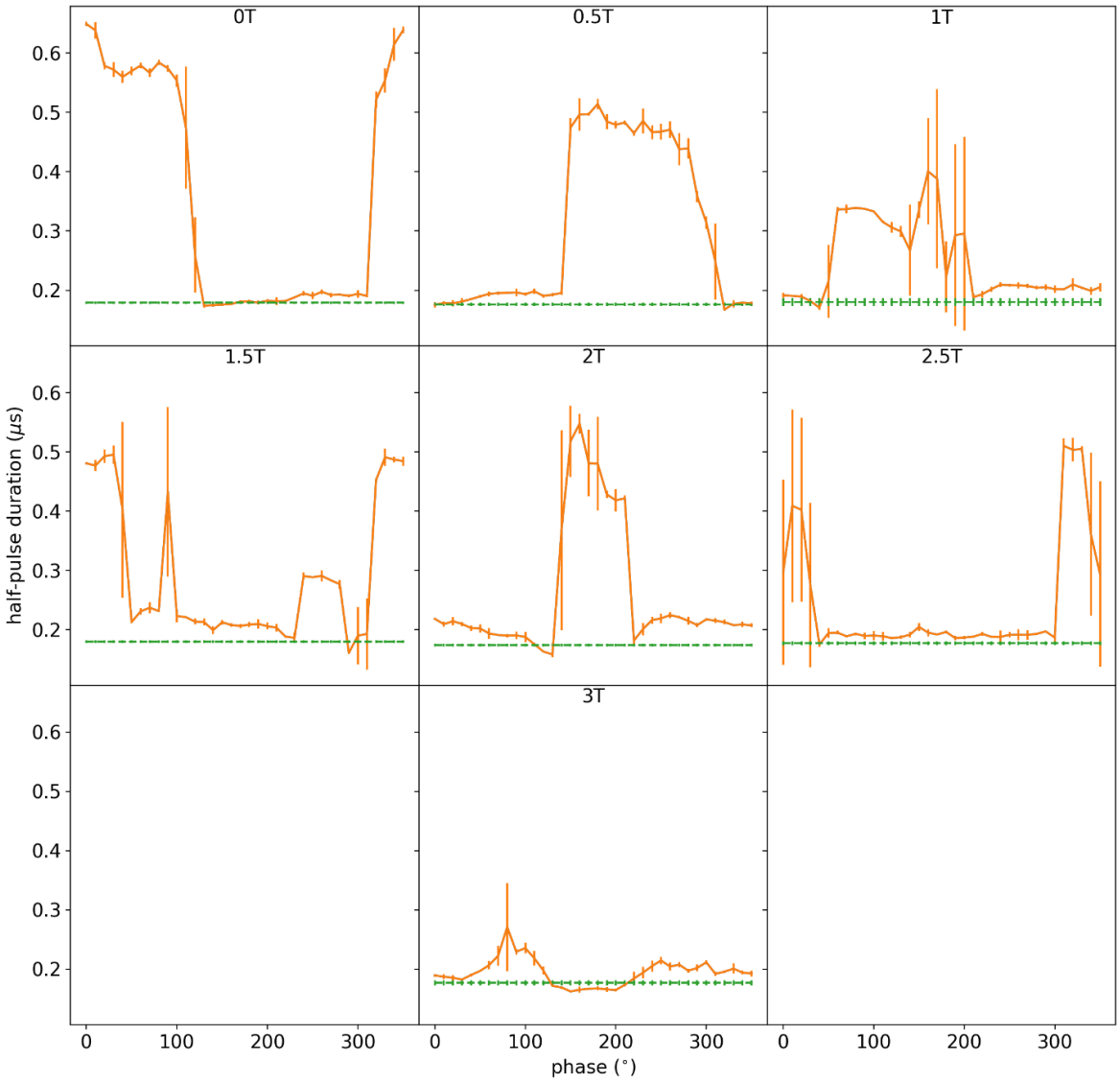

Fig. 6. 9. Measurements of the half-pulse duration obtained with the biaxial mode (P+L) for the test with additional delay in the signal applied in the L-electrodes. The biaxial mode is shown in orange and the reference (P-mode) in green.

Results showed that the biaxial mode was modified by introducing an additional delay. The gain increased with the delay until reaching a maximum for a delay of 2T and a phase of 340°. The gain for this case was 50%, which was double that obtained when using a delay of 0T (24%). The half-pulse duration for this configuration was 0.22 μs, which was 22% larger than the reference duration of 0.18 μs. It is worth noting that the configuration with 2.5T and a phase of 160° produced a gain of 46%, while reducing the half-pulse duration to 0.195 μs, which is only 8% larger than the reference duration.

6.1.4 Imaging tests

As shown in Fig. 6.10, a nylon wire with a diameter of 0.36 mm was used as reflector to test imaging with the biphasic prototype. The wire was placed 2 cm from the imaging transducer, crossing the central region of the transducer elements.

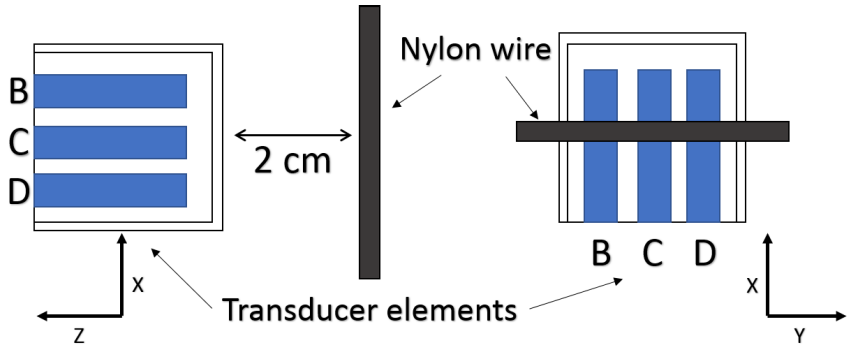

Fig. 6. 10. Reflector setup used for imaging test.

The Verasonics equipment was programmed to create planar B-mode images. Raw RF-data was acquired per electrode, and different tests were performed to evaluate several scenarios of the biaxial driving method applied for imaging. Verasonics vantage system allows the use of a TGC up to 40 dB implemented at 8 equally spaced regions over the recieved acquisition. A TGC of 27 dB was applied in the region of the nylon wire. This gain was kept constant in all tests. B-mode images were reconstructed with the envelope profile of the Hilbert transform of the RF data. Each experiment consisted of the capture of 100 frames, and each experiment was repeated 5 times, for a total of 500 frames.

6.1.4.1 Driving only P-electrodes with reception only at P-electrodes

This test was used as the reference where the transducer was driven and its reading captured in traditional ultrasound imaging configuration. Fig. 6.11 shows an example of an RF echo-pulse observed in the P-electrodes of the elements B, C and D. The nylon-wire reflector is clearly visible at 2 cm. It was also identified noise-related pulses coming from electrical interference in the cables. These noise-related pulses appeared at “random” locations in the captured data pulse. Fig. 6.12 shows three B-mode images (one of the images is formed using the RF data from Fig. 6.11) reconstructed by the planar scan, showing the presence of the nylon and the noise pulses. Table 6.1 (best metrics highlighted) shows the average (±s.d.) peak-peak amplitude, axial resolution (half-pulse width) and signal-to-noise ratio (SNR) for each transducer element. The central transducer (C) showed the best imaging metrics of the reflector. SNR was calculated using the peak amplitude and the noise region between 16 and 18 mm.

Table 6. 1 Only P-electrodes driving & reception measurements

TX element	B	C	D
Peak-peak amplitude (a.u.)	67 (±2.9)	162 (±1)	113(±3.2)
Axial resolution (mm)	4.6(±2.9)	0.7(±1)	3.7(±3.2)
SNR	15.2(±2.7)	23.3(±2.3)	19(±2.9)

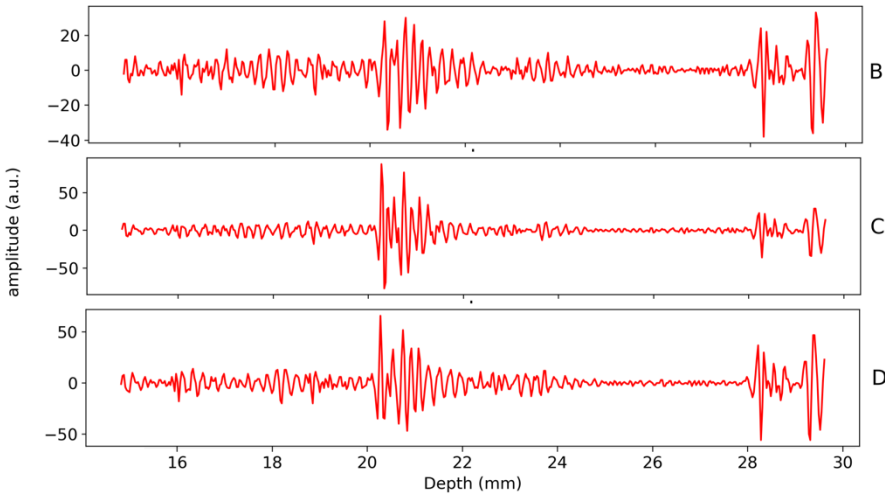

Fig. 6. 11. Echo signal examples for P-electrodes reception on elements B, C and D.

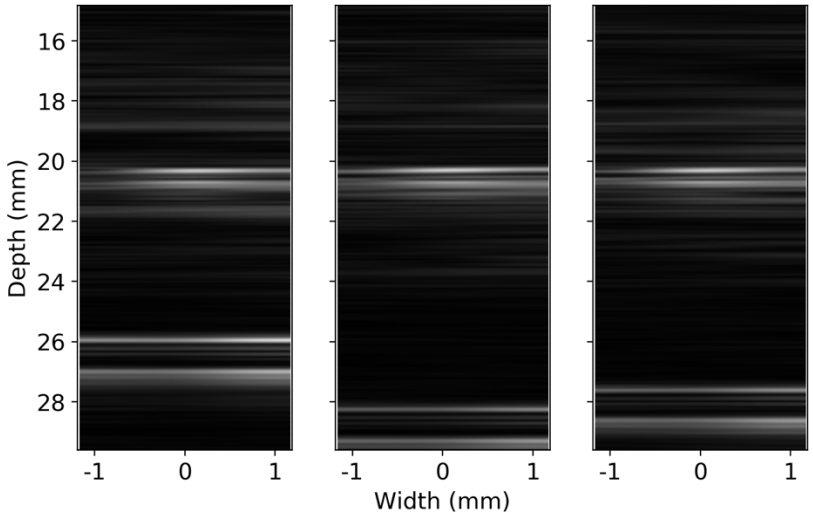

Fig. 6. 12. Three reconstructed frames for the transducer elements with only the P-mode for driving and reception. The nylon wire is observed at 2 cm.

6.1.4.2 Driving P+L electrodes with reception at P+L electrodes

The optimal phase for each element established in section 6.1.3 was programmed for each corresponding L-electrode. Fig. 6.13 shows an example of the RF signals recorded on the P- and L-electrodes of element C. Signals on the L-electrodes showed shapes with a slightly smaller amplitude compared to the signals recorded in the P-electrodes. Direct summation of the P- and L-signals showed an increase in the peak amplitude but also of the noise pulses. The imaging metrics were calculated as in section 6.1.4.1 for the images produced using P, L and P+L RF data. Fig. 6.14 shows an example of reconstructed B-mode images and Table 6.2 (best metrics highlighted) shows the imaging metrics, including all datasets.

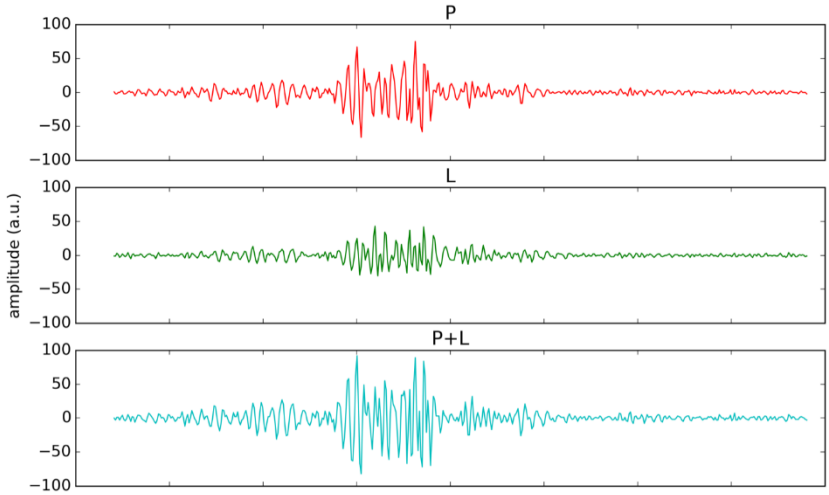

Fig. 6. 13. Echo signal examples for P- and L-electrodes and their sum (elements C).

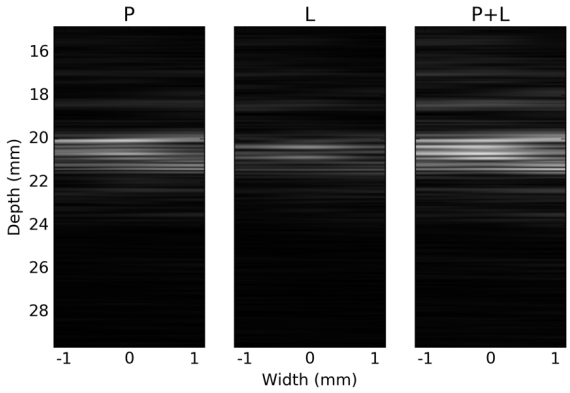

Fig. 6. 14. Three reconstructed frames while driving the transducer elements with the P+L mode and reception at P-, L- and P+L electrodes.

Table 6. 2 P-, L- and P+L driving while P+L reception measurements. Best metrics are highlighted.

Transducer Element	Source data	Peak-peak amplitude (a.u.)	Axial resolution (mm)	SNR (dB)
B	P	141.4(±14.0)	**1.6(±2.2)***	**19.8(±1.4)***
	L	90.9(±8.9)	1.9(±2.3))	16.8(±1.2)
	P+L	**179.4(±18.9)***	2.0(±2.2)	17.4(±1.5)
C	P	206.2(±12.3)	1.4(±1.6)	**23.5(±1.3)***
	L	157.0(±10.2)	**0.8(±0.1)***	23.4(±1.1)
	P+L	**247.6(±18.4)***	1.7(±2.1)	20.8(±1.3)
D	P	121.2(±25.5)	2.7(±2.2)	**19.9(±3.2)***
	L	82.7(±15.9)	**2.4(±2.3)***	19.1(±2.8)
	P+L	**168.8(±53.6)***	3.2(±2.3)	18.3(±3.8)

Compared to images reconstructed with the P-electrodes only, images obtained with the L-electrodes only showed less intense pixels but with comparable SNR and better axial resolution. Data also indicated that a simple sum of P- and L-electrodes RF data (P+L) likewise produced brighter pixels, also with degradation in SNR. When using such sum, a loss of 2.7 dB in element C was observed compared to P-only. A severe degradation in axial resolution was also observed for element C when compared to L-only.

6.1.4.3 Biaxial method on reception

The analysis of RF data indicated that the noise pulses signals on the P-electrodes and L-electrodes were for the most in phase. More importantly, it was also noticed that the pulse shapes of the reflector in the P-electrodes and L-electrodes were out of phase. We hypothesized then that the biaxial effect can also be applicable in reception mode, meaning that there is an optimal re-phase of the signal in the L-electrode that can be added to the signal of the P-electrode to increase image quality. It was anticipated that with this new approach, the noise should be reduced, increasing both the SNR and peak-peak amplitude, while enhancing the axial resolution.

The same metrics of the axial resolution, peak-peak amplitude and SNR were used to establish the optimal phase to be applied to the reception mode of the L-electrode. The SNR metric was clearly the most robust and consistent. A pseudo-code of the method is described as follows:

1. Calculate in *X* the fast Fourier transform (FFT) of L-data:

   X=FFT(L-data)

2. For each phase (ϕ, in radians) from 0 to 2π:

   a. Calculate the *Y* vector (same size as *X*) in the frequency domain that shifts all the frequency spectrum by ϕ with

   $$Y(n) = e^{-j2\varphi\frac{(n-\frac{N}{2})}{N}}$$

   where *n* is the position in the spectrum and *N* is the size of the *X* vector

   b. Calculate vector $Z = X \times Y$ in the frequency domain

   c. Apply inverse fast Fourier transform (FFT^{-1}) to *Z* to calculate L-rotated:

   L-rotated = $FFT^{-1}(Z)$

   d. Add L-rotated to P-data to obtain P+L-rotated

   e. Calculate the SNR of P+L-rotated

3. The optimal ϕ is the one producing the highest SNR.

Fig. 6.15 shows an example plot for one of the acquisitions of the SNR of P+L-rotated signal in function of ϕ. Results in the plot indicated that by applying a rotation on the L-signal the SNR can be improved significantly between 5 and 7 dB. The optimal phase (around 300°) is similar for all elements and very close to the optimal phase established in the tests to increase the pressure (section 6.1.3), which indicated that the physical process in the piezoelectric material to increase the pressure and to improve imaging quality are linked. Table 6.3 (best metrics highlighted) shows the imaging metrics of the P+L-rotated signal among all tests, including the average of the optimal phase at each electrode. SNR and axial resolution showed significant improvement when using the new P+L-rotated signal. Compared to images reconstructed with P-data, on average, the improvement of the SNR ranged from +3.6dB in element D to +5.4 dB in element C. Axial resolution improved from 18% in the element B to 43% in the element C. Fig. 6.16 shows an example of the reconstructed images with P, L, P+L and P+L-rotated RF data. The image reconstructed with P+L-rotated data shows a better-delineated object with less visible noise in the image.

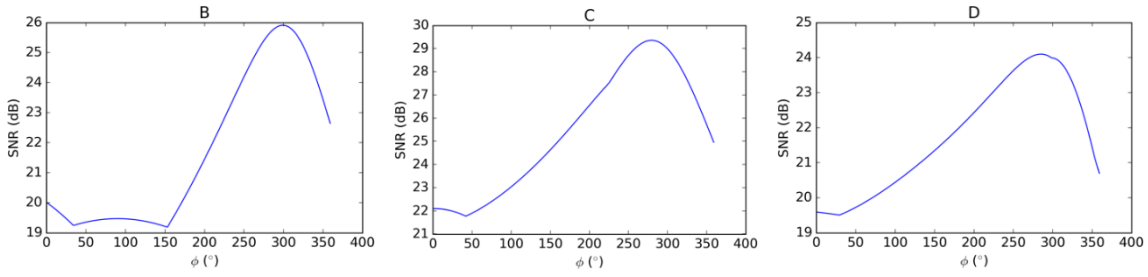

Fig. 6. 15. Example of SNR for the P+L rotated signals as a function of the applied phase ϕ for each element.

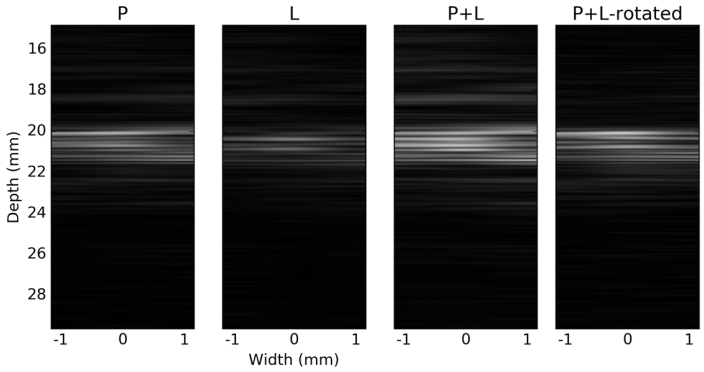

Fig. 6. 16. Reconstructed image example for the P, L, P+L and P+L rotated RF data.

Table 6. 3 P+L rotated measurements. Best metrics compared to Table 6.2 are highlighted.

Transducer Element	Source data	Peak-peak amplitude (a.u.)	Axial resolution (mm)	SNR (dB)	Optimal phase (°)
B	P+L-rotated	165(±11)	**1.3(±1.8)***	**24.4(±1.3)***	295(±12)
C	P+L-rotated	268(±16)	**0.8(±0.11)***	**28.9 (±1.2)***	269(±15)
D	P+L-rotated	143(±32)	**2.1 (±2.1)***	**23.5(±2.5)***	252(±56)

6.1.4.4 Driving P+L electrodes + delay with reception at P+L electrodes

The results of section 6.1.3.2 indicated that adding an additional delay to the rotated field in the L-electrodes can improve the transmitted pulse. We then performed a series of tests adding a 2T delay with a phase of 340° (Table 6.4) and a 2.5T delay with a phase of 160° (Table 6.5). Adding the delay further improved the quality of the imaging metrics. The P+L-rotated test with 2T produced the best improvement in the axial resolution among all tests, showing 1.1 mm, 0.8 mm and 0.8 mm for elements B, C and D, respectively. The P+L-rotated test with 2.5T and the P+L-rotated RF data produced the highest gain in SNR among all tests showing a remarkable average gain of +12.4 dB, +5.8dB and +11.6dB for elements B, C and D, respectively. Also, the tests with delays of 2T and 2.5T produced SNR levels among elements that were the closest among them. Fig. 6.17 shows an example of RF data for 2T. The P+L-rotated shows the larger amplitude while suppressing noise and narrowing the pulse shape. Fig. 6.18 shows a comparison of a reference image with an image obtained with a delay of 2.5T and P+L-rotated. The latter test shows a much more homogenous intensity of the nylon wire among all elements.

Table 6. 4 P+L driving mode with P-, L-, P+L and P+L rotated receiving mode (2T electrode) measurements. Best metrics are highlighted.

Transducer Element	Source data	Peak-peak amplitude (a.u.)	Axial resolution (mm)	SNR (dB)	Optimal phase (°)
B	P	135.8(±15.0)	3.6(±3.0)	21.4(±3.7)	
	L	77.7(±8.9)	3.2(±2.9))	19.1(±2.8)	
	P+L	**182.4(±28.2)***	4.2(±3.2)	20.0(±3.6)	
	P+L-rotated	176.8(±17.7)	**1.1(±1.0)***	**25.8(±3.0)***	282.7(±33.4)
C	P	147.4(±13.9)	2.7(±2.6)	22.5(±3.6))	
	L	103.2(±7.0)	2.4(±1.4)	22.1(±2.6)	
	P+L	180.8(±23.1)	4.4(±2.5)	20.4(±3.4)	
	P+L-rotated	**212.5(±18.5)***	**0.8(±0.6)***	**26.4(±2.9)***	254.4(±41.4)
D	P	202.6(±24.6)	3.2(±3.0)	22.2(±4.4)	
	L	109.5(±15.2)	3.6(±3.0)	21.2(±3.7)	
	P+L	243.3(±56.2)	4.4(±3.2)	20.3(±4.3)	
	P+L-rotated	**255.9(±34.8)***	**0.8(±0.9)***	**27.6(±4.1)***	268.6(±31.5)

Table 6. 5 P+L driving mode with P-, L-, P+L and P+L rotated receiving mode (2.5T L-electrode) measurements. Best metrics are highlighted.

Transducer Element	Source data	Peak-peak amplitude (a.u.)	Axial resolution (mm)	SNR (dB)	Optimal phase (°)
B	P	137.1(±10.9)	4.4(±3.2)	22.1(±2.6)	
	L	81.4(±7.2)	4.3(±3.1)	19.8(±1.9)	
	P+L	**191.6(±21.0)***	4.4(±3.2)	20.8(±2.6)	
	P+L-rotated	109.4(±6.5)	**3.1(±3.1)***	**27.6(±2.0)***	275.8(±20.0)
C	P	147.4(±13.9)	3.8(±3.2)	24.1(±2.6)	
	L	103.2(±7.0)	3.4(±2.7)	24.3(±2.1)	
	P+L	190.6(±17.2)	4.7(±2.8)	21.9(±2.6)	
	P+L-rotated	**242.3(±14.7)***	**0.8(±1.0)***	**29.1(±1.9)***	261.2(±28.7)
D	P	210.7(±18.9)	4.2(±3.3)	24.4(±3.4)	
	L	119.2(±10.6)	4.2(±3.2)	22.5(±2.8)	
	P+L	261.8(±44.6)	4.3(±3.2)	22.3(±3.6)	
	P+L-rotated	**270.6(±18.5)***	**2.0(±2.7)***	**30.6(±2.6)***	267.1(±13.2)

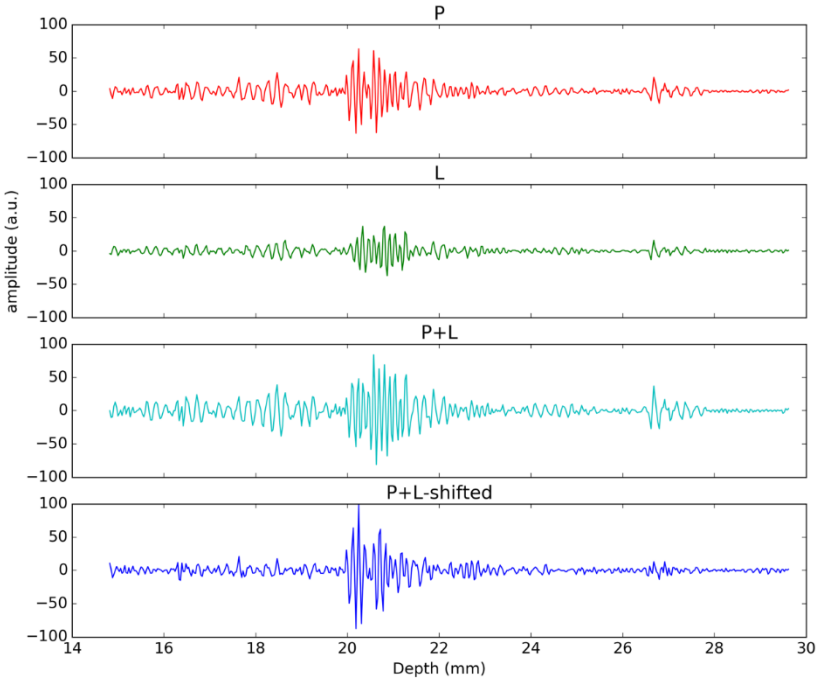

Fig. 6. 17. RF echo signals from P-, L-, P+L and P+L rotated receiving mode with a 2T delay.

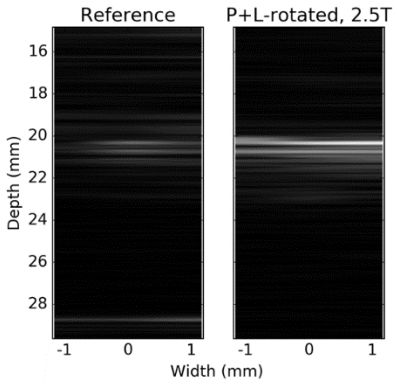

Fig. 6. 18. Comparison of a reconstructed reference (P-only) image with a P+L rotated receiving mode + 2.5T delay reconstructed image.

6.1.4.5 Driving only P-electrodes with a reception at P and L electrodes

A series of tests were done by driving only the P-electrode and receiving in both electrodes and applying the biaxial method on reception. It was hypothesized that the biaxial driving technique applied to reception would increase the image quality of pulses generated using only the P-electrodes. Table 6.6 (best metrics highlighted) shows the imaging metrics of this approach. Compared to the reference (Table 6.1), results confirmed that the biaxial technique on reception, while the driving transmission only with the P-electrode, improved the image quality significantly. Compared to driving both P+L electrodes, the central element of the transducer improved the axial resolution significantly from 0.8 mm to 0.5 mm. The SNR level was lower for the three transducer elements when both P+L electrodes were used for driving (Tables 6.3, 6.4 and 6.3).

Table 6. 6 Only P driving mode with P-, L-, P+L and P+L rotated receiving mode measurements. Best metrics are highlighted.

Transducer Element	Source data	Peak-peak amplitude (a.u.)	Axial resolution (mm)	SNR (dB)	Optimal phase (°)
B	P	61.9(±12.8)	5.9(±3.3)	14.8(±2.7)	
	L	61.9(±12.8)	5.6(±3.2)	14.3(±2.0)	
	P+L	**88.0(±22.3)***	6.7(±3.5)	13.7(±2.8)	
	P+L-rotated	74.0(±14.0)	**2.4(±2.3)***	**19.0(±2.3)***	270.3(±45.8)
C	P	169.4(±17.0)	0.7(±0.8)	23.4(±2.0)	
	L	98.8(±8.2)	0.7(±0.8)	22.8(±1.6)	
	P+L	179.2(±15.4)	1.5(±1.9)	19.6(±1.9)	
	P+L-rotated	**227.5(±18.3)***	**0.5(±0.1)**	**28.8(±1.7)***	267.1(±16.7)
D	P	107.1(±18.7)	4.5(±3.1)	18.3(±3.0)	
	L	60.3(±12.8)	5.3(±3.4)	16.6(±2.9)	
	P+L	**139.9(±35.8)***	5.9(±3.5)	16.1(±3.2)	
	P+L-rotated	110.4(±23.6)	**1.6(±1.9)**	**22.6(±2.8)***	270.0(±40.9)

CHAPTER 7: FINAL DISCUSSION, CONCLUSIONS AND FUTURE WORK

Research conclusions

The feasibility of applying the biaxial driving technique to ferroelectric materials was presented in this investigation with the purpose of increasing the overall acoustic efficiency and the distribution of the acoustic field. This technique consists of applying two dephased orthogonal electrical fields to a piezoelectric actuator. In this research work, biaxial transducers with different ferroelectric elements were simulated with finite element analysis and PZT transducers characterized by using a radiation force method to calculate the acoustic efficiency relative to the phase and power delivered to both modes and a hydrophone system to characterize the acoustic field. Also, we presented the application of the biaxial driving method for imaging, and we discovered how this biaxial method could be applied in reception mode to improve image quality.

For single-element transducers, the results revealed an overall reduction in power consumption in comparison to single-mode due to the fact that a higher efficiency was reached when only a fraction of the power that is used on the propagation electrode needs to be applied to the lateral electrode on biaxial mode transducers. The results indicate that with the proper phase and power, a single element PZT transducer driven biaxially can increase its efficiency up to 10% when compared to a conventional single electric field transducer with the same configuration, however this is not statistically significant for this range of total power applied. It has been shown, for the first time, that controlled steering can be achieved in single-element prismatic shaped ultrasound transducers using the biaxial driving technique. Steering angles up to 30° can be achieved using a single-element and two orthogonal driving signals. It was also demonstrated that a controlled refocusing from 4.5 mm to 9 mm could be achieved with single-element ring transducers by applying the biaxial driving technique. A good agreement was found between finite element simulations and experimental results; the frequency response differed by a maximum of 5.4% and the efficiency by 17.7% on the prismatic transducers; these differences can be attributed to the clamping effect of the sillicone glue used to adhere the piezoceramic material to the ABS casing on the lateral faces. It has also been demonstrated that the addition of the second set of electrodes does not affect the efficiency of ultrasound transducers. It is worth mentioning that the addition of the second set of electrodes into the piezoceramic will require twice the amount of cables and electronics required to drive the transducer element, which will have to be considered in the production of biaxial transducer phased-arrays.

The first ultrasound imaging device based on the biaxial driving technique was fabricated and

characterized. A sinusoidal response was observed on the acoustic pressure was observed, but the gain in terms of direct energy efficiency was short of what has been observed for narrow-band devices. Nevertheless, the biaxial method showed a relevant improvement on the signal to noise ratio and axial resolution for image reconstruction by combining the biaxial effect in transmission and a numerically-based biaxial method in reception.

In summary, the results in this work clearly indicate that the biaxial method will provide significant new opportunities to design a new generation of ultrasound transducers. The potential gain in ultrasound focusing and processing in reception using the biaxial method will be of great value for multiple applications, especially in medical therapy and imaging.

Future work

This work has shown the first study of the biaxial driving applications, covering the steering, refocusing and efficiency properties for single-elements ultrasound transducers and the advantages into a first prototype of an imaging probe. Regarding the efficiency response, results did not show a statistically significance for biaxial driving, however, the biaxial driving relies into the reduction of the coercive field and hence into the hysteresis response of a ferroelectric material, which means that there is a study opportunity to increase more the efficiency during high power transducer applications. Also, the use of a balanced voltage and a reduced area size of the lateral electrodes might help to improve the efficiency response and have a better control to the steering capability.

It was not include within this first study, but an analysis of the electric field vectors and its possible relation with the steering angles and vibration modes would be a feasible study, specially to reduce characterization time.

The capability of the biaxial driving to produce a steering response is one of the most interesting properties developed within this research project and hence the application of a 3rd set of electrodes within a prismatic shaped transducer to produce a three dimensional acoustic beam steering is a project that needs to be developed as soon as possible to cover the limitatios of most linear and phase arrays. In addition, the experimental validation of this work was aimed to low frequencies applications within the range of 150 kHz to 500 kHz for the narrowband transducers, so higher frequencies ferroelectric materials either by reducin the thickness or testing the harmonics would be a huge advantage for the future.

The ring shaped transducers showed a refocusing property that is only possible with phased arrays or physically moving the transducer. This refocusing property is highly desired for BBB opening experiments

and neuromodulation and neurostimulation applications. The development of an array of ring transducers to reduce the focal spot at lower frequencies is one applciation that needs to be considered.

Finally, the first prototype of an imaging transducer showed some promising applications to reduce the SNR of the signal, so an ultrasound probe with a higher number of elements would be a feasible option to keep developing the biaxial driving in imaging.

CONTRIBUTIONS.

The results obtained for the steering effect of single-element transducers with biaxial driving were accepted to be published in a scientific journal :

- Delgado, S., Curiel, L. & Pichardo, S. Steering Single-Element Lead Zirconate Titanate Ultrasound Transducers using Biaxial Driving. *Ultrasonics* (2021). Volume 110, February 2021. 106241. Published online https://doi.org/10.1016/j.ultras.2020.106241

In addition to the publication, a patent application was submitted on January 2020 for the steering technology,

- Samuel Pichardo, Laura Curiel, Sagid Delgado. SYSTEMS AND METHODS FOR CONTROLLING DIRECTIONAL PROPERTIES OF ULTRASOUND TRANSDUCERS VIA BIPHASIC ACTUATION. Provisional patent application, PCT # 62959616. Submitted Jan 10, 2020.

A second patent application covering the improvement for the image quality of ultrasound transducers with the biaxial driving in transmission and reception is under preparation,

- Samuel Pichardo, Laura Curiel, Sagid Delgado, Oleg Rubel. Method to improve quality of ultrasound imaging using rotational electric field (biphasic) in ferroelectric materials and devices. Submission Pending.

Several international conference papers were accepted to be published describing the efficiency and steering advantages of driving ultrasound transducers with the biaxial technique,

- Delgado, S., Curiel, L. & Pichardo, S. Steering Single-Element Ferroelectric Materials Using Biaxial Driving. *2020 IEEE International Ultrasonics Symposium* (2020).
- Delgado, S., Curiel, L. & Pichardo, S. Application of the Biaxial Driving Method To Focus Ultrasound Using Only Two Electric Signals. *2020 IEEE International Ultrasonics Symposium* (2020).
- Delgado, S., Curiel, L. & Pichardo, S. Improvement of Focusing in 2D phased Arrays Using the Biaxial Driving Method: A Numerical Study. *2020 IEEE International Ultrasonics Symposium* (2020).
- Delgado, S., Curiel, L., Rubel, O., Da Silva, G. & Pichardo, S. Optimal phase on biaxial driven transducers based only on electrical power measurements. *2017 IEEE International Ultrasonics Symposium (2017)*.

Finally, the significant discoveries identified in this work (especially in terms of intellectual property) helped to create the company Novus Tx Inc. (www.novustx-devices.com) , in which I am a founding member.

Appendix A. Material properties

Piezoelectric material properties

Stiffness matrix at constant E $(10^{10}\mathrm{N}\cdot\mathrm{m}^{-2})$	PZT	$BaTiO_3$	$LiNbO_3$
C_{11}^E	15.6	17.2	2.03
C_{12}^E	8.9	7.5	0.57
C_{13}^E	8.8	8.5	0.75
C_{14}^E	0	0	0.09
C_{33}^E	13.2	17.4	2.42
C_{44}^E	3.1	4.6	0.6
C_{66}^E	3.4	4.8	0.73

Piezoelectric constant $(\mathrm{C}\cdot\mathrm{m}^{-2})$	PZT	$BaTiO_3$	$LiNbO_3$
e_{15}	14.3	10.8	3.8
e_{22}	0	0	2.4
e_{31}	-4.9	-0.7	0.2
e_{33}	18.5	15.7	1.3

Dielectric matrix at constant strain	PZT	$BaTiO_3$	$LiNbO_3$
ε_{11}^{ξ}	960	960	44.3
ε_{33}^{ξ}	870	875	27.9

	PZT	$BaTiO_3$	$LiNbO_3$
Density ($Kg \cdot cm^{-3}$)	7800	5600	4650

Acoustic material properties

	Water	Air
Density ($Kg \cdot cm^{-3}$)	1000	1.24
Speed of sound ($m \cdot s^{-2}$)	1500	343

Structural material properties

	ABS-plastic	Silicone	Cork
Density ($Kg \cdot cm^{-3}$)	1040	930	240
Youngs modulus (MPa)	2390	2.068	11
Poisson ratio	0.399	0.4995	0.2

Appendix B. Materials IEEE to ANSYS format

IEEE [e]

$$\begin{matrix} x \\ y \\ z \\ yz \\ xz \\ xy \end{matrix}\begin{bmatrix} e_{11} & e_{12} & e_{13} \\ e_{21} & e_{22} & e_{23} \\ e_{31} & e_{32} & e_{33} \\ e_{41} & e_{42} & e_{43} \\ e_{51} & e_{52} & e_{53} \\ e_{61} & e_{62} & e_{63} \end{bmatrix}$$

ANSYS [e]

$$\begin{matrix} x \\ y \\ z \\ xy \\ yz \\ xz \end{matrix}\begin{bmatrix} e_{11} & e_{12} & e_{13} \\ e_{21} & e_{22} & e_{23} \\ e_{31} & e_{32} & e_{33} \\ e_{61} & e_{62} & e_{63} \\ e_{41} & e_{42} & e_{43} \\ e_{51} & e_{52} & e_{53} \end{bmatrix}$$

IEEE [e]

$$\begin{matrix} x \\ y \\ z \\ yz \\ xz \\ xy \end{matrix}\begin{bmatrix} d_{11} & d_{12} & d_{13} \\ d_{21} & d_{22} & d_{23} \\ d_{31} & d_{32} & d_{33} \\ d_{41} & d_{42} & d_{43} \\ d_{51} & d_{52} & d_{53} \\ d_{61} & d_{62} & d_{63} \end{bmatrix}$$

ANSYS [e]

$$\begin{matrix} x \\ y \\ z \\ xy \\ yz \\ xz \end{matrix}\begin{bmatrix} d_{11} & d_{12} & d_{13} \\ d_{21} & d_{22} & d_{23} \\ d_{31} & d_{32} & d_{33} \\ d_{61} & d_{62} & d_{63} \\ d_{41} & d_{42} & d_{43} \\ d_{51} & d_{52} & d_{53} \end{bmatrix}$$

for the elastic stiffness (c) matrix

IEEE [c]

$$\begin{matrix} x & y & z & yz & xz & xy \end{matrix}$$
$$\begin{bmatrix} c_{11} & c_{12} & c_{13} & c_{14} & c_{15} & c_{16} \\ c_{21} & c_{22} & c_{23} & c_{24} & c_{25} & c_{26} \\ c_{31} & c_{32} & c_{33} & c_{34} & c_{35} & c_{36} \\ c_{41} & c_{42} & c_{43} & c_{44} & c_{45} & c_{46} \\ c_{51} & c_{52} & c_{53} & c_{54} & c_{55} & c_{56} \\ c_{61} & c_{62} & c_{63} & c_{64} & c_{65} & c_{66} \end{bmatrix}\begin{matrix} x \\ y \\ z \\ yz \\ xz \\ xy \end{matrix}$$

ANSYS [c]

$$\begin{matrix} x & y & z & yz & xz & xy \end{matrix}$$
$$\begin{bmatrix} c_{11} & c_{12} & c_{13} & c_{16} & c_{14} & c_{15} \\ c_{21} & c_{22} & c_{23} & c_{26} & c_{24} & c_{25} \\ c_{31} & c_{32} & c_{33} & c_{36} & c_{34} & c_{35} \\ c_{41} & c_{42} & c_{43} & c_{66} & c_{46} & c_{56} \\ c_{51} & c_{52} & c_{53} & c_{64} & c_{44} & c_{54} \\ c_{61} & c_{62} & c_{63} & c_{65} & c_{45} & c_{55} \end{bmatrix}\begin{matrix} x \\ y \\ z \\ xy \\ yz \\ xz \end{matrix}$$

And finally, for the anisotropic elastic compliance (S) matrix

IEEE [S]

$$\begin{bmatrix} S_{11} & S_{12} & S_{13} & 0 & 0 & 0 \\ S_{21} & S_{22} & S_{23} & 0 & 0 & 0 \\ S_{31} & S_{32} & S_{33} & 0 & 0 & 0 \\ 0 & 0 & 0 & S_{44} & 0 & 0 \\ 0 & 0 & 0 & 0 & S_{55} & 0 \\ 0 & 0 & 0 & 0 & 0 & S_{66} \end{bmatrix}$$

ANSYS [S]

$$\begin{bmatrix} S_{11} & S_{12} & S_{13} & 0 & 0 & 0 \\ S_{21} & S_{22} & S_{23} & 0 & 0 & 0 \\ S_{31} & S_{32} & S_{33} & 0 & 0 & 0 \\ 0 & 0 & 0 & S_{66} & 0 & 0 \\ 0 & 0 & 0 & 0 & S_{44} & 0 \\ 0 & 0 & 0 & 0 & 0 & S_{55} \end{bmatrix}$$

REFERENCES

[1] F. Weyland, M. Acosta, J. Koruza, P. Breckner, J. Rödel, and N. Novak, "Criticality: Concept to Enhance the Piezoelectric and Electrocaloric Properties of Ferroelectrics," *Adv. Funct. Mater.*, vol. 26, no. 40, pp. 7326–7333, 2016.

[2] A. Carovac, F. Smajlovic, and D. Junuzovic, "Application of ultrasound in medicine.," *Acta Inform. Med.*, vol. 19, no. 3, pp. 168–71, 2011.

[3] K. H. Clare M. C. Tempany, Elizabeth A. Stewart, Nathan McDannold, Bradley J. Quade, Ferenc A. Jolesz, "MR Imaging–guided Focused Ultrasound Surgery of Uterine Leiomyomas: A Feasibility Study," *Radiology*, vol. 226, no. 3. pp. 897–905, 2003.

[4] M. Ghorbani, O. Oral, S. Ekici, D. Gozuacik, and A. Kosar, "Review on Lithotripsy and Cavitation in Urinary Stone Therapy," *IEEE Rev. Biomed. Eng.*, vol. 9, pp. 264–283, 2016.

[5] D. Waller, J. Chen, and T. R. Gururaja, "Requirements of piezoelectric materials for medical ultrasound transducers," *IEEE Int. Symp. Appl. Ferroelectr.*, vol. 2, pp. 565–568, 1996.

[6] T. Uchida and T. Kikuchi, "Effect of heat generation of ultrasound transducer on ultrasonic power measured by calorimetric method," *Jpn. J. Appl. Phys.*, vol. 52, no. 7 PART 2, 2013.

[7] S. W. Zhou and C. A. Rogers, "Heat generation, temperature, and thermal stress of structurally integrated piezo-actuators," *J. Intell. Mater. Syst. Struct.*, vol. 6, no. 3, 1995.

[8] M. S. Senousy, R. K. N. D. Rajapakse, D. Mumford, and M. S. Gadala, "Self-heat generation in piezoelectric stack actuators used in fuel injectors," *Smart Mater. Struct.*, vol. 18, no. 4, 2009.

[9] P. Ronkanen, P. Kallio, M. Vilkko, and H. N. Koivo, "Self heating of piezoelectric actuators: Measurement and compensation," in *Proceedings of the 2004 International Symposium on Micro-NanoMechatronics and Human Science, MHS2004; The Fourth Symposium "Micro-NanoMechatronics for and Information-Based Society" The 21st Century*, 2004.

[10] R. W. Martin, S. Vaezy, A. Proctor, T. Myntti, J. B. J. Lee, and L. A. Crum, "Water-cooled, high-intensity ultrasound surgical applicators with frequency tracking," *IEEE Trans. Ultrason. Ferroelectr. Freq. Control*, vol. 50, no. 10, 2003.

[11] A. C. H. Tan and F. S. Hover, "On the influence of transducer heating in underwater ultrasonic thrusters," in *20th International Congress on Acoustics 2010, ICA 2010 - Incorporating Proceedings of the 2010 Annual Conference of the Australian Acoustical Society*, 2010, vol. 1.

[12] O. Saunders, S. Clift, and F. Duck, "Ultrasound transducer self heating: development of 3-D finite-element models," *J. Phys. Conf. Ser.*, vol. 1, 2004.

[13] J. Calvert and F. Duck, "Self-heating of Diagnostic Ultrasound Transducers in Air and in Contact with Tissue Mimics," *Ultrasound*, vol. 14, no. 2, 2006.

[14] IEC, "IEC 60601-2-37:2007 - Medical electrical equipment - Part 2-37: Particular requirements for the basic safety and essential performance of ultrasonic medical diagnostic and monitoring equipment." 2007.

[15] C. Doody, H. Starritt, and F. Duck, "Prediction of the temperature rise at the surface of clinical ultrasound transducers," *Ultrasound*, vol. 11, no. 3, 2003.

[16] D. Clarck, B. Scheirer, and R. Manning, "Curved ultrasonic HIFU transducer with air cooling passageway," 2010.

[17] R. T. Held, V. Zderic, T. N. Nguyen, and S. Vaezy, "Annular Phased-Array High-Intensity Focused Ultrasound Device for Image-Guided Therapy of Uterine Fibroids," *IEEE Trans. Ultrason. Ferroelectr. Freq. Control*, vol. 53, no. 2, pp. 335–348, 2006.

[18] T. Uchida *et al.*, "Five years experience of transrectal high-intensity focused ultrasound using the Sonablate device in the treatment of localized prostate cancer," *Int. J. Urol.*, vol. 13, no. 3, pp. 228–233, Mar. 2006.

[19] H. Azhari, *Basics of Biomedical Ultrasound for Engineers*. 2010.

[20] R. S. C. Cobbold, "Foundations of Biomedical Ultrasound," *Oxford Univ. Press*, 2007.

[21] D. B. Ma and Y. Wang, "Power efficient ultrasound imaging diagnosis system using adaptive data prediction scheme," in *Proceedings of 2017 IEEE Far East NDT New Technology and Application Forum, FENDT 2017*, 2018.

[22] P. Wang, Y. Li, and Y. Lu, "Enhanced piezoelectric properties of (Ba0.85Ca0.15)(Ti0.9Zr0.1)O3 lead-free ceramics by optimizing calcination and sintering temperature," *J. Eur. Ceram. Soc.*, vol. 31, no. 11, pp. 2005–2012, 2011.

[23] J. H. Ahn and J. H. Koh, "Enhanced piezoelectric properties of (Bi,Sc)O3-(Pb,Ti)O3ceramics by optimized calcination process," *J. Alloys Compd.*, vol. 689, pp. 138–144, 2016.

[24] H. Zhao, Y. Hou, X. Yu, M. Zheng, and M. Zhu, “Construction of high T c BiScO 3 -BiFeO 3 -PbTiO 3 and its enhanced piezoelectric properties by sintering in oxygen atmosphere,” *J. Appl. Phys.*, vol. 124, no. 19, 2018.

[25] C. M. Wang, J. F. Wang, and Z. G. Gai, “Enhancement of dielectric and piezoelectric properties of M0.5Bi4.5Ti4O15 (M = Na, K, Li) ceramics by Ce doping,” *Scr. Mater.*, vol. 57, no. 9, pp. 789–792, 2007.

[26] A. I. Ali, C. W. Ahn, and Y. S. Kim, “Enhancement of piezoelectric and ferroelectric properties of BaTiO 3 ceramics by aluminum doping,” *Ceram. Int.*, vol. 39, no. 6, pp. 6623–6629, 2013.

[27] T. Yokoyama, Y. Iwazaki, Y. Onda, T. Nishihara, Y. Sasajima, and M. Ueda, “Effect of Mg and Zr co-doping on piezoelectric AlN thin films for bulk acoustic wave resonators,” *IEEE Trans. Ultrason. Ferroelectr. Freq. Control*, vol. 61, no. 8, pp. 1322–1328, 2014.

[28] H. Liu *et al.*, “Effect of MnO2 doping on piezoelectric, dielectric and ferroelectric properties of PNN–PZT ceramics,” *Ceram. Int.*, vol. 41, no. 9, pp. 11359–11364, 2015.

[29] J. Cole, S. J. Ahmed, L. Curiel, S. Pichardo, and O. Rubel, “Marble game with optimal ferroelectric switching,” *J. Phys. Condens. Matter*, vol. 26, no. 13, 2014.

[30] S. Pichardo, R. R. C. Silva, O. Rubel, and L. Curiel, “Efficient driving of piezoelectric transducers using a biaxial driving technique,” *PLoS One*, vol. 10, no. 9, pp. 1–10, 2015.

[31] C. H. Hong *et al.*, “Lead-free piezoceramics – Where to move on?,” *J. Mater.*, vol. 2, no. 1, pp. 1–24, 2016.

[32] F. Rubio-Marcos, R. López-Juárez, R. E. Rojas-Hernandez, A. Del Campo, N. Razo-Pérez, and J. F. Fernandez, “Lead-Free Piezoceramics: Revealing the Role of the Rhombohedral-Tetragonal Phase Coexistence in Enhancement of the Piezoelectric Properties,” *ACS Appl. Mater. Interfaces*, vol. 7, no. 41, pp. 23080–23088, 2015.

[33] Y. Chen, K. Mei, C. M. Wong, D. Lin, H. L. W. Chan, and J. Dai, “Ultrasonic transducer fabricated using lead-free BFO-BTO+Mn piezoelectric 1-3 composite,” *Actuators*, vol. 4, no. 2, pp. 127–134, 2015.

[34] L. Burianova, M. Pustka, and J. Nosek, “High-frequency extensional vibrations of piezoelectric ceramic bars polarized in the longitudinal direction,” *IEEE Trans. Ultrason. Ferroelectr. Freq. Control*, vol. 56, no. 1, pp. 175–181, 2009.

[35] S. Committee, I. Ultrasonics, and F. C. Society, “An American National Standard: IEEE Standard on Piezoelectricity,” *IEEE Trans. Sonics Ultrason.*, vol. 31, no. 2, pp. 8–10, 1984.

[36] S. Delgado, L. Curiel, O. Rubel, G. Da Silva, and S. Pichardo, “Optimal phase on biaxial driven transducers based only on electrical power measurements,” *IEEE Int. Ultrason. Symp. IUS*, pp. 6–9, 2017.

[37] M. I. Gutierrez, “Modelado del calentamiento de radiacion acustica generada por equipos de fisioterapia ultrasonica, validacion experimental en medios homogeneos y diseño de la instrumentacion,” Centro de Investigacion y de Estudios Avanzados del Instituto Politecnico Nacional, 2011.

[38] S. A. Delgado, “Dispositivo portátil para la excitación de transductores HIFU monoelemento y monitoreo de su acoplamiento mediante la medición de la relación de onda estacionaria,” Centro de Investigacion y de Estudios Avanzados del Instituto Politecnico Nacional, 2015.

[39] P. Laugier and G. Haïat, *Bone quantitative ultrasound*. 2011.

[40] J. L. Teja, “Diseño de un Dispositivo para Hemostasia Acústica con Ultrasonido Focalizado de Alta Intensidad mediante Simulaciones FEM,” 2013.

[41] P. Hoskins, K. Martin, and A. Thrush, *Diagnostic Ultrasound Physics and Equipment*, 2nd editio. Cambridge University Press, 2010.

[42] L. Vanco and A. D. Pierce, “Acoustics: An Introduction to Its Physical Principles and Applications,” *Comput. Music J.*, 1998.

[43] N. M. Tole, “Basic physics of ultrasonographic imaging,” *Diagnostic Imaging Lab. Technol. Essent. Heal. Technol. Heal. Technol. Pharm. WORLD Heal. Organ. Geneva*, 2005.

[44] *Crystallography and the World of Symmetry*. 2008.

[45] J. Curie and P. Curie, “Développement par compression de l’électricité polaire dans les cristaux hémièdres à faces inclinées,” *Bull. la Société minéralogique Fr.*, 1880.

[46] G. Lippmann, “Principe de la conservation de l’électricité, ou second principe de la théorie des phénomènes électriques,” *J. Phys. Théorique Appliquée*, 1881.

[47] B. P. O. Inc, “Intro to piezoelectric transducer crystals.” [Online]. Available: https://www.bostonpiezooptics.com/transducer-crystals.

[48] *Piezoelectric Transducers for Vibration Control and Damping*. 2006.

[49] H. F. Tiersten, *Linear Piezoelectric Plate Vibrations*. 1969.

[50] E. Engineers, "IEEE Standard Definitions of Primary Ferroelectric Terms," *East*, vol. 986, 1986.

[51] H. JAFFE, "Piezoelectric Ceramics," *J. Am. Ceram. Soc.*, 1958.

[52] K. M. Rabe, C. H. Ahn, and J.-M. Triscone, *Physics of Ferroelectrics - A Modern Perspective*. 2007.

[53] J. Guyonnet, *Ferroelectric Domain Walls*. 2014.

[54] L. APC International, "Piezoelectric ceramics principles and applications." [Online]. Available: https://www.americanpiezo.com/.

[55] B. Jaffe, R. S. Roth, and S. Marzullo, "Piezoelectric properties of Lead zirconate-Lead titanate solid-solution ceramics [8]," *Journal of Applied Physics*. 1954.

[56] C. R. Hill, J. C. Bamber, and G. R. Ter Haar, *Physical Principles of Medical Ultrasonics*. 2005.

[57] A. Safari and E. K. Akdoğan, *Piezoelectric and acoustic materials for transducer applications*. 2008.

[58] B. T. Eovino, "Design and Analysis of a PVDF Acoustic Transducer Towards an Imager for Mobile Underwater Sensor Networks," p. 44, 2015.

[59] T. H. Kim and A. C. Arias, "Characterization and applications of piezoelectric polymers."

[60] T. R. Gururaja, W. a. Schulze, L. E. Cross, R. E. Newnham, B. a. Auld, and Y. J. Wang, "Piezoelectric composite materials for ultrasonic transducer applications. Part I: Resonant modes of vibration of PZT rod-polymer composites," *IEEE Trans. Sonics Ultrason.*, vol. 32, no. 4, pp. 481–498, 1985.

[61] W. A. Smith, "Role of piezocomposites in ultrasonic transducers," *Ultrason. Symp. Proc.*, vol. 2, pp. 755–766, 1989.

[62] Ö. Oralkan *et al.*, "Capacitive micromachined ultrasonic transducers: Next-generation arrays for acoustic imaging?," *IEEE Trans. Ultrason. Ferroelectr. Freq. Control*, vol. 49, no. 11, pp. 1596–1610, 2002.

[63] S. H. Wong, M. Kupnik, R. D. Watkins, K. Butts-Pauly, and B. T. Khuri-Yakub, "Capacitive micromachined ultrasonic transducers for therapeutic ultrasound applications," *IEEE Trans. Biomed. Eng.*, vol. 57, no. 1, pp. 114–123, 2010.

[64] S. T. Hansen, B. J. Mossawir, A. S. Ergun, F. L. Degertekin, and B. T. Khuri-Yakub, "Air-coupled nondestructive evaluation using micromachined ultrasonic transducers," in *Proceedings of the IEEE Ultrasonics Symposium*, 1999, vol. 2.

[65] S. T. Hansen, A. Sanli Ergun, and B. T. Khuri-Yakub, "Improved modeling and design of microphones using radio frequency detection with capacitive micromachined ultrasonic transducers," in *Proceedings of the IEEE Ultrasonics Symposium*, 2001, vol. 2.

[66] H. Jagannathan, G. G. Yaralioglu, A. S. Ergun, F. L. Degertekin, and B. T. Khuri-Yakub, "Micro-fluidic channels with integrated ultrasonic transducers," *Proc. IEEE Ultrason. Symp.*, vol. 2, 2001.

[67] M. H. Repacholi, M. Gandolfo, A. Rindi, and K. TACHIBANA, *Ultrasound: Medical Applications, Biological Effects, and Hazard Potential*. 1987.

[68] H. F. Stewart, "Essentials of Medical Ultrasound. A Practical Introduction to the Principles, Techniques and Biomedical Applications," in *Essentials of Medical Ultrasound. A Practical Introduction to the Principles, Techniques and Biomedical Applications*, 1st ed., M. H. Repacholi and D. A. Benwell, Eds. HUMANA Press, 1982, pp. 77–111.

[69] A. Papoulis, S. U. Pillai, and S. U. Papoulis, Athanasios; Pillai, "Probability , Random Variables , and Stochastic Processes - Solutions Manual," *McGraw Hill*, 2002.

[70] A. Goldstein, "Quality Assurance in Diagnostic Ultrasound," in *Essentials of Medical Ultrasound. A practical Introduction to the principles, Techniques, and Biomedical Applications*, The HUMANA Press Inc., 1982.

[71] M. S. Patterson and F. S. Foster, "The improvement and quantitative assessment of B-Mode images produced by an annular array/cone hybrid," *Ultrason. Imaging*, vol. 5, no. 3, 1983.

[72] K. K. Shung, *Diagnostic ultrasound. Imaging and blood flow measurements*, 1st ed. CRC Press, 2006.

[73] R. H. Silverman, "High-resolution ultrasound imaging of the eye - A review," *Clinical and Experimental Ophthalmology*, vol. 37, no. 1. 2009.

[74] A. Webb, *Introduction to biomedical imaging*, 1st editio. John Wiley & Sons, 2003.

[75] G. ter Haar, "Therapeutic applications of ultrasound," *Prog. Biophys. Mol. Biol.*, vol. 93, no. 1–3, pp. 111–129, 2007.

[76] W. D. O'Brien, "Ultrasound-biophysics mechanisms," *Progress in Biophysics and Molecular Biology*, vol. 93, no. 1–3. 2007.

[77] D. L. Miller, N. B. Smith, M. R. Bailey, G. J. Czarnota, K. Hynynen, and I. R. S. Makin, "Overview of therapeutic ultrasound applications and safety considerations," *Journal of Ultrasound in Medicine*. 2012.

[78] S. Mitragotri, "Healing sound: The use of ultrasound in drug delivery and other therapeutic applications," *Nat. Rev. Drug Discov.*, vol. 4, no. 3, pp. 255–260, 2005.

[79] H. H. Pennes, "Analysis of tissue and arterial blood temperatures in the resting human forearm," *J. Appl. Physiol.*, vol. 85, no. 1, 1948.

[80] Z. Izadifar, D. Chapman, and P. Babyn, "Applications and Safety of Therapeutic Ultrasound: Current Trends and Future Potential," *Clin. Res. Open Access*, vol. 3, no. 1, 2017.

[81] W. J. Elias *et al.*, "A pilot study of focused ultrasound thalamotomy for essential tremor," *N. Engl. J. Med.*, vol. 369, no. 7, 2013.

[82] J. G. Lynn, R. L. Zwemer, A. J. Chick, and A. E. Miller, "A new method for the generation and use of focused ultrasound in experimental biology," *J. Gen. Physiol.*, vol. 26, no. 2, 1942.

[83] W. J. FRY, W. H. MOSBERG, J. W. BARNARD, and F. J. FRY, "Production of focal destructive lesions in the central nervous system with ultrasound," *J. Neurosurg.*, vol. 11, no. 5, 1954.

[84] M. Z. Mahmoud, M. Alkhorayef, K. S. Alzimami, M. S. Aljuhani, and A. Sulieman, "High-intensity focused ultrasound (HIFU) in uterine fibroid treatment: Review study," *Polish J. Radiol.*, vol. 79, no. 1, pp. 384–390, 2014.

[85] "ExAblate Model 4000 Type 1.0 System (ExAblate Neuro) for the unilateral Thalamotomy treatment of idiopathic Essential Tremor patients with medication refractory tremor." [Online]. Available: https://www.accessdata.fda.gov/cdrh_docs/pdf15/P150038a.pdf.

[86] "ExAblate System, Model 2000/2100/2100 V1 for pain palliation of Metastatic Bone Cancer." [Online]. Available: https://www.accessdata.fda.gov/cdrh_docs/pdf11/P110039A.pdf.

[87] "Sonablate® 450 indicated for transrectal high intensity focused ultrasound (HIFU) ablation of prostatic tissue." [Online]. Available: https://www.accessdata.fda.gov/cdrh_docs/pdf15/DEN150011.pdf.

[88] F. U. Fundation, "2019 State of the Field Report," 2019.

[89] T. J. Dubinsky, T. D. Khokhlova, V. Khokhlova, and G. R. Schade, "Histotripsy: The Next Generation of High-Intensity Focused Ultrasound for Focal Prostate Cancer Therapy," *Journal of ultrasound in medicine : official journal of the American Institute of Ultrasound in Medicine*, vol. 39, no. 6. 2020.

[90] M. Hoogenboom, D. Eikelenboom, M. H. den Brok, A. Heerschap, J. J. Fütterer, and G. J. Adema, "Mechanical High-Intensity Focused Ultrasound Destruction of Soft Tissue: Working Mechanisms and Physiologic Effects," *Ultrasound in Medicine and Biology*, vol. 41, no. 6. 2015.

[91] E. Vlaisavljevich *et al.*, "Image-guided non-invasive ultrasound liver ablation using histotripsy: Feasibility study in an in vivo porcine model," in *IEEE International Ultrasonics Symposium, IUS*, 2012.

[92] G. R. Schade *et al.*, "Boiling histotripsy of the kidney: Preliminary studies and predictors of treatment effectiveness," *J. Acoust. Soc. Am.*, vol. 136, no. 4, 2014.

[93] T. D. Khokhlova, M. S. Canney, V. A. Khokhlova, O. A. Sapozhnikov, L. A. Crum, and M. R. Bailey, "Controlled tissue emulsification produced by high intensity focused ultrasound shock waves and millisecond boiling," *J. Acoust. Soc. Am.*, vol. 130, no. 5, 2011.

[94] K. J. Pahk, D. K. Dhar, M. Malago, and N. Saffari, "Ultrasonic histotripsy for tissue therapy," in *Journal of Physics: Conference Series*, 2015, vol. 581, no. 1.

[95] K. J. Pahk *et al.*, "Boiling Histotripsy-induced Partial Mechanical Ablation Modulates Tumour Microenvironment by Promoting Immunogenic Cell Death of Cancers," *Sci. Rep.*, vol. 9, no. 1, 2019.

[96] T. G. Schuster, J. T. Wei, K. Hendlin, R. Jahnke, and W. W. Roberts, "Histotripsy Treatment of Benign Prostatic Enlargement Using the Vortx Rx System: Initial Human Safety and Efficacy Outcomes," *Urology*, vol. 114, 2018.

[97] F. Foundation, "Blood-Brain Barrier Opening."

[98] K. Hynynen, N. McDannold, N. Vykhodtseva, and F. A. Jolesz, "Non-invasive opening of BBB by focused ultrasound," *Acta Neurochir. Suppl.*, no. 86, 2003.

[99] W. M. Arif *et al.*, "Focused ultrasound for opening blood-brain barrier and drug delivery monitored with positron emission tomography," *Journal of Controlled Release*, vol. 324. 2020.

[100] S. I. Rapoport, M. Hori, and I. Klatzo, "Testing of a hypothesis for osmotic opening of the blood-brain barrier.," *Am. J. Physiol.*, vol. 223, no. 2, 1972.

[101] D. Yin, J. Forsayeth, and K. S. Bankiewicz, “Optimized cannula design and placement for convection-enhanced delivery in rat striatum,” *J. Neurosci. Methods*, vol. 187, no. 1, 2010.

[102] L. B. Liu, Y. X. Xue, and Y. H. Liu, “Bradykinin increases the permeability of the blood-tumor barrier by the caveolae-mediated transcellular pathway,” *J. Neurooncol.*, vol. 99, no. 2, 2010.

[103] N. Lipsman *et al.*, “Blood–brain barrier opening in Alzheimer’s disease using MR-guided focused ultrasound,” *Nat. Commun.*, vol. 9, no. 1, 2018.

[104] E. E. Konofagou, Y.-S. Tunga, J. Choia, T. Deffieuxa, B. Baseria, and F. Vlachosa, “Ultrasound-Induced Blood-Brain Barrier Opening,” *Curr. Pharm. Biotechnol.*, vol. 13, no. 7, 2012.

[105] K. T. Chen, K. C. Wei, and H. L. Liu, “Theranostic strategy of focused ultrasound induced blood-brain barrier opening for CNS disease treatment,” *Frontiers in Pharmacology*, vol. 10, no. FEB. 2019.

[106] C. H. Fan and C. K. Yeh, “Microbubble-enhanced focused ultrasound-induced blood-brain barrier opening for local and transient drug delivery in central nervous system disease,” *Journal of Medical Ultrasound*, vol. 22, no. 4. 2014.

[107] A. Abrahao *et al.*, “First-in-human trial of blood–brain barrier opening in amyotrophic lateral sclerosis using MR-guided focused ultrasound,” *Nat. Commun.*, vol. 10, no. 1, 2019.

[108] A. J. Coleman and J. E. Saunders, “A review of the physical properties and biological effects of the high amplitude acoustic fields used in extracorporeal lithotripsy,” *Ultrasonics*, vol. 31, no. 2. 1993.

[109] G. H. Haertling, “Ferroelectric ceramics: History and technology,” *J. Am. Ceram. Soc.*, vol. 82, no. 4, pp. 797–818, 1999.

[110] S. J. Ahmed, J. Kivinen, B. Zaporzan, L. Curiel, S. Pichardo, and O. Rubel, “BerryPI: A software for studying polarization of crystalline solids with WIEN2k density functional all-electron package,” *Comput. Phys. Commun.*, vol. 184, no. 3, pp. 647–651, 2013.

[111] K. C. Kao, *Dielectric Phenomena in Solids*. 2004.

[112] Z. Ma *et al.*, “Ferroelectric phase transition of BaTiO3 single crystal based on a tenth order Landau-Devonshire potential,” *Comput. Mater. Sci.*, 2017.

[113] H. Fu and R. E. Cohen, “Polarization rotation mechanism for ultrahigh electromechanical response in single-crystal piezoelectrics,” *Nature*, vol. 403, no. 6767, pp. 281–283, 2000.

[114] M. Budimir, D. Damjanovic, and N. Setter, “Qualitative distinction in enhancement of the piezoelectric response in PbTiO3 in proximity of coercive fields: 90° versus 180° switching,” *J. Appl. Phys.*, vol. 101, no. 10, pp. 1–5, 2007.

[115] Ranier C. TJIPTOPRODJO, “On a Finite Element Approach to Modeling of Piezoelectric Element Driven Compliant Mechanisms,” University of Saskatchewan, 2005.

[116] M. J. TURNER, R. W. CLOUGH, H. C. MARTIN, and L. J. TOPP, “Stiffness and Deflection Analysis of Complex Structures,” *J. Aeronaut. Sci.*, 1956.

[117] E. Madenci and I. Guven, *The finite element method and applications in engineering using Ansys®*. Springer US, 2006.

[118] S. S. Rao, *The finite element method in engineering*. Elsevier Inc., 2017.

[119] M. S. Khan, C. Cai, and K. C. Hung, “Acoustics Field and Active Structural Acoustic Control Modeling in ANSYS Introduction,” *Int. ANSYS Conf. Proc.*, 2002.

[120] C. Howard and B. Cazzolato, *Acoustic Analyses Using Matlab® and Ansys®*. CRC Press, 2015.

[121] X. Chen, Y. Yin, Q. Hou, L. Jin, and X. Li, “The simulation and structural optimization of ultrasonic transducer,” *2010 2nd Int. Conf. Ind. Inf. Syst. IIS 2010*, vol. 1, pp. 330–333, 2010.

[122] ANSYS, “Theory Reference for the Mechanical APDL and Mechanical Applications,” *Knowl. Creat. Diffus. Util.*, 2009.

[123] K. J. Bathe, *Finite Element Procedures*. 1996.

[124] V. S. Sutkar, P. R. Gogate, and L. Csoka, “Theoretical prediction of cavitational activity distribution in sonochemical reactors,” *Chem. Eng. J.*, 2010.

[125] W. Tangsopa and J. Thongsri, “Development of an industrial ultrasonic cleaning tank based on harmonic response analysis,” *Ultrasonics*, vol. 91, no. January 2018, pp. 68–76, 2019.

[126] F. Li and G. Li, “Application of ANSYS APDL in the Design of Piezoelectric Transducer,” no. Aemt, pp. 506–511, 2015.

[127] Z. J. Seyed Abdolali, “Nonlinear Constitutive Modeling of Piezoelectric Materials,” University of Calgary, 2013.

[128] H. Allik and T. J. R. Hughes, “Finite element method for piezoelectric vibration,” *Int. J. Numer. Methods Eng.*, vol. 2, no. 2, pp. 151–157, 1970.

[129] Y. Liu, “Wave propagation study using finite element analysis,” University of Illinois, 2005.

[130] S. Moharana, “Modelling of Piezo-Structure Elastodynamic Interaction Through Bond Layer for Electro-Mechanical Impedance Technique,” no. November, 2012.

[131] T. Volk and M. Wöhlecke, “Lithium niobate: Defects, photorefraction and ferroelectric switching,” in *Springer Series in Materials Science*, 2009.

[132] F. G. Mitri, Z. E. A. Fellah, E. Closset, P. Trompette, and J. Y. Chapelon, “Determination of object resonances by vibro-acoustography and their associated modes,” *Ultrasonics*, vol. 42, no. 1–9, pp. 537–543, 2004.

[133] IEC International Standard 61161, “Ultrasonics - Power measurement - Radiation force balances and performance requirements.” 2013.

[134] G. Nader, E. Silva, and J. Adamowski, “Effective damping value of piezoelectric transducers determined by experimental techniques and numerical analysis,” *ABCM Symp. Ser. Mechatronics*, vol. 1, pp. 271–279, 2004.

[135] D. A. DeAngelis, “Predicting the Displacement Gain from the Mechanical Quality Factor in Ultrasonic Transducers,” in *Physics Procedia*, 2016, vol. 87.

[136] IEC, “IEC 61161 - Ultrasonics - Power measurement - Radiation force balances and performance requirements.” 2013.

[137] G. Leinenga, C. Langton, R. Nisbet, and J. Götz, “Ultrasound treatment of neurological diseases — current and emerging applications,” *Nat. Rev. Neurol.*, vol. 12, no. 3, pp. 161–174, 2016.

[138] C. Christoffersen, T. Ngo, R. Song, Y. Zhou, S. Pichardo, and L. Curiel, “Quasi Class-DE Driving of HIFU Transducer Arrays,” *IEEE Trans. Biomed. Circuits Syst.*, vol. 13, no. 1, pp. 214–224, 2019.

[139] T. Yuan *et al.*, “Driving an inductive piezoelectric transducer with class E inverter,” *Sensors Actuators, A Phys.*, vol. 261, pp. 219–227, 2017.